ELASTIC PROPERTIES OF JET-GROUTED GROUND AND APPLICATIONS

A Thesis

by

BENJAMIN LAURENT JUGE

Submitted to the Office of Graduate Studies of
Texas A&M University
in partial fulfillment of the requirements for the degree of

MASTER OF SCIENCE

May 2012

Major Subject: Civil Engineering

ELASTIC PROPERTIES OF JET-GROUTED GROUND AND APPLICATIONS

A Thesis

by

BENJAMIN LAURENT JUGE

Submitted to the Office of Graduate Studies of
Texas A&M University
in partial fulfillment of the requirements for the degree of

MASTER OF SCIENCE

Approved by:

Chair of Committee,	Chloe Arson
Committee Members,	Charles Aubeny
	Peter P. Valko
Head of Department	John Niedzwecki

May 2012

Major Subject: Civil Engineering

ABSTRACT

Elastic Properties of Jet-Grouted Ground and Applications. (May 2012)

Benjamin Laurent Juge, B.A., Ecole Speciale des Travaux Publics

Chair of Advisory Committee: Dr. Chloe Arson

With the development of urban areas and the constant need to change or improve the existing structures, a need for creative and less destructive soil reinforcement processes has occurred. Jet-grouting is one possible ground improvement technique. The behavior of the soil improved by jet-grouting is still not well understood. In this thesis, the mechanical behavior of the injected soil is modeled in order to determine the different parameters needed for the engineering design of a soil reinforcement based on jet-grouting. At first several models are presented in order to determine the extent of the injected zone within the soil mass, based on engineering parameters (cement poroelastic properties, injection rate). A model based on an energetic balance is proposed to compute the lower bound of the injection radius. The second part of the thesis focuses on the characterization of the uniaxial compressive strength of the soilcrete created in the injected area determined in the first part. Three different methods have been adapted to the problem. A hollow sphere model has been calibrated against published data. After calibration, both Eshelby’s and averaging methods proved to provide results close to the reference data. The last part of this report presents numerical studies of the pile and of a group of piles. The study of the group of piles focuses on the effect of arching between soilcrete columns to reduce the vertical settlements due to urban tunneling at the surface. It appears that the values obtained for settlements in the presence of jet-grouted columns are much less important than in usual tunneling problems (with no reinforcement).

TABLE OF CONTENTS

Page

Page

LIST OF FIGURES

Page

Page

Page

Page

LIST OF TABLES

CHAPTER I

INTRODUCTION

Over the last centuries, the increasing size and number of civil engineering structures has amplified constraints imposed on the soil. In response to these challenges, civil engineers have developed several different macro-structures, such as piles or slabs, in order to transfer those increasing stresses in a more efficient way. But it appears that in certain cases, a combination of improper soils and important loads makes those structures insufficient. As a result, civil engineers have developed a new set of techniques grouped under the term of ground improvement.

Contrary to the macro-structures that are based on an improvement of the transfer of the loads from the structure to the surrounding soils, ground improvement techniques are aimed at improving hydraulic and mechanical properties of a defined soil mass. An extensive literature review shows that the main characteristics improved are compressive strength and permeability.

Several methods of ground improvement were developed during the past decades, mainly techniques aiming at changing the soil fabric, and techniques aiming at improving the properties of the soil mass by adding structural elements in the ground (such as minipiles).

Grouting is a ground improvement technique that lies between the addition of structural material and the improvement of the soil fabric. Indeed it consists in the addition of a grout into the soil mass.

This thesis follows the style of International Journal of Rock Mechanics & Mining Sciences.

The properties of the grout and of the solid grains can be homogenized in order to get the properties of the grouted soil, the mechanical properties of which (e.g., Young’s modulus, shear strength) are expected to be better than the ones of the original soil. Soilcrete fabric can be seen as an improved soil fabric.

Jet grouting is based on the injection of cement with a high kinetic energy. The cement penetrates the soil mass and mixes with it to form a new structure, called “soilcrete”. Soilcrete may be considered as a composite material made of a matrix (constituted of cement) with inclusions (constituted of soil solid grains). In the sequel, both the cement matrix and the grain inclusions are considered elastic, with different Young’s moduli and compressive strengths. Soilcrete is expected to have a higher compressive strength, shear modulus and bulk modulus than the non-injected soil. Jet grouting may also be used to and decrease the hydraulic conductivity of the ground. Nowadays, jet grouting in used in projects involving tunneling, underpinning and retaining walls. Compensation grouting consists in using injection pressures of the same order of magnitude as in hydro-fracturing. The ground heave resulting from the increase of pore pressure in the cracks is expected to compensate the settlements occurring in the cracked ground. Compaction grouting is aimed at transforming a block of ground into a very stiff and dense material. On the other hand, permeation grouting is used to transform the geometry of the ground porous network to change the soil permeability. Chemical grouting consists in injecting substances that have the ability to seal fractures due to chemical reactions. When the chemical reactions involve bacteria, the technique is called bio-grouting. Bacteria contribute to crack closure by catalizing calcification reactions. Such biological healing techniques proved to give good results in concrete [1, 2]. In this paper, the study is focused on cement injection.

In order to use jet-grouting in engineering design, the penetration distance of the grout from the injection nozzle and the different mechanical properties of the soilcrete must be determined. In the first part of this thesis, the penetration distance of the grout is determined by several methods, in which it is assumed that the injection pressure, the cement characteristics and the mechanical parameters of the natural ground are known. The present research does not aim to give an exact value of the radius of injection, which would be illusory considering the high heterogeneity of the soil in place. The objective is instead to give reasonable upper and lower bounds for the value of the radius of injection.

By definition, soilcrete is a heterogeneous structure made of soil particles and cement. It can be reasonably assumed that the mechanical properties of the grains and of cement can be determined by the engineer. In the second part of this thesis, simple homogenization schemes are studied to predict the mechanical stiffness of soilcrete. The present work is restricted to a homogenization process in which cement fills the pores of the natural soil. Future investigations will be dedicated to the perturbation of the soil fabric by injection.

The third part of this thesis aims at assessing the performance of ground improvement by jet-grouting. Parametric studies are first performed on isolated jet-grouted columns. This is followed by a study of arching. The emphasis is put on the general methodology allowing predicting surface settlements from the injection characteristics and natural soil properties.

CHAPTER II

BACKGROUND

2-1 Ground Improvement

2-1-1 Improvement of the Soil Fabric

The first group of improvements is based on the idea to improve the fabric of the soil itself, by changing the structure, phases or composition of the solid or liquid phase composing the soil

The methods that improve the fabric of the soil are listed below:

- Ground water lowering and drainage techniques: lowering the groundwater level is necessary in some excavation projects. Lowering the water table is also required for permanent structures that are below the water table and are not waterproof, or are waterproof but not designed to resist to hydrostatic pressure. The common tools are walls, drain and pipes and pumping.
- Soil compaction and consolidation: there are several kinds of compaction but all them aim at increasing the density of the soil. The preloading technique uses a fill embankment to reduce the future settlement. The dynamic compaction technique is carried out using a heavy weight which is dropped above the piece of soil that is to be improved. Some methods also aim to accelerate compaction, consolidation drainage for instance. The main tests related to compaction are the Proctor and Modified Proctor tests. These tests determine the maximum density of a soil needed for a specific job site. These tests first determine the maximum

density achievable for the material creating in the process a figure that will be used as reference. Secondly, they test the effects of the moisture on soil density. These values are determined before any compaction takes place to develop the compactions specifications. The methodology for both tests are similar but the Modified Proctor gives higher value taking into account the fact that certain projects need a higher density.

- Artificial ground freezing: this is a method of temporary stabilization of the soil. The basic concept is making cooled brine circulate through underground tubing.

2-1-2 Addition of Structural Elements

Other processes involve the use of materials that are not present in the genuine soil. By their interactions with the surrounding soil, those micro-structures are improving the mechanical properties of the surrounding soil, due to the work of forces acting at a smaller scale than the contact forces developed by soil/structure interactions at the foundation scale. Mechanical properties can be averaged from the properties of the genuine soil and extra-components. The different processes belonging to this category are listed below:

- Underpinning: this technique is applied by extending the foundation of an already existing structure in depth or width in order to make it rest on a more supportive soil or distribute it on a larger surface. This result is obtained by digging boxes by hand underneath the structure and pouring those boxes with concrete. It appears that is technique is more often applied for structure with shallow foundations but is also working up to

15-20m deep. The main advantages of this method include the simplicity of the engineering required and the low cost.

- In situ ground reinforcement: many earth reinforcement techniques involve the inclusion of metal strips, welded wire fabric, geosynthetics, tree branches and twine in engineered fill embankment.
- Small-diameter cast-in-place elements for load-bearing and in situ earth reinforcement: those methods are also referred to as minipiles, micropiles and root piles. These different elements are often used as an alternative technique of underpinning even though the main used is for creating foundations for large area projects including highway or bridges. They are very useful for sites with difficult access or environmental sensibility. Micropiles are normally made of steel or metallic alloys with diameters of 60 to 200mm. They are usually installed by drilling, jacking or vibrating techniques.
- Vertical screens: this technique covers a broad area of protective or remedial systems, including continuous earth, semi rigid, and rigid cutoff walls; plastic barriers and hot bituminous mastic inserted in narrow trenches; permeable treatment beds; synthetic membranes with overlapping or interlocking sheet-pile sections and so on. In general the intent is to provide essential control of groundwater movement where it is necessary to maintain the balance in the water supply, where the risk of pollution exists, and where deep excavations are contemplated.

2-2 Grouting

2-2-1 Background

2-2-1-1 History

Numerous records document projects involving the use of some rudimentary techniques of grouting, starting before 1800 and developping throughout the 19s century. Those early techniques involved the use of aqueous suspensions containing lime or clay that were injected into joints and seams in the bedrock underlying dams in order to reduce water leakage.

Most of the current techniques employed for grouting use grout containing small amounts of cement. The earliest use of Portland cement as a grout dates back over 150 years in Europe and over 100 years in the United States.

A patent was issued in 1887 for a sodium silicate-based formula. This grout was mixed on site and injected. The main problem of this formula was that some of the chemicals were reacting too soon after mixing which lead to the requirement of a very rapid injection and thus a very few flexibility on the construction process.

To overcome this problem of early chemical reactions leading to the hardening of the grout, Hugo Joosten patented in 1925 a two-shot sodium silicate-based system. This process involved two steps. During the first step, the sodium silicate based chemical was injected in the adequate position in the soil mass. Only during the second step was injected the reactant, at the same location than the chemical, in order to begin the grout process of hardening. The main problem of this technique was obtaining the complete mixing of the chemical and the reactant, which prevented this technique to widespread, even though it was used in the United States until 1960.

The main next breakthrough came from polymer chemistry: the development of new formula allowed returning to single-shot techniques by slowing down the reactions occurring between the chemicals in the grout.

2-2-1-2 Definition

The Grouting Committee, Geotechnical Division of the American Society of Civil Engineers, defines grout as injection of material into a formation of soil or rocks in order to increase the mechanical rigidity or decrease the hydraulic conductivity of the soil.

This definition is very broad because the changes aimed at using grouting techniques can be related to strength and/or permeability. This means that by definition any material that has the ability to penetrate porous space in the soil could be virtually used.

The main grouting techniques are listed in the different sections below.

2-2-2 Chemical Grouting

Chemical Grouting is used to stabilize shallow foundations near the ground surface. It is often used in the loose soil directly under the structure. It can also be used for waterproofing leaks in underground structures. Chemical grout is defined as any grouting material characterized by being pure solution, with no particles in suspension. The grout used in chemical grouting techniques is more liquid than in cement grouting techniques. The reactant in the solid phase has to be mixed with water to form a solution. Thus the chemical grout is characterized by its solid content. The liquid chemical is injected beneath the building and once it hardens, it seals fractures and joints and has the same properties as a stone. This makes the area waterproof.

2-2-3 BioGrouting

BioGrouting is the in-situ stimulation of a cementation process, where sand is converted into a sandstone-like material using calcium carbonate crystals. A natural biological process is used for this diagenesis. It is based on a reaction where naturally-occurring bacteria ensure that small chalk crystals are deposited on the surface of grains of sands. The general chemical reaction is given below:

$$\mathrm{CO(NH_2)_2 + Ca^{2+} + 2H_2O \xrightarrow{Urease} 2NH_4{}^{+} + CaCO_3(s)} \tag{2.1}$$

2-2-4 Compensation Grouting

Compensation Grouting is based in hydraulic fracturation, and is used to control settlement. Injection causes the ground to crack. Grout is forced into fractures, thereby causing an expansion to take place, which counteracts settlements, or produces a controlled heave of the foundation. Multiple injections and multiple levels of fractures create a complementary reinforcement zone.

2-2-5 Compaction Grouting

Compaction grouting is a technique in which very stiff, low-mobility cements are injected at high pressure in order to form a very dense and coherent bulb. It uses controlled displacement to increase the density of soft or loose soils. The typical applications of that technique are settlement control, structural re-leveling, and the remediation of sinkholes.

A small diameter steel casing is inserted in the zone of the ground that needs to be improved. Then, a stiff mortar-like grout is injected at high pressure to displace and compact the surrounding soil. Injection continues as the casing is withdrawn, in order to form a large diameter column of interconnected grout bulbs. The formation of cement bulbs intensively compacts the surrounding soil. The compaction grouting technique is illustrated in (Figure 1).

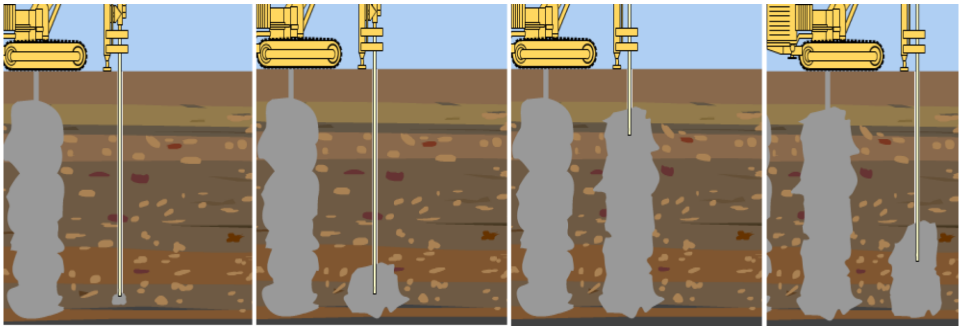

Figure 1- Main steps of compaction grouting (taken from [3])

2-2-6 Permeation Grouting

Permeation grouting is a more precise term for what is commonly referred to as a pressure grouting. Permeation grouting is defined as the direct pressure injection of a fluid grout into the ground. It is used for filling joints and other defects in rock, soil, concrete, masonry and similar materials. Another application is to change the soil into a denser state, by reducing or filling the porous space (compaction or filling). Permeation grouting can be used to ensure complete filling under precast member, base plates and other similar assemblies (see Figure 2).

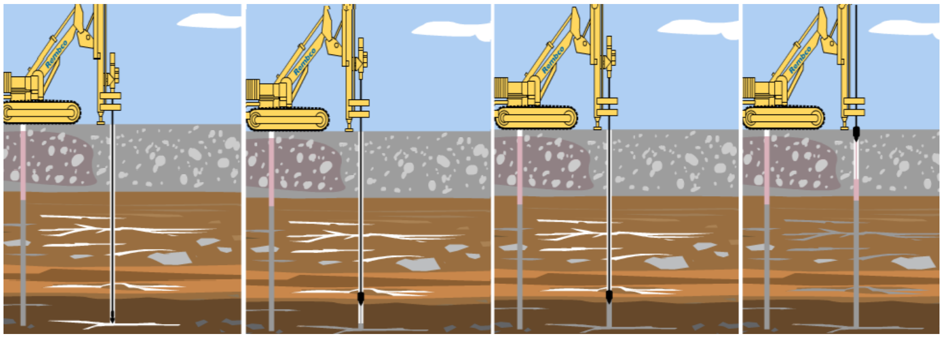

Figure 2- Main steps of permeation grouting (taken from [3])

2-2-7 Jet-Grouting

Jet-grouting is a technique has gained importance in civil engineering since 1970. It owes its origins to experiences acquired some decades ago in the oil drilling industry when unblocking strings of drill rods locked at great depths.

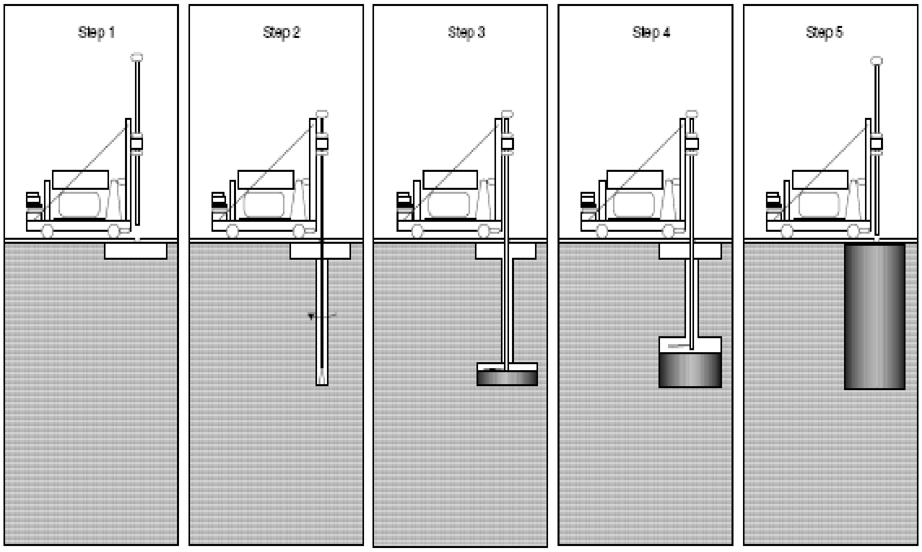

Figure 3- Main steps of jet-grouting (taken from [4])

Jet grouting is based on the injection of cement with a high kinetic energy. The grout penetrates the soil and then mixes with it (see Figure 3). Once it hardens the mixture forms a composite material called soilcrete, made of cement and soil solid grains, which have with different elastic moduli and compressive strengths. Soilcrete has a higher compressive strength, shear modulus, bulk modulus and a smaller permeability than the natural soil. As a result, jet grouting is used to improve the soil mechanical properties, or to reduce soil permeability.

Three injection techniques can be used, depending on the improved ground properties that are sought after treatment (Figure 4):

- Single rod: This is the simplest and most straightforward method. The grout jet cuts and mixes the soil and so provides essentially a mix-in-place effect. This technique is used almost exclusively for horizontal grouting. The most important feature of this type of jet-grouting technique is that jetting allows the cementing medium to be relatively uniformly mixed with a wide range of soils (both clay and sand) rather than being dependent on the in situ soils grading and permeability.
- Double rod: This method uses compressed air to enhance the cutting effect of the jet. For the same grout and injection rates, the diameter of the injected column can be twice as much as in the single rod technique:

A deeper penetration of the jet is allowed by the air acting as a buffer between the jet stream and groundwater.

The soil cut by the jet is prevented from falling back onto the jet, which reduces the energy lost through the turbulent action of the soil.

The cut soil is more efficiently removed from the region of jetting by the bubbling action of the compressed air.

- Triple rod: this is the most complicated jet grouting system due to the simultaneous injection of three different fluids: air, water and grout. The injection of those three fluids permits more soil to be removed from the ground, and therefore, the triple system can be used as a full replacement of the in situ oil wit grout.

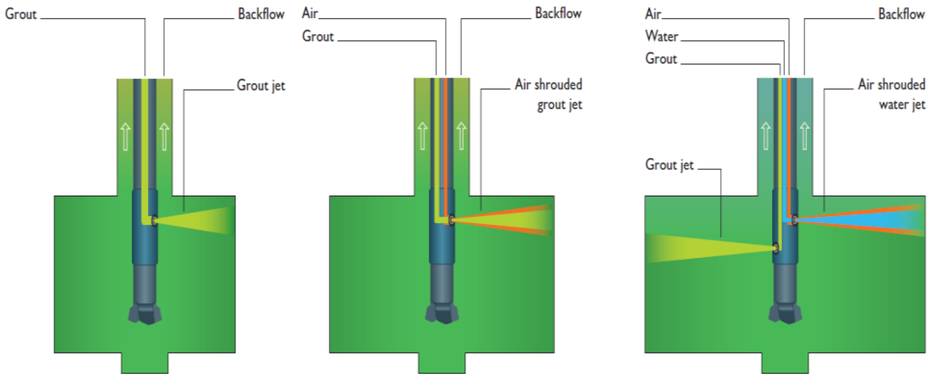

Figure 4- Schematic representation of the three different injection techniques used in jet-grouting (single rod, double rod and triple rod) (taken from [5])

The diameter of the injected column and the strength of soilcrete do not only depend on the grouting method, but also on soil type, density, plasticity, water content, water table location, amount of cement injected, soilcrete age, and injection rate. In the model described in the following part, only the single rod method is considered and it is assumed that soil properties (including pore size distribution) are given. As a result, in the following study, only the variations of cement characteristics can influence soilcrete elastic properties

A first set of applications of jet-grouting consists in the improvement of ground properties such as stiffness and strength, for instance:

- Blocking the flow of water and reducing seepage
- Fill massive voids in soil or rocks
- Strengthen soil or rocks

- Correct settlement damage to structure
- Form bearing piles
- Install and increase the capacity of anchors and tiebacks
- Support soil and create secant-pile walls

Jet-grouting is also used to repair structures:

- Returning into a monolithic mass disintegrated pieces of concrete or masonry
- Repairing and welding cracks in underground concrete structures
- Filling cracks, splits, and other defects in the repair of timber structural components
- Securing of bolts, rods, and anchors in drilled holes
- Corrosion protection for pre-stress tendons and anchors
- Casting of preplaced aggregate concrete

Jet-grouting – mainly horizontal jet-grouting - has also been extensively used for tunneling [1, 2, 4, 6, 7, 8, 9], mainly to improve the elastic and transport properties of the ground mass. Two jet-grouting techniques are currently used. The first one is the improvement of the excavated material. This is obtained by injecting grout (vertically or sub-horizontally) into the soil mass that is going to be extracted. Jet-grouting improves the mechanical properties of the soil mass surrounding the excavation, which is the result of increased friction at the contact between ground particles. As a result, arching effects are more likely to occur in the improved soil mass, which prevents ground collapse during the excavation.

The second method is the creation of a shell, made by sub-horizontal jet-grouting, around the excavated mass. This shell, made of soilcrete, is designed in order to avoid a massive soil failure during the excavation that is weakening the structure of the soil mass. The shell acts like a support.

Jet-grouting can also be employed as an underpinning method, as explained in [10, 11, 12]. In this method, the jet-grouting is used to create one or several columns of soilcrete under an existing structure. The advantage of using the jet-grouting technique for underpinning is that it allows an easy access to the zone where the ground needs to be improved (Figure 5).

Figure 5- Schematic representation of the underpinning method used with jet-grouting (taken from [13])

Jet-grouting has also been used to play the role of a retaining structure for slope stabilization, as described in [2, 14]. In case studies reported in [15, 16] jet-grouting is used to create cutoff or barrier walls.

In [15], the author studied the case of a site in Northern New Jersey where a storage tank have been removed and the excavation backfilled with silty sand. It appeared later that the surrounding undisturbed soils have been contaminated by chlorinated hydrocarbon and that these contaminants were migrating into the clean fill and seeping downward through the previously excavated area threatening the groundwater in the underlying rocks. In order to fix the problem, a series of columns were installed in a primary grid pattern. A similar overlapping grid of secondary columns was installed to complete the coverage of the entire area (The pattern geometry is shown in Figure 6. The results are a stabilization of the block and the creation of a vertical barrier preventing the further migration of the contaminant as long as a bottom "plug" to prevent the vertical migration into the underlying groundwater.

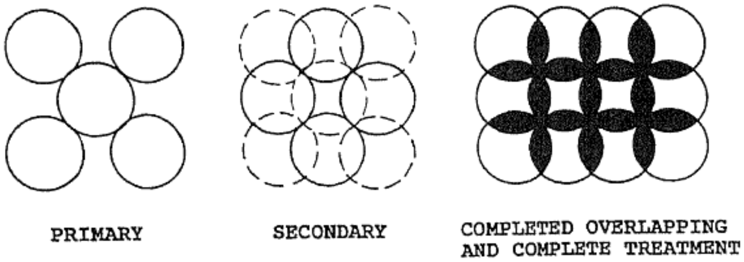

Figure 6- Typical block treatment pattern (taken from [15])

In [17], the jet-grouting technology has been successfully used to construct a below-grade barrier wall to contain petroleum hydrocarbon contamination in Spokane, Washington. A wall consisting of overlapping jet-grouted columns was constructed in order to reduce the permeability of the sand and gravel formations present on the site and thus intercept the flow of groundwater and heavy petroleum hydrocarbon in those formations.

2-3 Homogenization Techniques

2-3-1 Elastic Solids with Microcavities

This section illustrates how the overall elasticity and compliance tensors of a porous RVE may be estimated from homogenization techniques for a relatively small volume fraction. Two extreme cases are considered

- When the elastic contains a dilute distribution of cavities, so that the typical cavities are so far apart that their interaction may be neglected
- When the cavities are randomly distributed.

2-3-1-1 Effective Moduli of an Elastic Plate Containing Circular Holes [18]

In this subsection, the problem of estimating the effective moduli of linearly elastic homogeneous solid containing circular cylindrical cavities is worked out in some detail. Assume either plane stress which then corresponds to a thin plate containing circular holes, or a plain strain which then corresponds to a long cylindrical body containing cylindrical holes with circular cross sections and a common generator. Both cases deal with a two-dimensional problem. A rectangular Cartesian coordinate system is chosen such that:

$\sigma_{3i} = \sigma_{i3} = 0$ for plane stress, (2.2a)

$\varepsilon_{3i} = \varepsilon_{i3} = 0$ for plane strain, (2.2b)

For $i = 1, 2, 3$. All field quantities, hence, are functions of two space variables, x_1 and x_2, or when polar coordinates are used, r and θ.

For simplicity, the matrix of the RVE is assumed to be isotropic, linearly elastic, and homogeneous. Then, the corresponding two-dimensional stress-strain and the strain-stress relations become:

$$\sigma_{ij} = \mu\left\{-\frac{\kappa-3}{\kappa-1}\delta_{ij}\delta_{kl} + (\delta_{ik}\delta_{jl} + \delta_{il}\delta_{jk}\right\}\varepsilon_{kl} \tag{2.3}$$

$$\varepsilon_{ij} = \frac{1}{\mu}\left\{\frac{\kappa-3}{8}\delta_{ij}\delta_{kl} + \frac{1}{4}(\delta_{ik}\delta_{jl} + \delta_{il}\delta_{jk}\right\}\sigma_{kl} \tag{2.4}$$

or in matrix notation

$$\begin{bmatrix}\sigma_{11}\\ \sigma_{22}\\ \sigma_{12}\end{bmatrix} = \mu\begin{bmatrix}(\kappa+1)/(\kappa-1) & -(\kappa-3)/(\kappa-1) & 0\\ -(\kappa-3)/(\kappa-1) & (\kappa+1)/(\kappa-1) & 0\\ 0 & 0 & 1\end{bmatrix}\begin{bmatrix}\varepsilon_{11}\\ \varepsilon_{22}\\ 2\varepsilon_{12}\end{bmatrix} \tag{2.5}$$

$$\begin{bmatrix}\varepsilon_{11}\\ \varepsilon_{22}\\ 2\varepsilon_{12}\end{bmatrix} = \frac{1}{\mu}\begin{bmatrix}(\kappa+1)/8 & (\kappa-3)/8 & 0\\ (\kappa-3)/8 & (\kappa+1)/8 & 0\\ 0 & 0 & 1\end{bmatrix}\begin{bmatrix}\sigma_{11}\\ \sigma_{22}\\ \sigma_{12}\end{bmatrix} \tag{2.6}$$

where μ is the shear modulus, ν is the Poisson ratio, and

$$\kappa = \begin{cases}3-4\nu \text{ for plane strain}\\ \frac{3-\nu}{1+\nu} \text{ for plane stress}\end{cases} \tag{2.7}$$

This theory supposes that the microcavities are empty which explain why there is no matrix representing a second material.

2-3-1-2 Effective Bulk Modulus of an Elastic Body Containing Spherical Cavities

In this subsection, the effective bulk modulus of a linearly elastic homogeneous solid containing micro-cavity is estimated. For simplicity, an isotropic matrix containing micro-cavities, Ω_α is assumed, its radius is a_α $(\alpha = 1, 2, \ldots, n)$. The bulk modulus of the isotropic matrix material is defined in term of the Lame constants, λ and μ, by:

$$K = \lambda + \frac{2}{3}\mu \tag{2.8}$$

The mean stress, $\sigma_{ij}/3 \equiv \sigma$ and the volumetric strain, $\varepsilon_{ij} \equiv \varepsilon$, are then related by:

$$\sigma = K\varepsilon \tag{2.9}$$

Consider the response of the RVE, subjected to the prescribed macro-stress $\mathbf{\Sigma} = \sigma^0\mathbf{1}^{(2)}$, or to the prescribed macro-strain $\mathbf{E} = \varepsilon^0\mathbf{1}^{(2)}$. First the overall bulk modulus is estimated, assuming a dilute distribution of micro-cavities, i.e., neglecting the interaction among them.

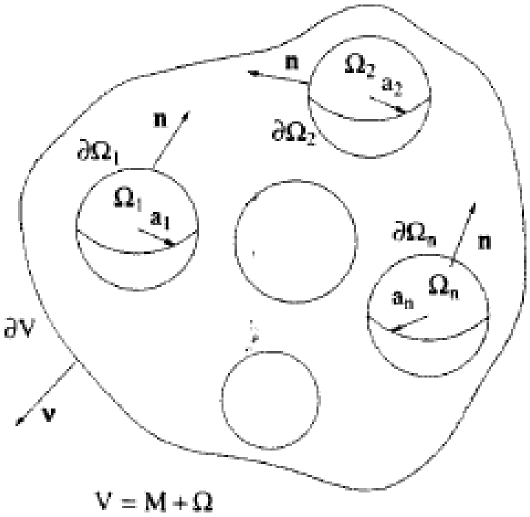

Figure 7- An RVE containing spherical microcavities (taken from [18])

For a typical cavity Ω_α of radius a_α, the field variables in the neighborhood of Ω_α are assumed to be spherically symmetric (see Figure 8):

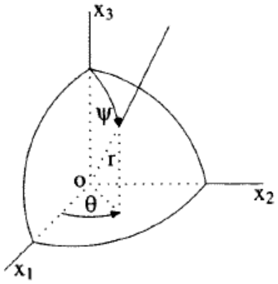

Figure 8- A spherical cavity and spherical coordinates (taken from [18])

The additional strain or the decremental stress is computed, using the spherical coordinates (r, θ, ψ)(see Figure 8) with the origin at the center of the cavity. Under the far-field stress $\sigma^0 \mathbf{1}^{(2)}$, the displacement components are:

$$u_r = u_r(r) = \frac{\sigma^0}{3\lambda+2\mu} r + \frac{\sigma^0}{4\mu}\frac{a^3}{r^2} \quad u_\theta = 0 \quad u_\psi = 0 \tag{2.10}$$

where a is the radius of the cavity. Since the unit normal **n** on $d\Omega_\alpha$ coincides with the radical base vector e_r, the average strain for Ω_α, becomes

$$\bar{\varepsilon}_{ii}{}^{\alpha} = \bar{\varepsilon}^{\alpha} = \frac{1}{\Omega_\alpha} \int u_r(a) dS_{\partial\Omega_\alpha} = \frac{1}{\Omega_\alpha}\{\partial\Omega_\alpha u_r(a)\} \tag{2.11}$$

where $\Omega_\alpha = \frac{4\pi a^3}{3}$, and $d\Omega_\alpha = 4\pi a^2$. Therefore, the additional volumetric strain due to the presence of cavities is given by

$$\bar{\varepsilon}^{c}{}_{ii} = \bar{\varepsilon}^{c} = \frac{1}{K} f(1 + \frac{3K}{4\mu})\sigma^0 \tag{2.12}$$

where f is the void volume fraction. From (2.12), the dilute estimate of the effective bulk modulus, $\bar{K}$, is obtained when the macro-stress is prescribed,

$$\frac{\bar{K}}{K} = \left\{1 + f\frac{3(1-\nu)}{2(1-2\nu)}\right\}^{-1} = 1 - f\frac{3(1-\nu)}{2(1-2\nu)} + O(f^2) \tag{2.13}$$

If the macro-strain $\mathbf{E} = \varepsilon^0 \mathbf{1}^{(2)}$ is prescribed, an infinite body subjected to the farfield stress given by $K\varepsilon^0 \mathbf{1}^{(2)}$ is considered. Then, by replacing σ^0 with $K\varepsilon^0$ in (2.12), the corresponding additional volumetric strain due to the cavities becomes

$$\bar{\varepsilon}^{c} = f(1 + \frac{3K}{4\mu})\varepsilon^0 \tag{2.14}$$

From (2.14) the effective bulk modulus, $\bar{K}$, is estimated for the prescribed macro-strain, as:

$$\frac{\bar{K}}{K} = 1 - f\left(1 + \frac{3K}{4\mu}\right) = 1 - f\frac{3(1-\nu)}{2(1-2\nu)} \tag{2.15}$$

Comparing (2.13) and (2.15), it is observed that the two expressions agree with each other to within the first order in the void volume fraction f. For $\nu = \frac{1}{3}, \frac{\bar{\kappa}}{\kappa} = (1 - 3\mathrm{f})^{-1}$ for the case when the macro-stress is prescribed, and $\frac{\bar{\kappa}}{\kappa} = (1 - 3\mathrm{f})$ when the macro-strain is prescribed.

The estimates (2.13) and (2.15) do not include any interaction among the cavities. To include this interaction for a random distribution of cavities, the self-consistent method may be used. Then for the case when the macro-stress is regarded prescribed, (2.12) is replaced by

$$\bar{\varepsilon}^{\mathrm{c}} = \frac{1}{\mathrm{K}}\mathrm{f}(1 + \frac{3\bar{\mathrm{K}}}{4\bar{\mu}})\sigma^0 \qquad (2.16)$$

and instead

$$\frac{\bar{\mathrm{K}}}{\mathrm{K}} = 1 - \mathrm{f}\frac{3(1-\bar{\nu})}{2(1-2\bar{\nu})} \qquad (2.17)$$

Which requires an estimate of the overall Poisson ratio $\bar{\nu}$. Similarly, a self-consistent estimate of the overall bulk modulus can be obtained when the macro-strain is regarded prescribed. The result is identical for the prescribed macro-stress.

2-3-1-3 Deformation Energy Stored by the Homogenized REV [18]

In the following, it is assumed that the overall compliance tensor $\bar{\mathrm{D}}$ and elasticity tensor $\bar{\mathrm{C}}$ are known (they can be determined for a solid containing cavities, as explained above).

The overall quantities $\bar{\mathrm{D}}$ and $\bar{\mathrm{C}}$ may also be defined in terms of the total elastic energy stored in the RVE, in the sense that if the RVE is replaced by an equivalent linearly elastic and homogeneous solid, it must store the same amount of elastic energy as the actual RVE for the same macro-stress, $\boldsymbol{\Sigma} = \boldsymbol{\sigma}^0$, when the overall stress is prescribed, or the same macro-strain, $\mathbf{E} = \boldsymbol{\varepsilon}^0$, when the overall strain is prescribed. The two cases (prescribed macro-stress and prescribed macro-strain) are treated separately, starting with the former.

Denote the macro-complementarity strain energy function by $\mathrm{W}^{\mathrm{c}}(\boldsymbol{\Sigma}) = \mathrm{W}^{\mathrm{c}}(\sigma^0)$, when the macro-stress is given by $\boldsymbol{\Sigma} = \boldsymbol{\sigma}^{\mathbf{0}}$.

$$\mathrm{W}^{\mathrm{c}}(\boldsymbol{\Sigma}) = < \mathrm{w}^{\mathrm{c}} > = \frac{1}{\mathrm{V}} \int \mathrm{w}^{\mathrm{c}}\big(\boldsymbol{\sigma}(\mathbf{x}; \boldsymbol{\Sigma})\big) \mathrm{dV} \tag{2.18}$$

Where $\mathrm{w}^{\mathrm{c}}(\boldsymbol{\sigma})$ is the complementary energy density function of the matrix material at point **x**. Since the RVE is linearly elastic and subjected to uniform tractions $\mathbf{t}^0 = \boldsymbol{\nu}.\boldsymbol{\sigma}^0$on $\partial \mathrm{V}$.

$$2\mathrm{W}^{\mathrm{c}}\big(\boldsymbol{\sigma}^{\mathbf{0}}\big) = < \sigma : \varepsilon > = \boldsymbol{\sigma}^0 : < \varepsilon > = \boldsymbol{\sigma}^0 : \bar{\boldsymbol{\varepsilon}} = \boldsymbol{\sigma}^0 : (\varepsilon^0 + \bar{\varepsilon}^{\mathrm{c}}) = \boldsymbol{\sigma}^0 : (\mathbf{D} + \mathbf{H}) : \boldsymbol{\sigma}^0 \tag{2.19}$$

Hence, whatever the structure of the macro-cavities, only the symmetric part of **H** contributes to the stored elastic energy; note that the microstructure is fixed and no frictional effects are included. Therefore the definition of **H** is:

$$\mathrm{H}_{\mathrm{ijkl}} = \frac{1}{\mathrm{V}} \int \int \frac{1}{2} \big(\mathrm{h}_{\mathrm{ijkl}} + \mathrm{h}_{\mathrm{klij}}\big) \mathrm{dSdS}_{\partial \mathrm{V}\, \partial \Omega} \tag{2.20}$$

The effective compliance of the RVE may now be defined as the constant symmetric tensor $\bar{\mathbf{D}}$ with the property that, for any macro-stress $\boldsymbol{\Sigma} = \boldsymbol{\sigma}^0$, the overall complementary energy density is:

$$\mathrm{W}^{\mathrm{c}}\big(\boldsymbol{\sigma}^{\mathbf{0}}\big) = \frac{1}{2} \boldsymbol{\sigma}^{\mathbf{0}} : \bar{\mathbf{D}} : \boldsymbol{\sigma}^{\mathbf{0}} \tag{2.21}$$

Comparison with (2.19) shows that $\bar{\mathbf{D}}$ is defined by

$$\bar{\mathbf{D}} = \mathbf{D} + \mathbf{H} \tag{2.22}$$

In a similar manner, when the macro-strain is prescribed to be $\mathbf{E} = \boldsymbol{\varepsilon}^0$, the overall elastic energy density of the RVE becomes

$$\mathrm{W}(\mathbf{E}) = < \mathrm{w} > = \frac{1}{\mathrm{V}} \int \mathrm{w}\big(\boldsymbol{\sigma}(\mathbf{x}; \mathbf{E})\big) \mathrm{dV} \tag{2.23}$$

Moreover

$$2\mathrm{W}\left(\boldsymbol{\varepsilon}^{\mathbf{0}}\right) = < \sigma : \varepsilon > = < \sigma > : \boldsymbol{\varepsilon}^{\mathbf{0}} = \overline{\boldsymbol{\sigma}} : \boldsymbol{\varepsilon}^{\mathbf{0}} = (\sigma^0 + \overline{\sigma}^c) : \boldsymbol{\varepsilon}^0 = \boldsymbol{\varepsilon}^0 : (\mathbf{C} - \mathbf{C} : \mathbf{J}) : \boldsymbol{\varepsilon}^0 \quad (2.24)$$

Defining the overall elasticity tensor $\bar{\mathbf{C}}$ Such that

$$\mathrm{W}\left(\boldsymbol{\varepsilon}^{\mathbf{0}}\right) = \frac{1}{2} \boldsymbol{\varepsilon}^{\mathbf{0}} : \bar{\mathbf{C}} : \boldsymbol{\varepsilon}^{\mathbf{0}} \quad (2.25)$$

for any prescribed constant strain $\boldsymbol{\varepsilon}^{\mathbf{0}}$, it is concluded from the two previous equations that:

$$\bar{\mathbf{C}} = \mathbf{C} - \mathbf{C} : \mathbf{J} \quad (2.26)$$

where $\mathbf{C} : \mathbf{J}$ is required to have the following symmetry property:

$$\mathrm{C}_{\mathrm{ijrs}} \mathrm{J}_{\mathrm{rskl}} = \mathrm{C}_{\mathrm{klrs}} \mathrm{J}_{\mathrm{rsij}} \quad (2.27)$$

2-3-2 The Self-Consistent Method [10]

The idea of the so-called self-consistent scheme consists of assuming that each particle of a given phase (pore or solid) reacts as if it were embedded in the equivalent homogeneous medium which is looked for.

Let $\mathbb{C}^{\mathrm{SC}}$ denote the stiffness tensor of the equivalent homogeneous medium. In the case of an isotropic morphology, the average strain in the pore space (resp. in the solid) is estimated by the uniform strain in a spherical pore (resp. spherical solid particle) surrounded by an infinite medium with stiffness $\mathbb{C}^{\mathrm{SC}}$, subjected to the uniform strain boundary condition $\underline{\xi} \rightarrow \mathrm{E}_0 \cdot \underline{z}$ at infinity:

$$\bar{\varepsilon}^{\mathrm{p}} = (\mathbb{I} + \mathbb{P}^{\mathrm{sc}} : (\mathbb{C}^{\mathrm{p}} - \mathbb{C}^{\mathrm{sc}}))^{-1} : \mathbf{E}_0 = (\mathbb{I} - \mathbb{P}^{\mathrm{sc}} : \mathbb{C}^{\mathrm{sc}})^{-1} : \mathbf{E}_0 \quad (2.28)$$

$$\bar{\varepsilon}^{\mathrm{s}} = (\mathbb{I} + \mathbb{P}^{\mathrm{sc}} : (\mathbb{C}^{\mathrm{s}} - \mathbb{C}^{\mathrm{sc}}))^{-1} : \mathbf{E}_0 \quad (2.29)$$

where $\mathbb{C}^{s}$ is the stiffness matrix of the elastic material composing the solid matrix, $\mathbb{C}^{\mathrm{p}}$ is the stiffness matrix of the material composing the pore (considered as an elastic body), $\bar{\varepsilon}^{\mathrm{s}}$ is the average strain in the solid phase, and $\bar{\varepsilon}^{\mathrm{p}}$ is the average strain in the pore space.

When the self-consistent estimate of the stiffness tensor is isotropic, $\mathbb{P}^{\mathrm{SC}}$ is the $\mathbb{P}$ tensor ($\mathbb{P} = \mathbb{S}:(\mathbb{C}^{\mathrm{s}})^{-1}$ where $\mathbb{S}$ is the Eshelby tensor) of a spherical inclusion in an isotropic medium:

$$\mathbb{P}^{\mathrm{SC}} = \frac{\alpha^{\mathrm{sc}}}{3\mathrm{k}^{\mathrm{sc}}}\mathbb{J} + \frac{\beta^{\mathrm{sc}}}{2\mu^{\mathrm{sc}}}\mathbb{K} \tag{2.30}$$

$\mathbb{P}^{\mathrm{SC}}$ depends on the unknown self-consistent estimates k^{SC} and μ^{SC} of the homogenized bulk and shear moduli.

$$\mathbf{E}_0 = (\varphi_0(\mathbb{I} + \mathbb{P}^{\mathrm{sc}}:(\mathbb{C}^{\mathrm{p}} - \mathbb{C}^{\mathrm{sc}}))^{-1}) + (1-\varphi_0)(\mathbb{I} + \mathbb{P}^{\mathrm{sc}}:(\mathbb{C}^{\mathrm{s}} - \mathbb{C}^{\mathrm{sc}}))^{-1})^{-1}:\mathbf{E} \tag{2.31}$$

where E is the macroscopic strain tensor

That is:

$$\mathbf{E}_0 = \overline{(\mathbb{I} + \mathbb{P}^{\mathrm{sc}}:(\mathbb{C} - \mathbb{C}^{\mathrm{sc}}))^{-1}}^{-1}:\mathbf{E} \tag{2.32}$$

Returning to (2.29), the average strain concentration tensors$\overline{\mathbb{A}}^{\alpha}$ (α=s, p) take the form:

$$\overline{\mathbb{A}}^{\alpha} = (\mathbb{I} + \mathbb{P}^{\mathrm{sc}}:(\mathbb{C}^{\alpha} - \mathbb{C}^{\mathrm{sc}}))^{-1}:\overline{(\mathbb{I} + \mathbb{P}^{\mathrm{sc}}:(\mathbb{C} - \mathbb{C}^{\mathrm{sc}}))^{-1}}^{-1} \tag{2.33}$$

A concentration tensor is a linear operator that relates the microscopic concentration gradient to the macroscopic one.

$$\mathbb{C}^{\mathrm{sc}} = \overline{\mathbb{C}:(\mathbb{I} + \mathbb{P}^{\mathrm{sc}}:(\mathbb{C} - \mathbb{C}^{\mathrm{sc}}))^{-1}}:\overline{(\mathbb{I} + \mathbb{P}^{\mathrm{sc}}:(\mathbb{C} - \mathbb{C}^{\mathrm{sc}}))^{-1}}^{-1} \tag{2.34}$$

Taking advantage of the fact that $\mathbb{P}^{\mathrm{SC}}$ is identical for both phases (it is given by (2.30)), it is useful to note that (2.34) can also be expressed as:

$$0 = \overline{(\mathbb{C} - \mathbb{C}^{\mathrm{sc}}):(\mathbb{I} + \mathbb{P}^{\mathrm{sc}}:(\mathbb{C} - \mathbb{C}^{\mathrm{sc}}))^{-1}} \tag{2.35}$$

From this equation, it is readily seen that:

$$\mathbb{I} = \overline{(\mathbb{I} + \mathbb{P}^{\mathrm{sc}}:(\mathbb{C} - \mathbb{C}^{\mathrm{sc}}))^{-1}} \tag{2.36}$$

This further implies that $E_0 = E$ (2.32), and yields the simplified form of (2.34):

$$\mathbb{C}^{sc} = \overline{\mathbb{C}\colon(\mathbb{I} + \mathbb{P}^{sc}\colon(\mathbb{C} - \mathbb{C}^{sc}))^{-1}} \qquad (2.37)$$

In the case of an isotropic solid, the equivalent homogenized medium is isotropic as well. Equation (2.37) thus provides the following two scalar equations:

$$k^{sc} = (1 - \varphi_0)\frac{k^s}{1+\alpha^{sc}(k^s - k^{sc})/k^{sc}} \qquad (2.38)$$

$$\mu^{sc} = (1 - \varphi_0)\frac{\mu^s}{1+\beta^{sc}(\mu^s - \mu^{sc})/\mu^{sc}} \qquad (2.39)$$

In the general case, these equations are coupled because$\alpha \text{ and } \beta$ and depend on k^{SC} and μ^{SC} according to $\alpha = \frac{3k^s}{3k^s+4\mu^s} \text{ and } \beta = \frac{6(k^s+2\mu^s)}{5(3k^s+4\mu^s)}$. In the particular case of an incompressible solid phase (k^S → ∞), for which (2.38) is:

$$k^{sc} = (1 - \varphi_0)\frac{k^{sc}}{\alpha^{sc}} = \frac{1-\varphi_0}{3}(3k^{sc} + 4\mu^{sc}) \qquad (2.40)$$

That is:

$$\frac{k^{sc}}{\mu^{sc}} = \frac{4(1-\varphi_0)}{3\varphi_0} \qquad (2.41)$$

Combining (2.41) and (2.39) yields to:

$$k^{sc} = 4\mu^s\frac{(1-2\varphi_0)(1-\varphi_0)}{\varphi_0(3-\varphi_0)};\ \mu^{sc} = 3\mu^s\frac{(1-2\varphi_0)}{(3-\varphi_0)} \qquad (2.42)$$

The self-consistent scheme (2.42) predicts that the effective stiffness is a decreasing function of φ_0. However, the self-consistent estimate vanishes for $\varphi_0 = \frac{1}{2}$. This level of porosity is classically interpreted as a percolation threshold of the pores. Another point of view might consist in increasing the solid volume fraction: the self-consistent scheme would then predict that an effective stiffness appears beyond a solid volume fraction equal to ½.

2-4 Arching

2-4-1 Classical Theories

Arching theories have been reviewed extensively in [19]. The classical studies of the arching effect occurring in a soil mass begin by the investigation [20, 21]. This type of studies combines both experimental observations and theoretical derivation. In the following figure, the initial experiment used by Terzaghi and referred as the trap door is shown in (Figure 9):

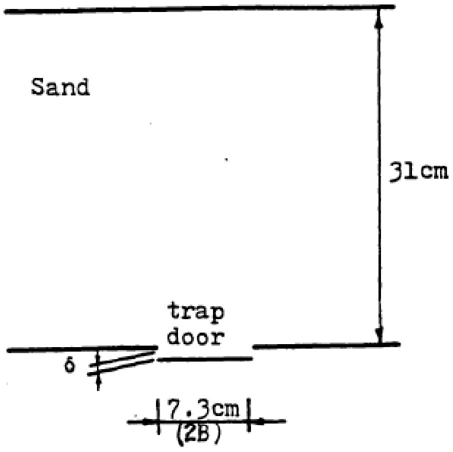

Figure 9– Trap door experiment by Terzaghi

This experiment highlights the redistribution of stresses in the soil mass. The shearing resistance tends to keep the yielding mass in its original position resulting in a change of the pressure on both of the yielding part's support and the adjoining part of the soil. If the yielding part moves downward (see Figure 9), the shear resistance will act upward and reduce the stress at the base of the yielding mass.

After investigating the experimental case of the trap door, Terzaghi has set a theoretical approach for the arching problem in sand under plane strain conditions. Using the following free body diagram for a slice of soil in the yielding zone [21]:

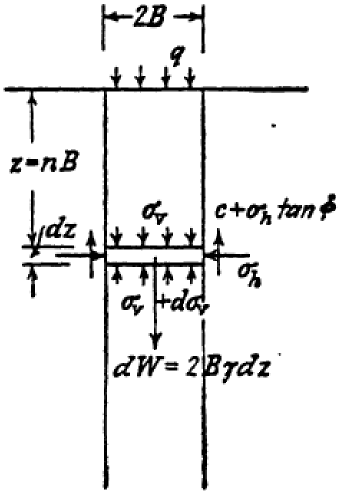

Figure 10– Free body diagram for a slice in the yielding zone

In Terzaghi's theory, using (Figure 10), the following assumptions are made:

- The sliding surface is assumed to be vertical
- The normal stress is uniform across horizontal section
- The coefficient K of lateral stress is a constant
- The cohesion c is assumed to be existing along the sliding surface

As a matter of consequences, the vertical equilibrium for the free body diagram can be written as follows:

$$2\mathrm{B}\gamma\mathrm{dz} = 2\mathrm{B}(\sigma_\mathrm{v} + \mathrm{d}\sigma_\mathrm{v}) - 2\mathrm{B}\sigma_\mathrm{v} + 2\mathrm{cdz} + 2\sigma_\mathrm{h}\mathrm{dz}\tan\phi \qquad (2.43)$$

In which:

- 2B = width of the yielding strip

- Z = depth
- Γ = unit weight of soil
- σv = vertical stress
- σh = horizontal stress = Kσv
- K = coefficient of lateral stress
- C = cohesion
- Φ = friction angle

Noting that in the middle of the soil column, σv equals the surcharge q at the ground surface, we get:

$$\sigma_{\mathrm{v}} = \frac{\mathrm{B}\left(\gamma - \frac{\mathrm{c}}{\mathrm{B}}\right)}{\mathrm{Ktan}\phi}\left(1 - \mathrm{e}^{-\mathrm{Ktan}\phi\frac{\mathrm{c}}{\mathrm{B}}}\right) + \mathrm{q}\mathrm{e}^{-\mathrm{Ktan}\phi\frac{\mathrm{c}}{\mathrm{B}}} \qquad (2.44)$$

The analytical theories closest to the problems considered in the following are all based on the work of Chelapati.

Chelapati's model is based on Finn's model. Finn presented closed form solutions for the change in vertical stress resulting from translation or rotation of a trap door. (Figure 11) (a) is the pure translation case and (Figure 11)(b) is the pure rotation case.

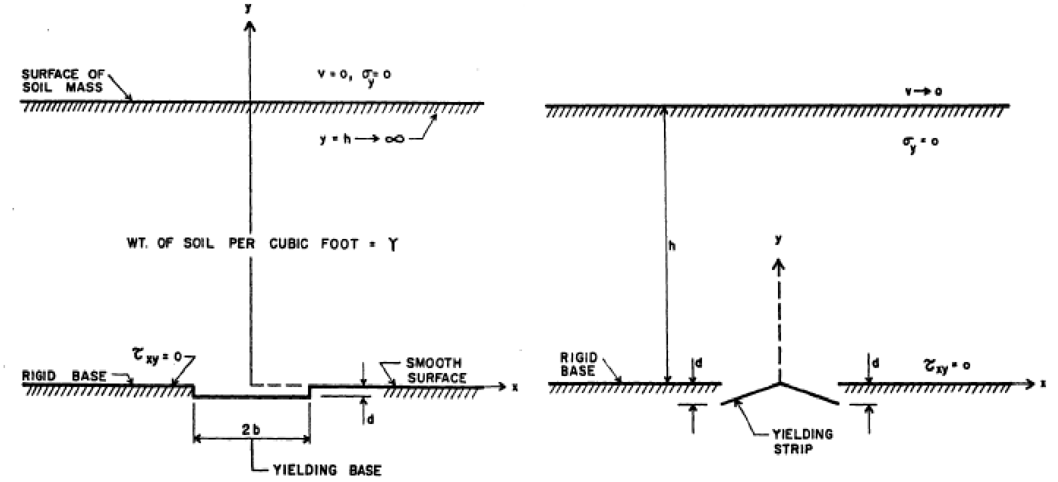

(a) Translational Yielding Base

(b) Rotational Yielding Base

Figure 11- Boundary conditions for soil mass with yielding base (Finn, 1963)

In these figures, the vertical displacement v and the vertical stressσ_y on the ground surface are both assumed to be equal to zero. A plane strain condition is assumed with the soil treated as an elastic medium with unit weight γ resting on a rigid horizontal boundary with a trap door located in it. The rigid base is considered frictionless $\tau_{xy} = 0$ initially but it then treated as frictional and cohesive later. The trap door has a width equal to $2b$. The depth of soil is assumed to be infinite: $h \rightarrow \infty$. The displacement of the trap door is d. Finn restricted his analysis to problems where displacements of the soil were very small and entirely elastic.

Infinite tensile stresses develop near the edges of the trap door, while infinite compressive stresses occur on the base next to the door. The results obtained by the theory of elasticity from Finn (1963) have been checked against available published experimental and field results. The stress distribution, the approximate location of the force resultants, and the influence of the various types of displacements predicted by the analysis were in reasonable agreement with the published results of Finn. However, one big obstacle to the determination of these values was the displacement d of the trap door. These predicted values were only good for very small d values.

In Finn's study, the depth of the soil was always taken as infinite which imposed restrictions in adapting the solution to practical problems of finite soil depth. Chepati (1964) presented a study using Finn's model but dealt with the stresses in a soil field of finite depth, h. The soil mass was again assumed to be a homogeneous, elastic, isotropic medium but subjected to high overburden pressure. The geometry and boundary condition of Chelapati's analysis is shown in (Figure 12):

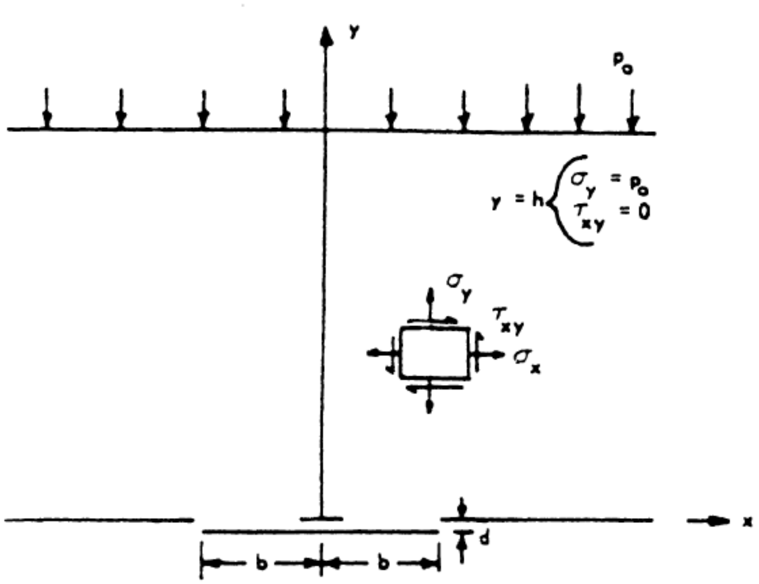

Figure 12- Boundary condition for Chelapati's analysis of arching in granular material

Using the model in (Figure 12), Chelapati superimposed stresses caused by the yielding trap door onto those due to surcharge load. The problem of infinite stresses at the trap door edges still existed. Since he considered granular soils in his study, and because granular soils cannot sustain tension, the stress on the door was assumed to be zero wherever tensile stresses were indicated. Chelapati used the method of series expansion to find the solutions in his study. Chelapati concluded from the results that arching for the cases in his study was dependent on three parameters, b/h, Ph/dE, and μ. For practical purposes, however, the effect of the Poisson's ratio, ν, can be neglected over a wide range of the other parameters.

Bjerrum, Frimann Clausen and Duncan (1972) developed a model giving approximate values for the change in vertical pressure at the center of a flexible section located within a rigid horizontal boundary. The variation of vertical pressure at the center was expressed as:

$$\Delta_p \approx \alpha \times \frac{\delta}{l} \times E \tag{2.45}$$

In which E is the elastic modulus of the soil and α is a coefficient whose values are between 0.3 and 1.0. The other parameters are shown in the layout (Figure 13):

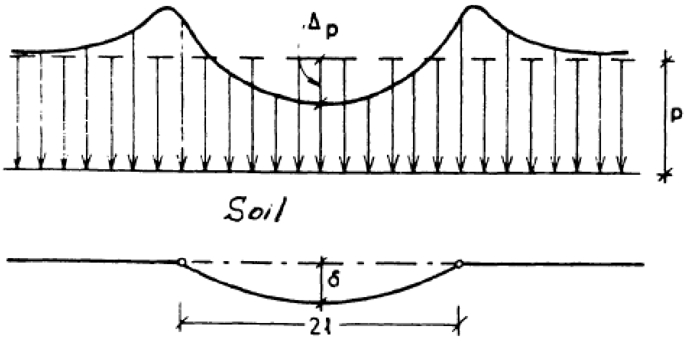

Figure 13- Arching model in the study of Bjerrum et al.

2-4-2 Arching Between Columns: Model of Hong, Lee and Lee [12, 22]

Arching occurs both in the embankment supported by jet-grouted columns and in the soil mass surrounding the columns. In a regularly jet-grouted soil, a differential settlement occurs because of the presence of stiffer jet-grouted columns. This differential settlement generates shear stresses within the embankment that increase the load on the pile while decreasing the load on the surrounding soil.

Soil arching develops in the embankment following a semi-cylindrical arch, with a thickness which is equal to the width of the cap as shown in (Figure 14):

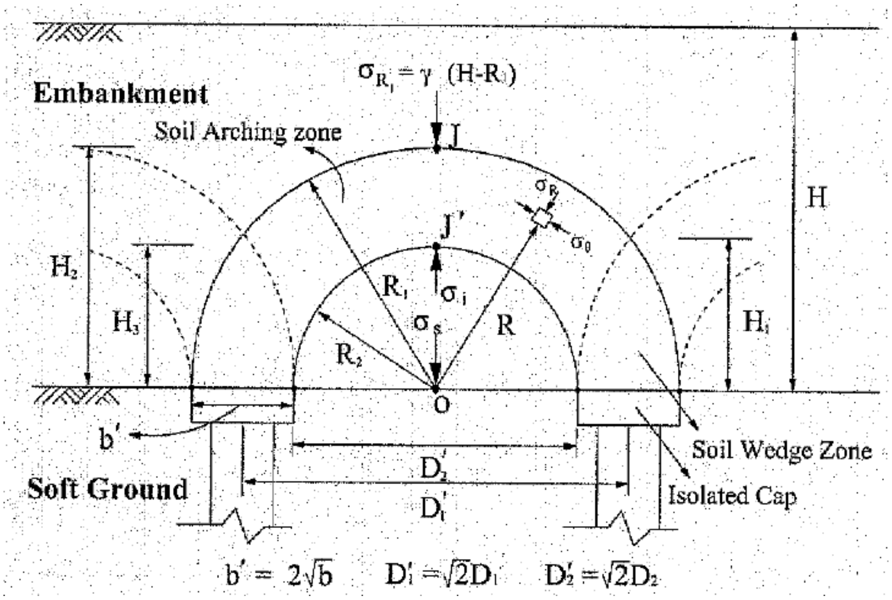

Figure 14- Arching model (taken from [12, 22])

The arch is oriented opposite in the soil mass. The model illustrated in Figure 1 has been used to model arching between isolated cap piles [2, 23].

2-4-3 Arching Behind Walls: Model Developed by Handy

The arching theory states that for an element of soil which moves relative to a non-moving element, in our case the jet-grouting columns, the force applied on the element below the one considered will be reduced from a normal state by the amount of friction between the soil mass and the columns (see Figure 15):

$$V + dV = V + \gamma B dh - 2 \times K\mu \frac{V}{B} dh \qquad (2.46)$$

Terzaghi provides a state of the art on the theories of soil arching in [20, 21], and gives a general empirical idea of the geometry of the sliding surfaces and zones of influence

Handy reviews some arching models in [24]. In this study, the following free body diagram is considered (Figure 15):

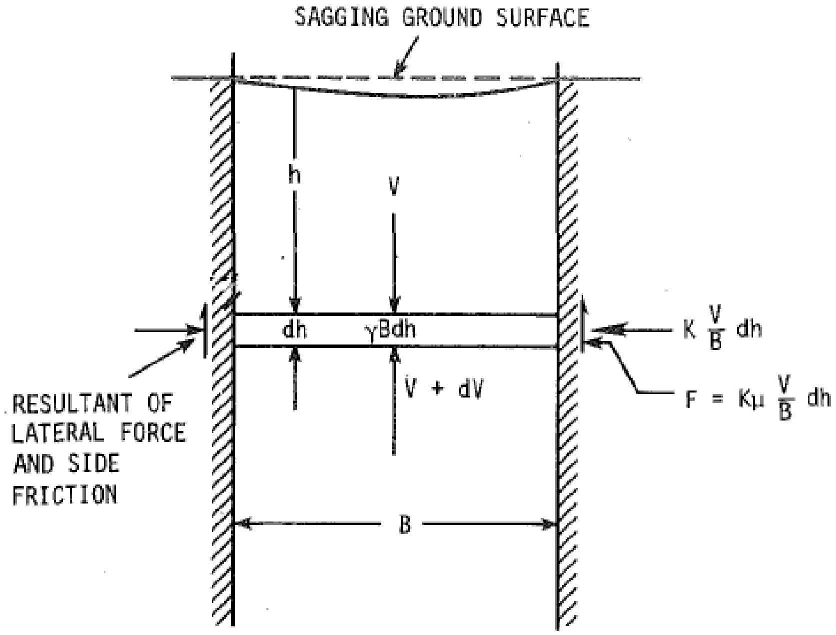

Figure 15- Body diagram considered by Handy

The objective of the modeling of arching effects is to find the orientation of the principal stresses developed in the soil mass. The arching slice-element of (Figure 15) is bounded by surfaces representing principal planes of zero shearing stress. The authors then consider the slice-element to be uniform in thickness and density which lead to a uniform weight throughout the arch. The result is that the shape of the arch is a catenary described by the following equation:

$$y = \frac{a}{2}\left[\exp\left(\frac{x}{a}\right) + \exp(-\frac{x}{a})\right] \tag{2.47}$$

Where a is a friction coefficient and x stands for the relative distance from the center line and has limits ± 1.

$$\frac{\mathrm{dy}}{\mathrm{dx}} = \frac{1}{2}\left[\exp\left(\frac{\mathrm{x}}{\mathrm{a}}\right) - \exp\left(\frac{\mathrm{x}}{\mathrm{a}}\right)\right] = -\cot\theta \tag{2.48}$$

For fully developed wall friction, $\theta_{\mathrm{max}} = \pm(45 + \frac{\phi}{2})$ when $\mathrm{x} = \pm 1$ at the walls, enabling evaluation of a.

Published studies relate the following parameters and variables:

- Major principal stress σ_1
- Distance between the two walls
- Vertical displacement d
- Unit weight of the soil
- Internal friction angle
- The earth pressure coefficient K

[25] uses the following formula to relate the load supported by reinforcement (P) to the surface load transmitted by the ground (q):

$$\mathrm{P} = \frac{\mathrm{qB}\sqrt[2]{1+\frac{16\mathrm{d}^2}{\mathrm{B}^2}}}{8\mathrm{d}} \tag{2.49}$$

The problem of this theory is that the major principal stress is not depending of the depth at which the arching is considered. In reality, there is a direct connection between the major principal stress and the depth: $\sigma_{\mathrm{v}} = \gamma' \times \mathrm{z}$ where z is the depth and $\gamma' = \mathrm{y} - \gamma_{\mathrm{w}}$.

There is a non-linear relationship, depending on depth, between the major principal stress and the horizontal stress applying on the jet-grouting columns as a function of the depth [24]. Horizontal stress represents the friction developed between the grouted structure and the soil mass when arching takes place.

CHAPTER III

MODEL

3-1. Prediction of the Injection Radius

The first step of the dimensioning procedure consists in determining the extent of the injected zone. The diameter of the grouted column is then considered as the size of the Representative Elementary Volume (REV), at the scale at which the elastic properties of soilcrete are homogenized (in Step 2). The injection radius $\mathrm{R_{injection}}$ is defined as half of the diameter of the soilcrete column. The domain under study is a ground layer of thickness $\mathrm{t_{pancake}}$ (“pancake thickness”), surrounding the nozzle. For $0 \leq \mathrm{r} \leq \mathrm{R_{injection}}$, the ground is improved (soilcrete). For $\mathrm{r} > \mathrm{R_{injection}}$, the ground may be subjected to stress perturbations due to the injection, but particles are not mixed with grout (solid grains only). It is assumed that the injection velocity and the grout elastic moduli (bulk and shear moduli) are known.

3-1-1 Background on Fluid Mechanics [26]

3-1-1-1 The Basic Equations

Conservation of mass is the most basic principle. In general, the fluid density ρ may vary in response to changes in the fluid temperature and/or pressure. For a fixed control volume Ꝟ enclosed by the surface S, a general statement of mass conservation is:

$$\frac{\partial}{\partial \mathrm{t}}\int \rho \mathrm{d}\text{Ꝟ}_{\text{Ꝟ}} + \int \rho\vec{\mathrm{v}}\cdot\vec{\mathrm{n}}\mathrm{dS}_{\mathrm{S}} \qquad (3.1)$$

in which $\vec{v}$ is the velocity at a point and $\vec{\mathrm{n}}$ is an outer normal unit vector to the surface S, and t is time. The first term represents the accumulation of mass over time in the control volume; for steady flows it is zero. At a surface point the dot product $\vec{\mathrm{v}}\cdot\vec{\mathrm{n}}$ gives the component of the velocity which crosses the surface, so the second computes the net outflow of fluid across the entire control surface. For steady incompressible flow of a liquid in a pipe, the conservation of mass is generally referred to as the continuity principle, or simply continuity and it is written

$$Q = \int \upsilon dA_A = V_1A_1 = V_2A_2 \qquad (3.2)$$

in which Q is the volumetric discharge through a pipe cross section, which can also be written as the product of the mean velocity V and cross-sectional area A of the pipe.

The second, equally important, principle is the work-energy principle, sometimes called simply the energy principle. Some also call it the Bernoulli equation, but in general it is distinctly more than that. For a steady one-dimensional flow of a liquid in a pipe, per unit weight of fluid, the principle can be written between two sections or stations as

$$\frac{{V_1}^2}{2g} + \frac{p_1}{\gamma} + z_1 = \frac{{V_2}^2}{2g} + \frac{p_2}{\gamma} + z_2 + \sum h_{L_{1-2}} - h_m \qquad (3.3)$$

In this equation $\frac{V^2}{2g}$ is the velocity head or kinetic energy, $\frac{p}{\gamma}$ is the pressure head or flow work, and z elevation head or potential energy, all per unit weight. If the last two terms on the right were absent, the equation would be the classical Bernoulli equation. The last two terms, however, are extremely important in the study of the hydraulics of pipe lines. The head loss term, or the accumulated energy loss per unit weight, $\sum h_L$, is the sum, between sections 1and 2, of the individual head losses in the reach caused by frictional effects. The last term, h_m, is the mechanical energy per unit weight added to the flow by hydraulic machinery. A pump adds energy to the flow h_m is then positive and called h_p; a turbine extracts energy from the flow so h_m would then be negative and called h_t.

Fluid power, sometimes denoted by P, is the product of the energy gain or loss per unit weight h_m and the weight rate of flow $Q\gamma$, or $P = Q\gamma h_m$. Depending on the purpose of the computation, and efficiency factor η may be used as a multiplier or divisor of the power.

The last major principles considers linear momentum, which is governed by the impulse-momentum equation

$$\frac{\partial}{\partial t}\int \vec{v}\rho d\cancel{V}_{\cancel{V}} + \int \vec{v}(\rho\vec{v}\cdot\overrightarrow{n})dS_S = \vec{F}_{net} = \vec{F}_s + \vec{F}_b \qquad (3.4)$$

in which the net force on the contents of the control volume, fluid and solid, which can be divided into surface forces and body forces, is equal to the rate of accumulation of momentum within the control volume plus the net flux of momentum through the surface of the control volume. In a steady flow the first term is again zero. For steady, incompressible, one-dimensional flow through a pipe, the component momentum equation along the direction of flow is:

$$\vec{F}_{net} = \rho Q(\vec{V}_2 - \vec{V}_1) \qquad (3.5)$$

in which we assume flow into the pipe at the left section, section 1, and flow from the pipe at the right section, section 2. If the pipe cross-sectional area is constant between the end sections and the pipe is straight, then the velocities are equal, and the equations simplifies further to $\vec{F}_{net} = 0$. Since equation (3.5) is a vector equation, it can always be written in component form; for two-dimensional flow in the x-y plane, the components of this equation are:

$$\sum F_x = (\rho Q V_x)_2 - (\rho Q V_x)_1 = (\rho A {V_x}^2)_2 - (\rho A {V_x}^2)_1 \qquad (3.6a)$$

$$\sum F_y = (\rho Q V_y)_2 - (\rho Q V_y)_1 = (\rho A {V_y}^2)_2 - (\rho A {V_y}^2)_1 \qquad (3.6b)$$

3-1-1-2 Head Loss Formulas

The head loss term in equation (3.3) is responsible for representing accurately two kinds of real-fluid phenomena, head loss due to fluid shear at the pipe wall, called pipe friction, and additional head loss caused by local disruptions of the fluid stream. The head loss due to pipe friction is always present throughout the length of the pipe, The local disruptions, called local losses, are caused by valves, pipe bends, and other such fitting. Local losses may also be called minor losses if their effect, individually and/or collectively, will not contribute significantly in the determination of the flow; indeed, sometimes minor losses are expected to be inconsequential and are neglected. Or a preliminary survey of design alternatives may ignore the local or minor losses, considering them only in a later design stage. The present study only uses to kind of losses, the regular loss (or pipe friction) and the singular loss (or local loss):

First, the regular loss. If we were to select a small cylindrical control volume within a section of circular pipe, with coordinates s in the flow direction and r radially, in steady flow subject this volume to analysis by the momentum equation (3.4), it has been found that the mean fluid shear stress τ, as function of the radius r from the pipe centerline, is:

$$\tau = -\frac{r}{2}\gamma\frac{\partial}{\partial s}(\frac{p}{\gamma} + z) \qquad (3.7)$$

from which two important facts are learned:

1. The fluid shear stress τ varies linearly in a pipe cross-section, from zero at the centerline to a maximum, called τ_w, at the pipe wall where r=D/2.
2. In the absence of a streamwise gradient of the piezometric head $(\frac{p}{\gamma} + z)$, the fluid shear stress will be zero, and consequently no flow will exist at that section.

If the control volume is now expanded to fill the pipe cross-section and integrate equation (3-1-6) over a length L of pipe of constant diameter, it is found that the frictional head loss $\mathrm{h_L}$ over that length is directly related to the wall shear stress τ_w via:

$$\tau_w = \gamma h_L \frac{D}{4L} \tag{3.8}$$

But this equation does not relate head loss to the mean velocity V or the discharge Q.

The completely general functional relation $\tau_w = F(V, D, \rho, \mu, e)$ between the wall shear stress τ_w and the mean velocity V, pipe diameter D, fluid density ρ, and viscosity μ, and the equivalent sand-grain roughness e can be reduced by dimensional analysis to

$$\frac{\tau_w}{\rho V^2} = F\left(\frac{VD\rho}{\mu}, \frac{e}{D}\right) = \frac{f}{8} \tag{3.9}$$

The combination of equation (3.8) and (3.9) to eliminate the wall shear stress produces the fundamentally most sound and versatile equation for frictional head loss in a pipe, the Darcy-Weisbach equation:

$$h_f = f\frac{L}{D}\frac{V^2}{2g} = f\frac{L}{D}\frac{Q^2}{2gA^2} \tag{3.10}$$

In equation (3-2-9) the friction factor f is introduced as a shorthand notation for the function F. It is a function of the pipe Reynolds number $\mathrm{Re} = \frac{VD\rho}{\mu} = \frac{VD}{\nu}$ and the equivalent sand-grain roughness factor e/D. For each pipe material either a single value or range of e/D values has been established in the literature.

Then comes the singular loss. A local loss is any energy loss, in addition to that of pipe friction alone, caused by some localized disruption of the flow by some flow appurtenances, such as valves, bends, and other fittings. The actual dissipation of this occurs over a finite but not necessarily short longitudinal section of the pipe line, but it is accepted convention in hydraulics to lump or concentrate the entire amount of this loss at the location of the device that causes the flow disruption and loss. If a loss is sufficiently small in comparison with other energy losses and with pipe friction, it may be regarded as a minor loss. Often minor losses can be so large or significant that they will never be termed a minor loss, and they must be retained; one example is a valve that is only partly open.

Normally, theory alone is unable to quantify the magnitudes of the energy losses caused by these devices, so the representation of these losses depends heavily upon experimental data. Local losses are usually computed from the equation

$$h_L = K_L \frac{V^2}{2g} \tag{3.11}$$

in which V=Q/A is normally the downstream mean velocity. For enlargement the following alternative formula applies:

$$h_L = K_L \frac{(V_1 - V_2)^2}{2g} \tag{3.12}$$

in which V_1 and V_2 are, respectively, the upstream and downstream velocities. In equation (3.12) the loss coefficient K_L is unity for sudden enlargements. The head loss for flow from a pipe into a reservoir is a special but important case of equation (3.12), called the exit losses; in this case, $K_L = 1$ and $V_2 = 0$, independent of the geometric details of the pipe exit shape.

The energy losses for common valves and pipe fittings are mostly consequence of fluid turbulence caused by the device rather than by secondary motions which persists downstream. Normally a locally accelerating flow will cause much less energy loss than does a decelerating flow. If decelerating is too rapid, it causes separation, which results in additional turbulence and a high velocity in non-separated region.

3-1-2 Model on Singular Pressure Drops

In a first approach, the soilcrete column diameter is computed by estimating the grout pressure drops occurring during the injection. Grout injection is viewed as a pipe fluid flow problem. The pipe diameter is *d*. In the absence of reference data, it is assumed that $t_{pancake}$ is equal to five times the nozzle diameter (Figure 16).

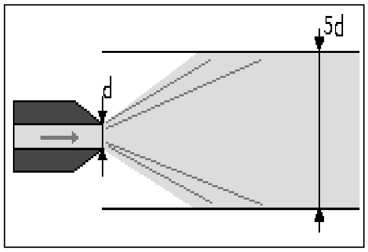

Figure 16- Schematic representation of the nozzle and surrounding injected zone

Regular pressure drops (J_r) are defined as the difference between the injection pressure at the nozzle ($P_{injection}$) and grout pressure in the middle of the injected layer (noted u):

$$J_r = P_{injection} - u \tag{3.13}$$

Noting V_c the average grout velocity in the injected layer, and c the grout kinematic viscosity, Reynolds number may be computed as [27]:

$$R_e = \frac{t_{pancake}V_c}{c} \tag{3.14}$$

Using Blasius law for a turbulent pipe flow, the friction coefficient (λ) writes:

$$\lambda = 0.3164(R_e)^{-0.25} \tag{3.15}$$

If no other dissipation phenomenon than regular pressure drops occur during jet-grouting, the injection radius can be determined by [28]:

$$R_{injection} = \frac{2t_{pancake}J_r}{\lambda\rho(V_c)^2} \tag{3.16}$$

In which ρ is the mass density of grout. This first prediction model has been calibrated using data on injection velocity and corresponding injection radius, which are available in case studies published in [1, 15, 28, 29].

The plot is presented in (Figure 17). The model presented in equations (3.13 to 3.16) only accounts for regular pressure drops, and for no other dissipation phenomena. As a result, the injection radius predicted by the model is over-estimated, as could be expected.

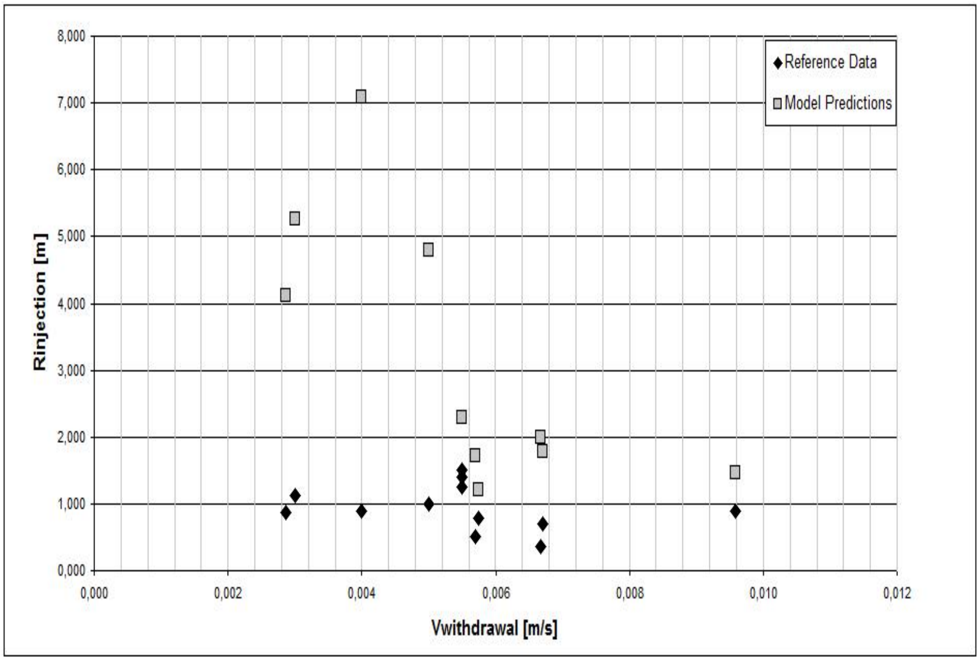

Figure 17– Radius of injection [m] versus the velocity of the cement in the ground for the reference data and the first model predictions [m/s]

The values of the theoretical radius of injection are larger than the measured values of the radius of injection. The accuracy of the results greatly depends on the velocity of the cement in the ground. In fact the less fast the grout is, the less accurate the results are with a worst estimation of the radius of injection seven times greater than the one measured.

The approach is refined to account for singular pressure drops, representing energy loss due to the geometry of the fictitious pipe. It is assumed that around the nozzle, the pipe is a truncated cone rather than a tube. The minimum diameter of the pipe is equal to d, the diameter of the nozzle. The maximum diameter of the pipe is $\mathrm{t_{pancake}}$, the thickness of the injected layer. A geometric parameter (ζ) is introduced:

$$\zeta = \left(\frac{\mathrm{d}}{\mathrm{t_{pancake}}}\right)^4 \tag{3.17}$$

Singular pressure drops may be computed as [27]:

$$\mathrm{J_s} = \rho\zeta(\mathrm{V_{injection}})^2 \tag{3.18}$$

in which $\mathrm{V_{injection}}$ is the injection velocity (grout velocity at the nozzle head). With the assumption $\mathrm{t_{pancake}} = 5\mathrm{d}$ (Figure 16), we have $\zeta = 0.0016$. The injection radius is thus related to regular and singular pressure drops by [27]:

$$\mathrm{R_{injection}} = \frac{1}{2} - \frac{\mathrm{J_s}}{\mathrm{J_r}} \tag{3.19}$$

The injection radius is determined by combining equations (3.17, 3.18 and 3.19). Calibration results are provided in the figure below (Figure 18):

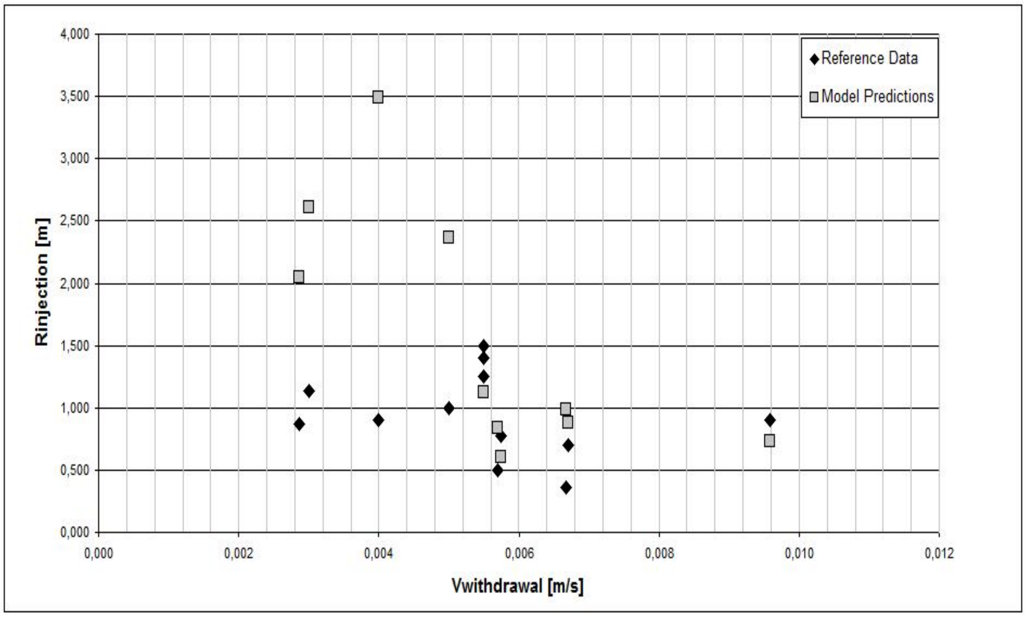

Figure 18- Radius of injection [m] versus the velocity of the cement in the ground for the reference data and the second model predictions [m/s]

The predictions of the improved hydraulic model are compared to in situ measurements published in the literature in (Figure 18). It appears that the predictions of this second model are closer to the radius measurements. The accuracy of the results still greatly depends on the velocity of the cement in the ground: the results are closer to the measurements for high injection rates. In the worst cases, the radius of injection predicted by the improved hydraulic model is four times larger than the one measured in situ. However, the second model underestimates the injection radius for the two highest injection velocities reported in the literature.

3-1-3 Model Based on Energy Balance

3-1-3-1 Energetic Model 1

A new modeling approach is proposed to improve the accuracy of the results. A lower predicted radius will lead to choose higher injection pressures, and thus to over-size the soilcrete column, which is conservative. The objective is thus to control the error to get a lower estimate of the injection distance rather than a higher radius estimate, and to reduce the error as much as possible.

The kinetic energy (expressed in MJ) of the grout injected during one nozzle revolution corresponds to the kinetic energy of 0.09m^3 of grout (typical grout volume injected during one revolution):

$$K = \frac{0.09}{2}\rho(V_{injection})^2 \tag{3.20}$$

Considering that during injection, the grout describes a spherical spiral, the radius of which varies continuously from $R_{injection}$ to 0 into 360°, the work (W) of the force required to expel solid grains and pore water from the injected volume is:

$$W = \frac{5\pi}{6}t_{pancake}\left(P_{injection} - u\right)\left(R_{injection}\right)^2 = A_1(R_{injection})^2 \tag{3.21}$$

When the energy losses fully compensate the kinetic energy input, we have:

$$K = W \tag{3.22}$$

After combining equations 8, 9 and 10, the injection radius turns to be:

$$\text{Radius} = \sqrt{\frac{K}{W}} \tag{3.23}$$

The predictions of this first energetic model are compared to the in situ injection radius measurements in (Figure 19). The model predictions over-estimate the injection radius for all the injection velocities tested. As explained above, this is not satisfactory to get conservative predictions. However, the accuracy of the energetic approach is less dependent on the injection velocity than the hydraulic approach (Figure 19). The objective of the remainder of the present study is to improve this first energetic model to have a lower bound of the injection radius.

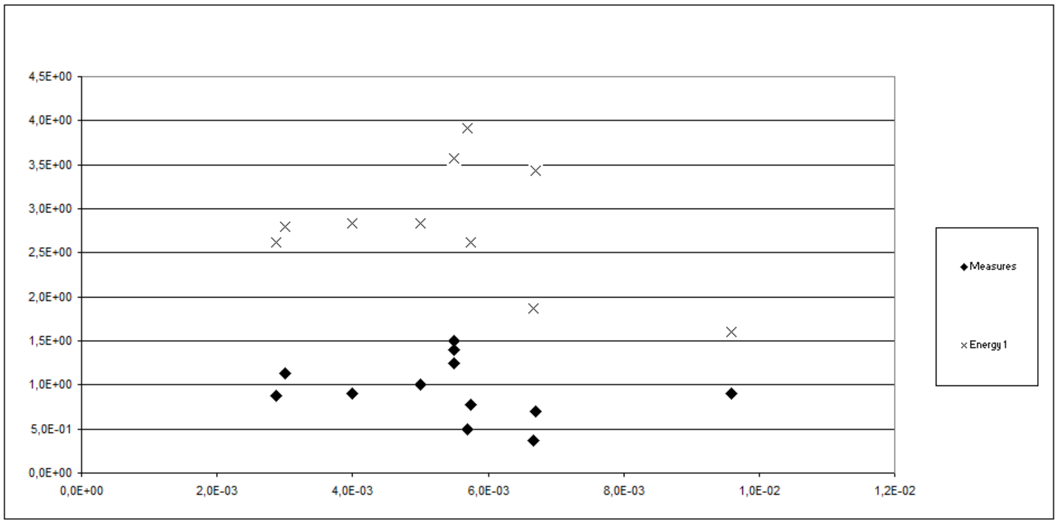

Figure 19- Radius of injection [m] versus the velocity of the cement in the ground for the first energetic model and the reference data [m/s]

3-1-3-2 Energetic Model 2

In order to get a lower bound for the injection radius, dissipation due to friction is accounted for in addition to the work of the force required to expel water and solid grains from the injected zone is accounted for, but also the work of the force generated by the dynamic viscosity of the grout moving between the two planes delimiting the cement pancake (Figure 20). The force associated to viscosity is defined as:

$$F = \mu A \frac{dv}{dz} \tag{3.24}$$

where A is the area of a layer, μ the dynamic viscosity and $\frac{dv}{dz}$ the shear rate.

In this second energetic model, the following assumptions are made:

- The area of injection is assumed to have the shape of a spherical spiral, the radius of which varies continuously from $R_{injection}$ to 0 into 360°.
- The area where the force generated by the dynamic viscosity is applied is not a plane. The model accounts for the geometry of the grains. The surface

corresponds to the area of a disc of radius equal to the radius of a grain times the number of grains in 90 L of soil.

- The force generated by the dynamic viscosity works over a distance equal to one seventh of $R_{injection}$. This ratio has been fitted to give model predictions as close as possible to the in situ radius measurements. This attenuation ratio may be explained by the fact that the loss of energy due to viscosity is more important where the soil grains are not totally invaded by cement. The work of the force associated with the cement dynamic viscosity is noted *S* [MJ].

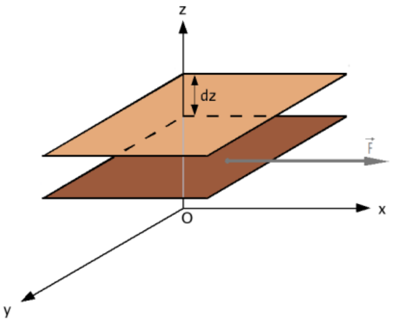

Figure 20- Representation of the work done by the force generated by the dynamic viscosity

Let's recall that the work of the force necessary to expel the water and the grains from the injected soil mass is (equation 3.21):

$$W = \frac{5\pi}{6} t_{pancake} \left(P_{injection} - u\right) \left(R_{injection}\right)^2 = A_1 (R_{injection})^2$$

On the other hand, the work of the force associated to the cement viscosity is, using [29]:

$$S = \frac{1}{7} \frac{0.279 \times 30.93 \times \pi \rho c \times V_{withdrawal}}{1000000 t_{pancake}} (R_{injection})^4 = A_2 (R_{injection})^4 \qquad (3.25)$$

The energy balance:

$$\mathrm{K} = \mathrm{W} + \mathrm{S} \tag{3.26}$$

leads to solve an equation of the form:

$$\mathrm{K} = \mathrm{A}_1\mathrm{X}^2 + \mathrm{A}_2\mathrm{X}^4 \tag{3.27}$$

in which K, A_1, and A_2 are known, and X is the unknown radius.

The predictions of the second energetic model are compared to in situ injection radius measurements published in [1, 15, 28, 29] in (Figure 21). As expected, the theoretical results are below the measured ones for all the different values of the velocity of the grout in the soil. Nonetheless, it appears that the accuracy of the results depends on the velocity of the grout in the soil.

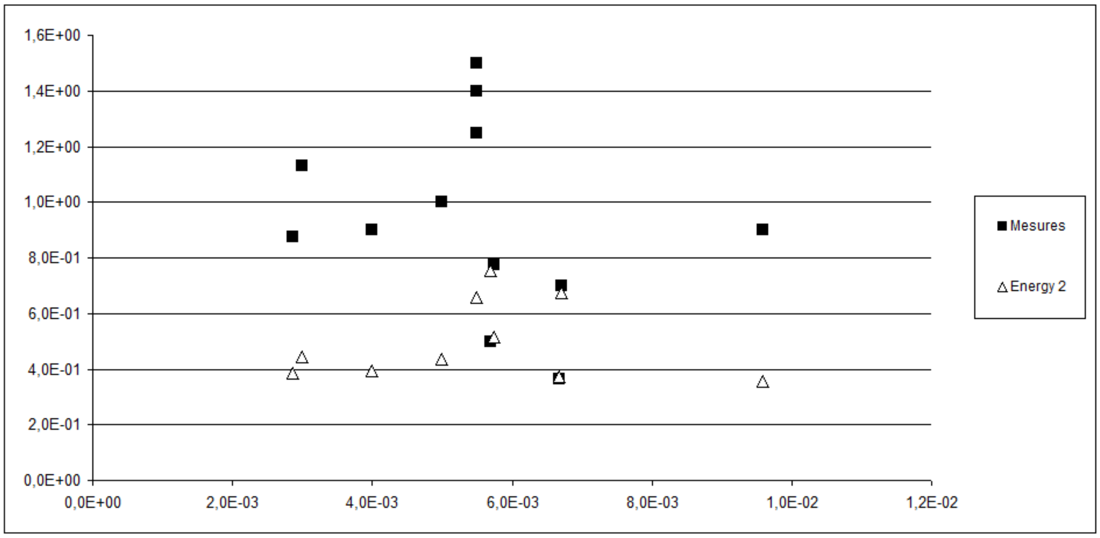

Figure 21- Radius of injection [m] versus the velocity of the cement in the ground for the second energetic model and the reference data [m/s]

3-1-3-3 Energetic model 3

The energetic potential defined in (3.27) represents the energy required to dislodge the solid grains from the ground mass surrounding the nozzle and the energy dissipated by friction between the remaining grains and the grout. Based on this simplifying assumption, the net energy representing the energy dissipated by friction during grout penetration is equal to the work of the shear force acting on soil/grout plane interfaces in the pancake. The average shear force resulting from the grout viscosity is expressed as:

$$F = \mu \mathrm{A} \frac{\mathrm{dv}}{\mathrm{dz}} = \mu \mathrm{A} \frac{\mathrm{V_c}}{\mathrm{t_{pancake}}} \tag{3.28}$$

in which v is the velocity of grout (depending on both coordinates r and z), and A is the area of the contact surface between the grout and the soil mass.

This assumption is not right close to the nozzle where the high pressure and high velocity grout changes the structure formed by the grains. However close to the nozzle the material composing the heart of the jet-grouted column is going to be cement (whose mechanical properties are known) and this zone of genuine cement is not interfering with the dimension of the radius of injection.

Considering that the grout spreads in a volume forming a cylinder of radius $\mathrm{V_{injection}}$ and of thickness $\mathrm{t_{pancake}}$ around the nozzle, and assuming that the soil is already injected below the pancake considered, the contact surface between the grout and the soil is: $\mathrm{A} = \pi(\mathrm{R_{injection}})^2$. The geometric assumptions in the computation of A are further made less constraining by introducing a parameter N to better calibrate the model (3.30 and 3.31). Assuming that F works over a distance of one meter to the nozzle (usual soilcrete column diameter), the work (in MJ) of the force associated to grout viscosity (energy dissipated by friction) writes [27]:

$$\mathrm{S} = \frac{1}{10^6} \pi(\mathrm{R_{injection}})^2 \mathrm{c} \frac{\mathrm{V_c}}{\mathrm{t_{pancake}}} \times 1 = \mathrm{A_3}(\mathrm{R_{injection}})^2 \tag{3.29}$$

The energy balance equation is expressed as:

$$\mathrm{K} = \mathrm{W} + \mathrm{NS} \tag{3.30}$$

in which N is a model parameter, controlling the influence of the dissipation induced by the grout viscosity. Combining equations 3.20 to 3.31 and 3.29 to 3.30 provides the injection radius:

$$R_{\text{injection}} = \sqrt{\frac{K}{A_1+NA_3}} \qquad (3.31)$$

Calibration results for the model based on energy balance are provided in Chapter IV.

All the models are using the pore water pressure in the calculations. This pore water pressure is connected to the depth at which the pancake is located.

The design of the column will follow the scheme presented below (Figure 22):

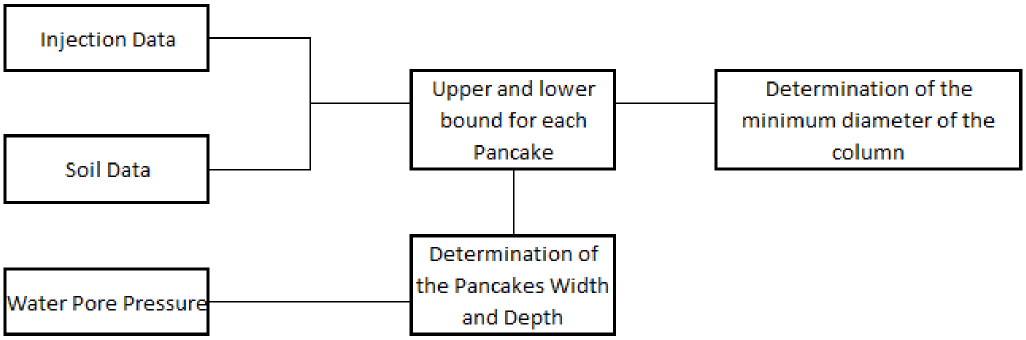

Figure 22- Scheme for the determination of the diameter of the column for designing purpose

3-2 Hollow Sphere Model

The purpose of this section is to introduce a homogenization scheme to compute the elastic moduli of soilcrete. The proposed approach is dedicated to coarse-grained soils, typically sands, in which hydraulic fracturing is unlikely to occur. For simplicity, the hollow sphere model is chosen to illustrate the computational approach. It is assumed that solid grains do not contribute to the mechanical strength of soilcrete. Grains are considered as void inclusions embedded in a grout matrix. Accordingly, the grouted soil is considered as a porous medium constituted of a grout matrix and void pores. The hollow sphere model is a pure illustrative case, which cannot be used for practical purposes. The objective is to homogenize the elastic properties of the injected zone, the dimension of which is assumed to be determined from the model explained in the preceding section. The injection radius defines the size of the Representative Elementary Volume (REV) considered for homogenization. The simplest approach consists in considering the REV of soilcrete as one hollow sphere. The sphere cavity represents the fictitious pore space (representing soil grains), and the solid shell represents the solid matrix (made of grout). If the hollow sphere REV is subjected to isotropic stress and strain conditions, the macroscopic bulk modulus of the hollow sphere ($\mathrm{k_{hs}}$) writes [27]:

$$\mathrm{k_{hs}} = \mathrm{k_c}\frac{4\mu_c(1-\varphi)}{3\varphi \mathrm{k_c}+4\mu_c} \qquad (3.32)$$

in which $\mathrm{k_c}$ and μ_c are the bulk and shear moduli of grout, respectively. φ is the porosity of the homogenized medium (representing the volumetric fraction of the sand grains in the soilcrete REV). To satisfy the requirements of the theory of homogenization [18], the separation-of-scale condition imposes that the dimension of the pores (inner hollow sphere radius) should be at least three orders of magnitude less than the dimension of the REV (external hollow sphere radius). The basic hollow sphere model is thus only valid for very low porosity media, which is not satisfactory in the present case. Following the approach of Hashin, the REV is considered as an assemblage of hollow spheres [27]. The inner radius of each hollow sphere is small enough compared to the REV size to satisfy the separation-of-scale requirement. Noting A_i the inner radius of the *i-th* hollow sphere, the porosity of the REV is equal to:

$$\varphi = \frac{\sum_{i}\frac{4\pi}{3}(A_i)^3}{V_{REV}} = f\alpha \qquad (3.33)$$

in which V_{REV} is the volume of the REV. a is the cumulated porosity of all hollow spheres present in the REV (not accounting for the void space between hollow spheres). Noting B_i the external radius of the *i-th* hollow sphere f is the smallest ratio $\frac{A_i}{B_i}$ that ensures that the hollow spheres occupying the REV do not overlap. A lower bound and an upper bound for the macroscopic bulk modulus of the REV (k_{hom}) can be determined by deriving the theorem of minimum complementary energy and the theorem of minimum potential energy [27]:

$$\frac{1}{k_{hom}} \leq \frac{\alpha}{k_{hs}} + \frac{1-\alpha}{k_c} \qquad (3.34)$$

$$\frac{1}{k_{hom}} \geq \frac{1}{(1-\alpha)k_c + \alpha k_{hs}} \qquad (3.35)$$

In the following, equation (3.35) is used to have a lower bound of the homogenized bulk modulus of soilcrete. Using this lower bound to predict the properties of the ground improved by jet-grouting is a conservative approach. In general k_c and μ_c are known (chosen by the engineer). φ is the volume fraction of the solid grains in soilcrete. It can be determined by comparing the weight of a grout sample to the weight of a soilcrete sample after mixing. Assuming that the problem is one-dimensional (radial distribution of stress and strain around the nozzle), (3.32) can be used to get k_{hs}. The remaining unknown in (3.35) is α, which can be determined if f is known (3.34).

A calibration process is proposed to relate f to k_{hom} The REV size is considered equal to $R_{injection}$ (determined in Step 1). It is assumed that $\varphi = 0.26$ (low volume fraction of grains after injection and mixing). A standard value is chosen for the grout Poisson's ratio (0.25). Nine case studies [29] are used to get reference values for the soilcrete bulk modulus ($\mathrm{k_{hom}}$) with the corresponding grout Young's modulus. Inputs are thus: $\mathrm{k_c}$, μ_c and φ and f is adjusted iteratively to ensure that the lower bound computed from (3.35) equals $\mathrm{k_{hom}}$ with less than 3% of error. The variations of f with $\mathrm{k_{hom}}$ are plotted in (Figure 23).

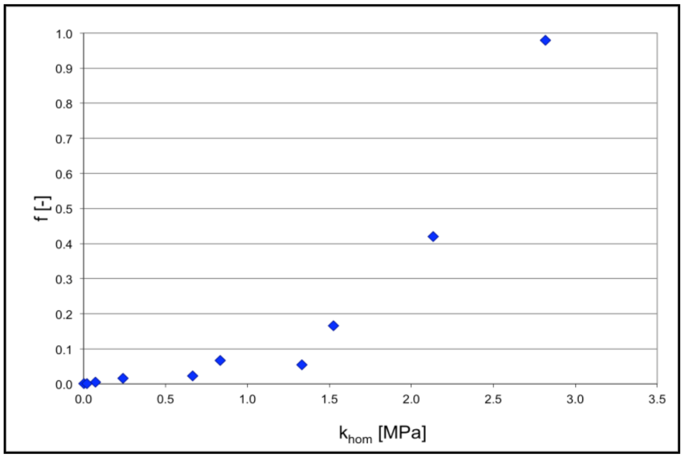

Figure 23- Parameter f versus homogenized soilcrete bulk modulus

It appears that f varies between 0 and 1 for a small range of values of $\mathrm{k_{hom}}$. In other words, there is no typical value of f for typical values of $\mathrm{k_{hom}}$. It is thus impossible to set f as a fixed model parameter. Further work needs to be done to determine the space distribution of the sand grains in the injected zone, and to account for the elastic properties of the grains in the homogenization scheme.

3-2-1 Averaging Technique Accounting for Grain Elastic Properties

Averaging and homogenization techniques have been reviewed in order to account for the mechanical properties of the particles of the genuine soil in the computation of soilcrete moduli [18]. In the simplest approaches, the volume fraction of each soilcrete component (solid, grains and cement) are used as weights in the computation of soilcrete averaged properties. More complex techniques require the introduction of strain concentration tensors.

3-2-2 Averaging Method

In the model described below, the main assumptions are:

- The grains are perfectly compacted together
- All the grains have the same radius
- The principal strain is 0.0025

Because the grains of soil are supposed to be perfectly compacted, the spatial ratio of the occupancy of the initial soil is 0.74 (close-packing of equal spheres). The REV is the smallest volume where the spatial ratio occupancy can be observed. Also, the boundary conditions are far enough for the hypothesis on the principal stress to be realist. As a consequence, the spatial ratio of the occupancy of the grout is 0.26. So the formula to calculate the average elasticity tensor is:

$$\bar{\mathbb{C}} = 0.26\mathbb{C}^{\mathrm{g}} + 0.74\mathbb{C}^{\mathrm{s}} \tag{3.36}$$

where $\mathbb{C}^{\mathrm{g}}$ is the elasticity tensor of the grout and $\mathbb{C}^{\mathrm{s}}$ is the elasticity tensor of the soil.

Soilcrete stiffness tensor has been computed by using the preceding equations, with soil and grout elastic moduli found in the literature for a series of case studies [1, 6, 7, 14, 29, 30, 31, 32, 33, 34, 35, 36, 37]. Poisson's ratio is generally not given. It has been assumed that Poisson's ratio was equal to 0.25 for both the soil and the grout. Soilcrete compressive strength is computed by assuming that plasticity occurs for a principal strain equal to 0.0025 (this corresponds to the value used for concrete) (Figure 24):

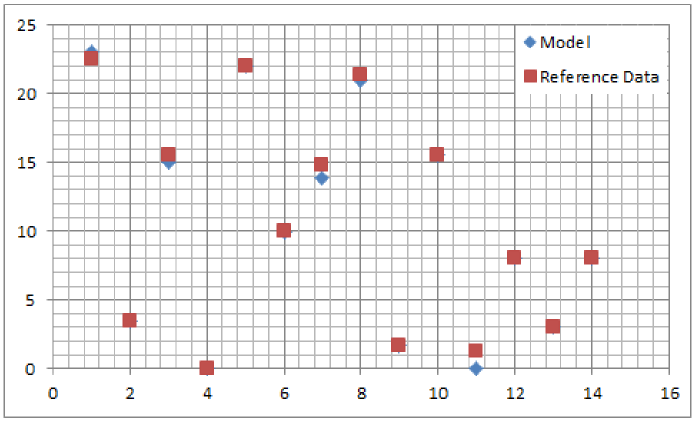

Figure 24- Uniaxial compressive strength [MPa] of soilcrete: model predictions versus data found in the literature (x-axis is the number of the case studied)

The errors made in the model predictions are around 15%. The problem of this model is that assuming a perfect particle packing is not realistic. Soil particles are dislodged during grout injection.

3-2-3 Eshelby's Model

Denote the elasticity tensor of Ω_α by $\mathbf{C}^\alpha$ and set:

$$\mathbf{A}^\alpha = (\mathbf{C}:\mathbf{C}^\alpha)^{-1}:\mathbf{C} \qquad (3.37)$$

The Eshelby tensor S and its conjugate T depend on the aspect ratios of Ω_α. Hence, denote them by $\mathbf{S}^\alpha$ and $\mathbf{T}^\alpha$, respectively. $\mathbf{S}^\alpha$ and $\mathbf{T}^\alpha$ satisfy:

$$\mathbf{S}^\alpha + \mathbf{D}:\mathbf{T}^\alpha:\mathbf{C} = \mathbf{1}^{(4s)}, \mathbf{T}^\alpha + \mathbf{C}:\mathbf{S}^\alpha:\mathbf{D} = \mathbf{1}^{(4s)} \qquad (3.38)$$

For a single Ω_α embedded in an infinitely extended solid under uniform strain at infinity, the resulting strain in Ω_α are uniform and given by:

$$\boldsymbol{\varepsilon}^\alpha =< \boldsymbol{\varepsilon}^\alpha + \boldsymbol{\varepsilon}^\alpha >_\alpha = \mathbf{A}^\alpha:(\mathbf{A}^\alpha - \mathbf{S}^\alpha)^{-1}:\boldsymbol{\varepsilon}^\mathbf{0} \qquad (3.39)$$

Considering the case when the surface displacements are prescribed by macrostrain $\mathbf{E} = \boldsymbol{\varepsilon}^\mathbf{0}$ the average strain in each inclusion is now approximated by the uniform strain of a single inclusion embedded in an unbounded solid with the eleasticity of the matrix material, and subjected to the farfield strain $\boldsymbol{\varepsilon}^{\mathbf{0}}$ (or the farfield stress $\boldsymbol{\sigma}^{\mathbf{0}} = \mathbf{C}:\boldsymbol{\varepsilon}^{\mathbf{0}}$). Thus, from (3.39), it follows that:

$$\boldsymbol{\varepsilon}^{\boldsymbol{\alpha}} = \mathbf{A}^{\alpha}:(\mathbf{A}^{\alpha} - \mathbf{S}^{\alpha})^{-1}:\boldsymbol{\varepsilon}^{\mathbf{0}} \tag{3.40}$$

Substitution of (3.40) into the exact relation $(\bar{\mathbf{C}} - \mathbf{C}):\boldsymbol{\varepsilon}^{\mathbf{0}} = \sum_{\alpha=1}^{n} \mathrm{f}_{\alpha}(\mathbf{C} - \mathbf{C}^{\alpha}):\bar{\boldsymbol{\varepsilon}}^{\boldsymbol{\alpha}}$ then yields:

$$(\bar{\mathbf{C}} - \mathbf{C}):\boldsymbol{\varepsilon}^{\mathbf{0}} = \{\textstyle\sum_{\alpha=1}^{n} f_{\alpha}(\mathbf{C}^{\alpha} - \mathbf{C}):\mathbf{A}^{\alpha}:(\mathbf{A}^{\alpha} - \mathbf{S}^{\alpha})^{-1}\}:\boldsymbol{\varepsilon}^{\mathbf{0}} \tag{3.41}$$

and since the prescribed overall strain, $\boldsymbol{\varepsilon}^{\mathbf{0}}$, is arbitrary,

$$\bar{\mathbf{C}} = \mathbf{C}:\left\{\mathbf{1}^{(4s)} \textstyle\sum_{\alpha=1}^{n} \mathrm{f}_{\alpha}(\mathbf{A}^{\alpha} - \mathbf{S}^{\alpha})^{-1}\right\} \tag{3.42}$$

If all inclusions are similar, with identical elasticity and alignment, then $\mathbf{C}^{\alpha} = \mathbf{C}^{\mathrm{i}}, \mathbf{D}^{\alpha} = \mathbf{D}^{\mathrm{i}}, \mathbf{S}^{\alpha} = \mathbf{S}^{\mathrm{i}}, \text{and } \mathbf{T}^{\alpha} = \mathbf{T}^{\mathrm{i}} \text{ for all } \Omega_{\alpha}$

The overall elasticity tensor becomes:

$$\bar{\mathbf{C}} = \mathbf{C}^{\mathrm{g}}(\mathbf{1}^{4\mathrm{s}} - \mathrm{f}(\mathbf{A}^{\mathrm{i}} - \mathbf{S}^{\mathrm{i}})^{-1}) \tag{3.43}$$

Soilcrete stiffness tensor has been computed by using the preceding equations, with soil and grout elastic moduli found in the literature for a series of case studies [1, 6, 7, 14, 29, 30, 31, 32, 33, 34, 35, 36, 37]. Poisson’s ratio is generally not given. It has been assumed that Poisson’s ratio was equal to 0.25 for both the soil and the grout (Figure 25):

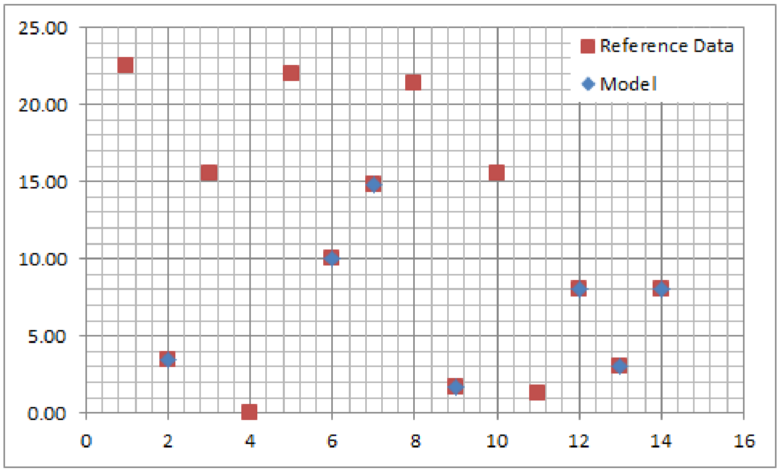

Figure 25- Eshelby's method: uniaxial compressive strength [MPa] of soilcrete: model predictions versus data found in the literature

The preliminary results shown in (Figure 25) show that the calibration of Eshelby's model is difficult. Future investigations will be devoted to the formulation of a more efficient homogenization scheme to predict soilcrete elastic properties.

3-3 Numerical Study of the Properties of the Jet-Grouted Column

3-3-1 Background on the Finite Element Method

3-3-1-1 Objectives of the Numerical Study

Most of the studies published so far focus on arching effects developed between concrete piles. It is demonstrated that arching effects depend on column spacing, embankment height and soil properties. In cohesive soils like clays, soil cohesion (or shear strength) plays an important role on the vertical loading transferred to the substratum by the ground. The purpose of the present study is to show that in addition to the structure geometry and the soil properties, soilcrete column characteristics play an important role in the ground mass bearing capacity. Parametric studies are performed to determine the influence of the mechanical properties of soilcrete and of the diameter of the grouted columns on the foundation efficiency. First, settlements are studied around an isolated soilcrete column embedded in a homogeneous non-cohesive soil layer. The numerical model is developed for plane strain analysis. Then, arching effects are studied for beam-caps (in plane strain). Correlations are proposed between grouting parameters (such as cement and soil properties and injection velocity) and the foundation efficiency. The settlements under the embankment are also studied thoroughly.

3-3-1-2 Brief Statement of the Theory of Finite Element Analysis

The finite element method is a numerical technique for finding approximate solutions of partial differential equations as well as integral equations. The solution approach is based either rendering the PDE into an approximating system of ordinary differential equations which are then numerically integrated using standard techniques such as Euler's method or Runge-Kutta.

In solving PDE, the primary challenge is to create an equation that approximates the equation to be studied, but is numerically stable, meaning that errors in the input and intermediate calculations do not accumulate and cause the resulting output to be meaningless. Numerical methods in continuum mechanics have traditionally been classified into three main approaches: finite element (FE), boundary element (BE), and finite difference (FD) methods. The finite element method is a good choice for solving PDE over complicated domains, when the domain change, when the desired precision varies over the entire domain, or when the solution lacks smoothness.

The main features of the FE methods are:

- The entire solution domain is divided into small finite domains called elements

- Over each element, the behavior is prescribed by the displacements of the elements and material law
- All elements are assembled together and the requirements of continuity and equilibrium are satisfied between neighboring elements
- Provided that the boundary conditions of the actual problem are satisfied, a unique solution can be obtained to the overall system of linear algebraic equations
- The solution matrix is sparsely populated (which means that outside of a band around the diagonal the matrix is full of 0)

In a three-dimensional Cartesian axes system there are six components of stress:

- Three direct (tensile or compressive) stresses $(\sigma_{xx}, \sigma_{yy}, \sigma_{zz})$ caused by forces normal to the area
- Three shear stresses $(\sigma_{xy}, \sigma_{xz}, \sigma_{yz})$ caused by shear forces acting parallel to the area

The first subscript refers to the direction of the outward normal to the plane on which the stress acts, and the second subscript refers to the direction of the stress arrow. For simplicity, in most problems the first and second subscripts can be interchanged; in other words, $\sigma_{xy} = \sigma_{yx}, \sigma_{yz} = \sigma_{zy} \text{ and } \sigma_{xz} = \sigma_{zx}$ (complimentary shear stress).

Stress-strain relationships are often called “substitutive equations”. For isotropic linear thermo-elastic materials with thermal strain, the following three-dimensional stress-strain equations (Hooke’s law) can be used

$$\varepsilon_{xx} = \frac{1}{E}\left[\sigma_{xx} - \nu(\sigma_{yy} + \sigma_{zz})\right] + \alpha(\Delta T)$$

$$\varepsilon_{yy} = \frac{1}{E}\left[\sigma_{yy} - \nu(\sigma_{zz} + \sigma_{zz})\right] + \alpha(\Delta T)$$

$$\varepsilon_{zz} = \frac{1}{E}\left[\sigma_{zz} - \nu(\sigma_{yy} + \sigma_{zz})\right] + \alpha(\Delta T) \tag{3.44}$$

$$\varepsilon_{xx} = \frac{1}{2\mu}\sigma_{xy}$$

$$\varepsilon_{xx} = \frac{1}{2\mu}\sigma_{xz}$$

$$\varepsilon_{xx} = \frac{1}{2\mu}\sigma_{yz}$$

where E is Young's modulus (N/m^2), ν is Poisson's ratio (dimensionless), μ is the shear modulus (N/m^2), α is the coefficient of thermal expansion (per Celsius degree) and ΔT is the temperature change from a reference value (per Celsius degree).

The shear modulus μ is defined as:

$$\mu = \frac{E}{2(1+\nu)} \tag{3.45}$$

The stress-strain equations (3.44) can be rearranged such that the stresses are on the left-hand side, resulting in the following matrix expression. Often referred to as the "material constitutive equation":

$$[\sigma] = [D][\varepsilon] \tag{3.46}$$

where $[D]$ is called the "elastic property matrix".

The notation and sign convention used for strains are the same as those used for stresses. The three-dimensional direct (non-shear) strains are related to the displacements in the following relationships:

$$\varepsilon_{xx} = \frac{\partial u_x}{\partial x}$$

$$\varepsilon_{yy} = \frac{\partial u_y}{\partial y} \tag{3.47}$$

$$\varepsilon_{xx} = \frac{\partial u_z}{\partial z}$$

where u_x, u_y, u_z are the displacements (deformations) in the x, y and z directions, respectively.

The three-dimensional shear strains are defined as:

$$\varepsilon_{xy} = \frac{1}{2}\left(\frac{\partial u_x}{\partial y} + \frac{\partial u_y}{\partial x}\right)$$

$$\varepsilon_{xz} = \frac{1}{2}\left(\frac{\partial u_z}{\partial x} + \frac{\partial u_x}{\partial z}\right) \quad (3.48)$$

$$\varepsilon_{yz} = \frac{1}{2}\left(\frac{\partial u_y}{\partial z} + \frac{\partial u_z}{\partial y}\right)$$

It should be noted that two definitions are often used for the shear strain, one with the1/2 factor and one without. The shear strain definition with the ½ factor is mainly used for the convenience of use in tensor notations. The shear strain definition without the ½ factor is referred to as the “engineering shear strain”. Both definitions are valid, provided that the definition is followed throughout the derivation of other relationships involving strains.

In order to examine the variation of stress from point to point within the body, consider the equilibrium of forces (resulting from the stresses) in the x, y, and z directions on a small differential volume. For example, σ_{xx} on one face changes to $(\sigma_{xx} + \delta\sigma_{xx})$ on the opposite face. Similarly, all other stress changes can be obtained. Therefore, the net force caused by the change in σ_{xx} in the x direction is given by:

$$\delta\sigma_{xx}(\delta y\delta z) = \frac{\partial \sigma_{xx}}{\partial x}\delta x(\delta y\delta z) \quad (3.49)$$

Similarly, the other forces caused by stresses in the x direction are:

$$\frac{\partial \sigma_{xy}}{\partial y}\delta y(\delta x\delta z), \frac{\partial \sigma_{xz}}{\partial z}\delta z(\delta x\delta y) \quad (3.50)$$

In addition to the net force in the x direction, there may be other forces caused by body forces (such as gravitational or centrifugal forces). If F_x is the net body force per unit volume acting in the x direction, then the equilibrium equation becomes:

$$\delta x\delta y\delta z\left(\frac{\partial \sigma_{xx}}{\partial x} + \frac{\partial \sigma_{xy}}{\partial y} + \frac{\partial \sigma_{xz}}{\partial z}\right) + \delta x\delta y\delta z(F_x) = 0 \quad (3.51)$$

Similarly, all other net forces can be obtained, resulting in the following differential equations of stress known as the “equilibrium equations”:

$$\frac{\partial \sigma_{xx}}{\partial x} + \frac{\partial \sigma_{xy}}{\partial y} + \frac{\partial \sigma_{xz}}{\partial z} + F_x = 0$$

$$\frac{\partial \sigma_{yx}}{\partial x} + \frac{\partial \sigma_{yy}}{\partial y} + \frac{\partial \sigma_{yz}}{\partial z} + F_y = 0 \qquad (3.52)$$

$$\frac{\partial \sigma_{zx}}{\partial x} + \frac{\partial \sigma_{zy}}{\partial y} + \frac{\partial \sigma_{zz}}{\partial z} + F_z = 0$$

where $F_x, F_y, \text{and } F_z$ are the body force components in the x, y, and z directions, respectively.

In order to examine the strain variation from point to point within the body, differential equations of strains can be derived in a similar manner to the differential equations of stress (the equilibrium equations). These strain differential equations are called “compatibility equations”, and they must satisfy the physical constraint that the body must remain continuous as it deforms. In other words, all displacements must be continuous and differentiable functions of position.

By eliminating $u_x, u_y, \text{and } u_z$ using the strain-displacement definitions in equations (3.47) and (3.48) and differentiating with respect to the x, y, and z directions, the following six compatibility equations can be obtained.

$$\frac{\partial^2 \varepsilon_{xx}}{\partial y^2} + \frac{\partial^2 \varepsilon_{yy}}{\partial x^2} = 2\frac{\partial^2 \varepsilon_{xy}}{\partial x\,\partial y}$$

$$\frac{\partial^2 \varepsilon_{yy}}{\partial z^2} + \frac{\partial^2 \varepsilon_{zz}}{\partial y^2} = 2\frac{\partial^2 \varepsilon_{yz}}{\partial y\,\partial z}$$

$$\frac{\partial^2 \varepsilon_{xx}}{\partial z^2} + \frac{\partial^2 \varepsilon_{zz}}{\partial x^2} = 2\frac{\partial^2 \varepsilon_{xz}}{\partial x\,\partial z} \qquad (3.53)$$

$$\frac{\partial^2 \varepsilon_{xx}}{\partial y\,\partial z} + \frac{\partial^2 \varepsilon_{yz}}{\partial x^2} = \frac{\partial^2 \varepsilon_{xz}}{\partial x\,\partial y} + \frac{\partial^2 \varepsilon_{xy}}{\partial x\,\partial z}$$

$$\frac{\partial^2 \varepsilon_{yy}}{\partial x\,\partial z} + \frac{\partial^2 \varepsilon_{xz}}{\partial y^2} = \frac{\partial^2 \varepsilon_{yz}}{\partial x\,\partial y} + \frac{\partial^2 \varepsilon_{xy}}{\partial y\,\partial z}$$

$$\frac{\partial^2 \varepsilon_{zz}}{\partial x\, \partial y} + \frac{\partial^2 \varepsilon_{xy}}{\partial z^2} = \frac{\partial^2 \varepsilon_{yz}}{\partial x\, \partial z} + \frac{\partial^2 \varepsilon_{xz}}{\partial y\, \partial z}$$

If displacements are used as the independent variables in the FE formulation, then the compatibility equations are automatically satisfied. Hence these compatibility equations will not be explicitly used hereafter. If other variables such as stresses are used as the independent variables, then stress functions must be chosen to explicitly satisfy the above compatibility equations. This is the main reason why displacements are chosen as the independent variables in most FE formulation.

3-3-2 Presentation of Theta-Stock

The following numerical study is done with Theta-Stock Finite Element code [11]. This program has been designed to study dry, saturated and unsaturated porous media. The analysis of the results is done using GID postprocessor.

3-3-3 Parameter Studies

In the sequel, Theta-Stock Finite Element program [11] is used to study settlements around an isolated soilcrete column embedded in a homogeneous non-cohesive soil layer. The column is considered as a “floating pile” (i.e. the column foot does not lie on the substratum), which corresponds to the most of the embankment studies reported in the literature. Only one ground layer is represented (sand). The domain modeled extends to 45 meters in the vertical direction and to 61 meters in the horizontal direction. The column is centered in the horizontal direction, and is 15 meters long. A plane strain configuration is adopted. Parametric studies are performed to determine the influence of the diameter of the grouted column (determined in Step 1) and of the mechanical properties of soilcrete (studied in Step 2) on the foundation efficiency. Both sand and soilcrete are assumed to be elastic. Three sets of material parameters are tested for soilcrete, as indicated in (Table 1).

The choice of modeling the embankment was pertinent due to the potential arching phenomena that could occur on top of the jet-grouted columns. Nonetheless, the model focuses on the arching effect occurring in the soil mass in-between the two jet-grouted walls and as a consequence, the model does not model the embankment with specific nodes but with a load on top of the modeled soil mass.

Table 1- Elastic properties of sand and soilcrete

	Sand	Soilcrete (Kauschinger et al., 1992)	Medium Soilcrete	Soilcrete (Covil & Skinner, 1994)
E [MPa]	1	10	100	6,000
υ[-]	0.3	0.25	0.25	0.25

The vertical dimension of the domain is three times the column height, which makes it possible to consider that the nodes at the bottom are not influenced by the loading in usual foundation problems. In the same way, the extent of the domain is twice as much as the column height on both sides of the column, which makes it possible to consider that the horizontal displacements are null on the lateral boundaries. Therefore, the following boundary conditions are adopted:

- a 50 kN-vertical load is applied at the top of the column,
- the remainder surface of the top domain boundary is free,
- vertical displacements are fixed to zero at the bottom boundary,
- horizontal displacements are fixed to zero on the lateral boundaries.

3-3-3-1Influence of Soilcrete Elastic Properties on Settlements

Assuming that the domain has a unit thickness in the out-of-plane direction, the 50 kN-load is applied by imposing a vertical pressure of 50 kPa on the top of a one-meter-width column. (Figure 26) shows the space variations of vertical displacements around the column, for the three soilcrete materials described in (Table 1). The reference simulation, for a sand layer with no injected column, is shown in Fig. 26a for the same loading conditions. It appears from that the presence of the soilcrete column can divide the maximum settlements observed at the top surface of the domain by more than two for (Fig. 26a and 26d). As expected, the variations of vertical displacements in the ground show a bulb shape, and settlements are reduced as soilcrete rigidity is increased. At a distance larger than one meter from the column, the settlements are almost the same in the four cases. The differences are expected to be larger in several columns induce an arching effect. This issue will be investigated in further studies.

3-3-3-2Influence of the Column Diameter on Settlements

The problem is solved for three column diameters: 0.5m, 1m and 2m. The same load is applied in all cases (50 kN), by imposing a vertical pressure of: 100 kPa on the 0.5m-diameter column, 50 kPa on the 1m-diameter column, 25 kPa on the 2m-diameter column. As expected, the settlements are less if soilcrete is stiffer and if the injected column is wider. Moreover, (Figure 27) shows a linear relationship between the soilcrete column diameter and the maximum settlements computed on the top boundary of the domain.

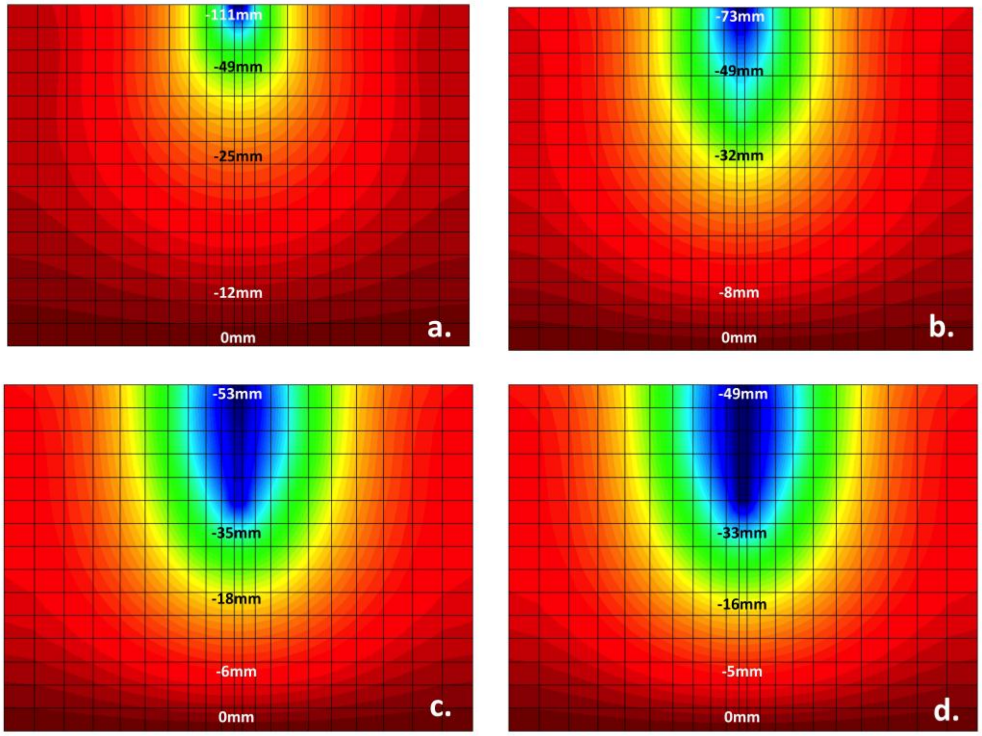

Figure 26- Influence of soilcrete elastic properties on the settlements around a one-meter-width injected column.

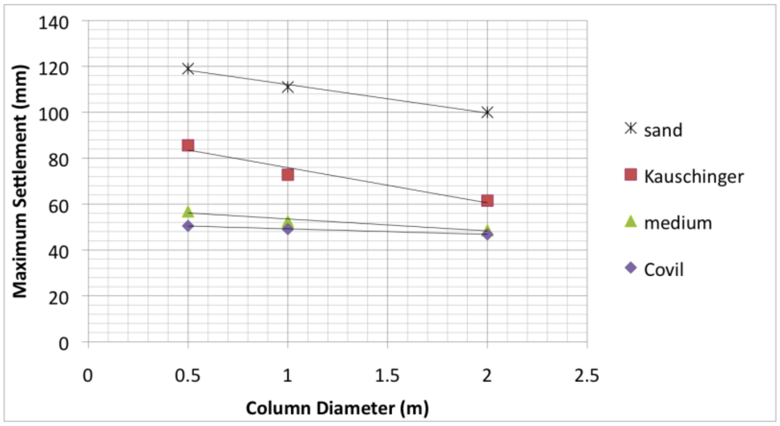

Figure 27- Maximum settlements computed for soilcrete columns of various diameters and various properties.

3-4 Arching in Tunneling

The purpose of this study is to model the re-orientation of stress around a tunnel due to the arching effects caused by two vertical reinforcements. In the proposed model, the two vertical reinforcements are assumed to be made of adjacent jet-grouted columns. The numerical analysis is based on a plane strain model, in which stress distribution is studied in the tunnel cross-section plane. Within this assumption, the vertical reinforcements are modeled as diaphragm walls with appropriate account of friction developed at the surface of the injected columns. In general, a diaphragm wall consists in a reinforced concrete vertical wall (with anchors in certain cases), that function according to the earth pressure theory.

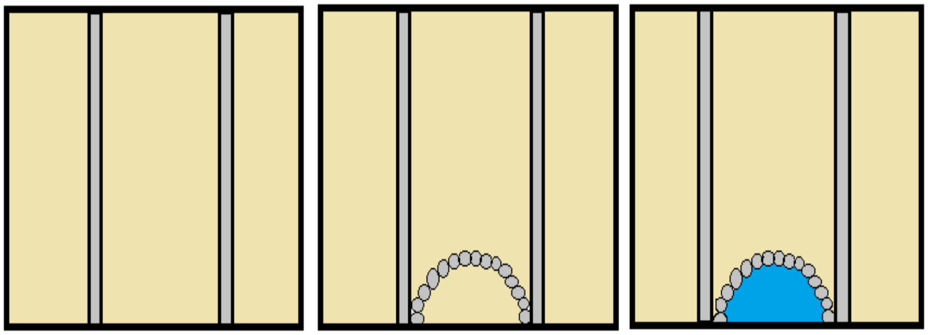

Figure 28- Description of the three construction steps of the new method: 1) Jet-grouting of the columns; 2) Sub-horizontal grouting of the shell; 3) Excavation

By chronological order, the first phenomenon to deal with is the deformation of the shell of the tunnel during the excavation of the tunnel. In the present study, displacements are predicted by resorting to the theory of plane strain elasticity applied to a circular cavity in an infinite soil mass (see Figure 28).

The deformation of the shell is expected to create a displacement of the soil mass above and as a consequence, the soil mass is will move relative to the jet-grouting columns. This relative displacement is going to generate a friction phenomenon at the surface of contact between the soilcrete and the soil mass. [21] explains the consequences of friction by resorting to the earth pressure theory, and used Jaky's theory to develop an analytical solution for the stress distribution. [24] enlightens the complexity of the choice of the earth pressure coefficient.

Lastly, the friction at the surface of contact between the soilcrete and the soil mass is going to allow a part of the stresses occurring in the soil mass to be transferred in to the injected columns, through friction forces. In the present state of the art, articles dealing with arching effects between jet-grouted columns deal with a homogeneous soil mass, which is not a valid assumption in the current case, including a tunnel excavation.

In reality, the three phenomena listed above interact, and do not occur in sequence. Actually, arching effects tend to decrease the value of the major principal stress developed in the soil mass. That decrease of the major principle stress will decrease the deformation of the shell which will decrease the vertical displacement and thus the friction. If the friction decreases, the amount of stresses supported by the jet-grouting column will decrease and thus it will increase the major principal stress and increase the deformations of the shell.

The objective of this research work is to analyze stress distributions due to the interacting effects of excavation and arching.

Most of the articles dealing with tunnelling found in literature deal with face stability [38, 39] or the optimization of the sub-horizontal jet-grouting technique used in New Austrian Tunnelling Method [40, 41, 42, 43, 44]. Nonetheless, it has been highlighted by [45] that a line of jet-grouted piles (on one side of the excavation only) can reduce the surface settlements. In order to test the effectiveness of a simple row of piles, the authors have computed the influence of parameters such as the spacing between the piles by means of three-dimensional finite element method. The authors of [45] have reached the conclusion (despite reduced experimental data) that the efficiency of such process is highly function of the spacing between the piles (Figure 29 and Figure 30). In fact, for a ratio s/b (of the spacing between the structural elements to their transversal size) ranging between 2 and 6, the row of piles is capable of notable benefits to the surrounding buildings because of the reduction in the average horizontal stress.

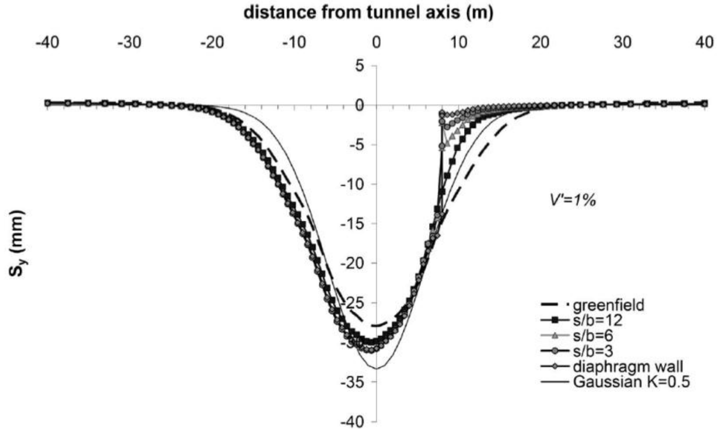

Figure 29- Settlement [mm] versus distance from tunnel axis [m] with the row on the right side (taken from [45])

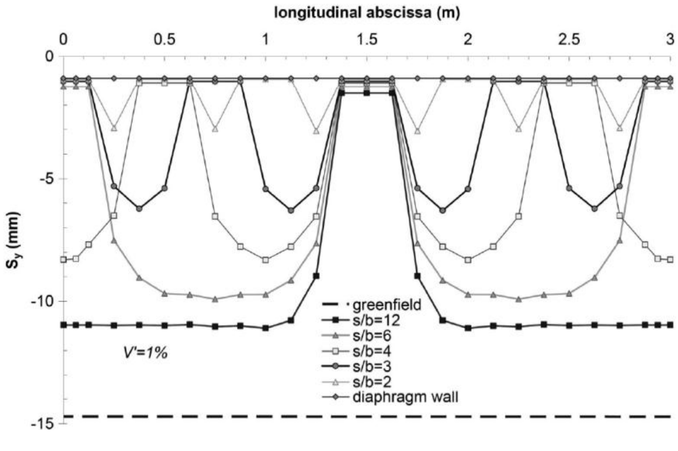

Figure 30- Settlement [mm] along the line of pile versus longitudinal abscissa [m] (taken from [45])

A form or arching effect develops between the piles. Adding a second line of piles (one line on each side of the tunnel) would generate an additional arching effect, between the two rows of piles. The consequent redistribution of stress is expected to reduce surface settlements, and to avoid any damage caused to the infrastructure in the surrounding area.

In addition to the three phenomena listed above, jet-grouting parameters (studied in the preceding section of this report) need to be calibrated in order to optimize the wall design. The problems at stake are the following:

- How to create a model taking into account the interaction between the three phenomena listed above?
- How to ensure the convergence of the iterative computation scheme?
- Is it possible to validate the model with data published in the literature?

In the sequel, an analytical method is formulated and tested with a plane strain numerical model.

3-4-1 Analytical Study

3-4-1-1 Deformation of the Tunnel Support ("Shell")

A plane model has been used to study stress re-orientation around a circular cavity excavated in an isotropic linear elastic soil mass [46]. The fundamental relations are:

Strain-displacement (plane stress and plane strain)

$$\epsilon_x = \frac{\partial u}{\partial x}, \epsilon_y = \frac{\partial v}{\partial y}, \gamma_{xy} = \frac{\partial u}{\partial y} + \frac{\partial v}{\partial x} \qquad (3.54)$$

Equilibrium conditions

$$\frac{\partial \sigma_x}{\partial x} + \frac{\partial \tau_{xy}}{\partial y} + X = 0, \frac{\partial \tau_{xy}}{\partial x} + \frac{\partial \sigma_y}{\partial y} + Y = 0 \qquad (3.55)$$

Compatibility equations

$$\frac{\partial^2 \epsilon_x}{\partial y^2} + \frac{\partial^2 \epsilon_y}{\partial x^2} = \frac{\partial^2 \gamma_{xy}}{\partial x \partial y} \qquad (3.56)$$

Substitution of the strains in the compatibility conditions (3.56) gives the stress compatibility equations in which we substitute the derivatives of the equilibrium conditions (3.55). If the body forces (X, Y) are assumed as constant or zero, the resulting equations are:

$$\left(\frac{\partial^2}{\partial x^2}+\frac{\partial}{\partial y^2}\right)(\sigma_x+\sigma_y)=0 \tag{3.57}$$

Now suppose Airy's function U is defined as:

$$\sigma_x=\frac{\partial y}{\partial x},\sigma_y=\frac{\partial^2 U}{\partial y^2},\tau_{xy}=\frac{\partial^2 U}{\partial x\,\partial y} \tag{3.58}$$

It is seen by substitution that U satisfies the equilibrium conditions (3.55). Substitution of (3.58) into (3.57) gives the biharmonic equations (3.4.6):

$$\frac{\partial^4 U}{\partial x^4}+2\frac{\partial^4 U}{\partial x^2\,\partial y^2}+\frac{\partial^4 U}{\partial y^4}=0 \tag{3.59}$$

For polar coordinates (r, Θ), Airy's stress function is defined as:

$$\sigma_r=\frac{1}{r}\frac{\partial U}{\partial r}+\frac{1}{r^2}\frac{\partial^2 U}{\partial \theta^2},\sigma_\theta=\frac{\partial^2 U}{\partial r^2},\tau_{r\theta}=-\frac{\partial}{\partial r}\left(\frac{1}{r}\frac{\partial U}{\partial \theta}\right) \tag{3.60}$$

With the corresponding biharmonic equations defined as:

$$\left(\frac{\partial^2}{\partial r^2}+\frac{1}{r}\frac{\partial}{\partial r}+\frac{1}{r^2}\frac{\partial^2}{\partial \theta^2}\right)\left(\frac{\partial^2 U}{\partial r^2}+\frac{1}{r}\frac{\partial U}{\partial r}+\frac{1}{r^2}\frac{d^2 U}{d\theta^2}\right)=0 \tag{3.61}$$

The general solution to the differential equation can be obtained through complex variables or through integration by the method of separation of variables. Solutions have been derived for the problem of stress distribution around a circular hole lying in an infinite plate. Thus, the tunnel radius is considered to be acceptable considering the depth at which the axis of the tunnel is in order to make this assumption. This problem is of great significance to the design of tunnels.

Consider an infinite plate subjected to boundary stresses σ_h and σ_v along the x and y axes, respectively, containing a circular hole of radius a centred at the origin.

For solutions of the stresses, σ_r, σ_Θ, $\tau_{r\Theta}$, Airy's stress function is given the form:

$$\mathrm{U(r\theta) = Al_nr + Br^2 + \left(Cr^2 + Dr^4 + \frac{E}{r^2} + F\right)\cos(2\theta)} \qquad (3.62)$$

The following boundary conditions are used to evaluate the constants in (3.62)

At r = a where a is the radius of the tunnel

$$\sigma_r = 0 = \tau_{r\theta} \qquad (3.63a)$$

At r equals to infinity for any value of Θ

$$\sigma_r = \frac{1}{2}(\sigma_h + \sigma_v) + \frac{1}{2}(\sigma_h - \sigma_v)\cos 2\theta \qquad (3.63b)$$

$$\tau_{r\theta} = -\frac{1}{2}(\sigma_h - \sigma_v)\sin 2\theta \qquad (3.63c)$$

The various derivatives of U are substituted into equations (3.60), the results are compared at the boundaries with (3.63) to evaluate the constants, and finally the following expressions are obtained for the stresses around the circular hole:

$$\sigma_r = \frac{1}{2}(\sigma_h + \sigma_v)\left(1 - \left(\frac{a}{r}\right)^2\right) + \frac{1}{2}(\sigma_h - \sigma_v)\left(1 - 4\left(\frac{a}{r}\right)^2 + 3\left(\frac{a}{r}\right)^4\right)\cos 2\theta$$

$$\sigma_\theta = \frac{1}{2}(\sigma_h + \sigma_v)\left(1 - \left(\frac{a}{r}\right)^2\right) - \frac{1}{2}(\sigma_h - \sigma_v)\left(1 + 3\left(\frac{a}{r}\right)^4\right)\cos 2\theta \qquad (3.64)$$

$$\tau_{r\theta} = -\frac{1}{2}(\sigma_h - \sigma_v)\left(1 + 2\left(\frac{a}{r}\right)^2 - 3\left(\frac{a}{r}\right)^4\right) \sin 2\theta$$

The displacements of points around the circular hole are obtained by integrating the stress-displacement relations.

For plane stress conditions, the displacements (radial displacement, u, and tangential displacement v) are obtained by integrating the stress-displacement equations:

$$\frac{\partial u}{\partial r} = \frac{1}{E}(\sigma_r - \nu\sigma_\theta$$

$$\frac{u}{r} + \frac{1}{r}\frac{\partial v}{\partial \theta} = \frac{1}{E}(\sigma_\theta - \nu\sigma_r) \qquad (3.65)$$

$$\frac{1}{r}\frac{\partial u}{\partial \theta}+\frac{\partial v}{\partial r}-\frac{v}{r}=\frac{2(1+\nu)}{E}\tau_{r\theta}$$

With the result that

$$\mathrm{u}=\frac{1}{\mathrm{E}}\left[\left(\frac{\sigma_\mathrm{h}+\sigma_\mathrm{v}}{2}\right)\left(\mathrm{r}+\frac{\mathrm{a}^2}{\mathrm{r}}\right)+\left(\frac{\sigma_\mathrm{h}-\sigma_\mathrm{v}}{2}\right)\left(\mathrm{r}-\frac{\mathrm{a}^4}{\mathrm{r}^3}+\frac{4\mathrm{a}^2}{\mathrm{r}}\right)\cos 2\theta\right]-\frac{\nu}{\mathrm{E}}\left[\left(\frac{\sigma_\mathrm{h}+\sigma_\mathrm{v}}{2}\right)\left(\mathrm{r}-\frac{\mathrm{a}^2}{\mathrm{r}}\right)-\left(\frac{\sigma_\mathrm{h}-\sigma_\mathrm{v}}{2}\right)(\mathrm{r}-\frac{\mathrm{a}^4}{\mathrm{r}^3})\cos 2\theta\right] \quad (3.66)$$

And

$$\mathrm{v}=\frac{1}{\mathrm{E}}\left[-\left(\frac{\sigma_\mathrm{h}-\sigma_\mathrm{v}}{2}\right)\left(\mathrm{r}+\frac{2\mathrm{a}^2}{\mathrm{r}}+\frac{\mathrm{a}^4}{\mathrm{r}^3}\right)\sin 2\theta\right]-\frac{\nu}{\mathrm{E}}\left[\left(\frac{\sigma_\mathrm{h}-\sigma_\mathrm{v}}{2}\right)\left(\mathrm{r}-\frac{2\mathrm{a}^2}{\mathrm{r}}+\frac{\mathrm{a}^4}{\mathrm{r}^3}\right)\sin 2\theta\right] \quad (3.67)$$

The displacements for the plane strain case can be recovered from () by making the substitution for the moduli with the results that:

$$\mathrm{u}=\frac{1-\nu^2}{\mathrm{E}}\left[\left(\frac{\sigma_\mathrm{h}+\sigma_\mathrm{v}}{2}\right)\left(\mathrm{r}+\frac{\mathrm{a}^2}{\mathrm{r}}\right)+\left(\frac{\sigma_\mathrm{h}+\sigma_\mathrm{v}}{2}\right)\left(\mathrm{r}-\frac{\mathrm{a}^4}{\mathrm{r}^3}+\frac{4\mathrm{a}^2}{\mathrm{r}}\right)\cos 2\theta\right]-\frac{\nu(1+\nu)}{\mathrm{E}}\left[\left(\frac{\sigma_\mathrm{h}+\sigma_\mathrm{v}}{2}\right)\left(\mathrm{r}-\frac{\mathrm{a}^2}{\mathrm{r}}\right)-\left(\frac{\sigma_\mathrm{h}-\sigma_\mathrm{v}}{2}\right)(\mathrm{r}-\frac{\mathrm{a}^4}{\mathrm{r}^3})\cos 2\theta\right] \quad (3.68)$$

And

$$\mathrm{v}=\frac{1-\nu^2}{\mathrm{E}}\left[-\left(\frac{\sigma_\mathrm{h}-\sigma_\mathrm{v}}{2}\right)\left(\mathrm{r}+\frac{2\mathrm{a}^2}{\mathrm{r}}+\frac{\mathrm{a}^4}{\mathrm{r}^3}\right)\sin 2\theta\right]-\frac{\nu(1+\nu)}{\mathrm{E}}\left[\left(\frac{\sigma_\mathrm{h}-\sigma_\mathrm{v}}{2}\right)\left(\mathrm{r}-\frac{2\mathrm{a}^2}{\mathrm{r}}+\frac{\mathrm{a}^4}{\mathrm{r}^3}\right)\sin 2\theta\right] \quad (3.69)$$

When r = a, the displacements are:

$$\mathrm{u}=\frac{1-\nu^2}{\mathrm{E}}(\mathrm{a}(\sigma_\mathrm{h}+\sigma_\mathrm{v})+2\mathrm{a}(\sigma_\mathrm{h}-\sigma_\mathrm{v})\cos 2\theta) \quad (3.70)$$

And

$$\upsilon=-\frac{1-\nu^2}{\mathrm{E}}(2\mathrm{a}(\sigma_\mathrm{h}-\sigma_\mathrm{v})\sin 2\theta) \quad (3.71)$$

The present study is based on the plane strain model described by equations (3.70). In addition, the following assumption is made in order to estimate σ_v (see Figure 31):

- The Arching effect is passive (which means that it occurs in a soft material located between two pieces of a harder material) and occurs between the two lines of columns.

It is necessary to develop a model to evaluate stress reorientation due to arching effects. Modelling the interactions between the vertical movement of the soil mass above the tunnel and the development of arching effects between the two jet-grouted walls will provide the state of stress around the tunnel at equilibrium.

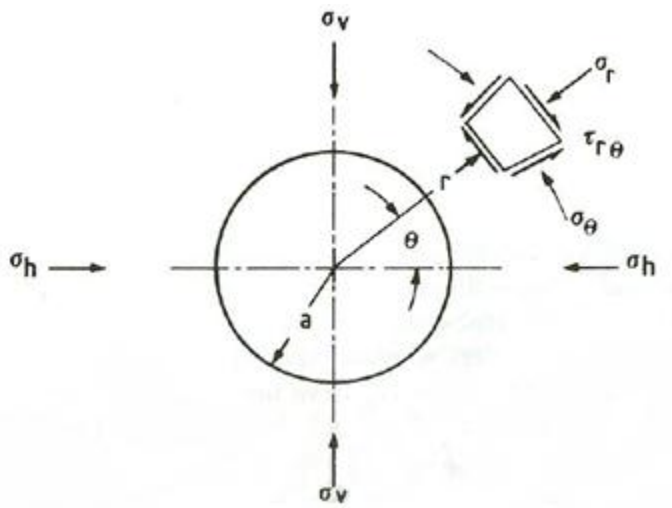

Figure 31- Stress redistribution around a circular opening (taken from [46])

3-4-1-2. Mobilization of Friction Behind Jet-grouted Walls

This phenomenon is the first to happen in the sequence that will lead to the arching effect. Model experiments reported by [39] indicated that a translating wall movement of about 1/6000 the height of the wall was required to mobilize friction. The rotation of the principal stresses at the wall due to mobilization of wall friction may be assumed to exist at full scale, even without wall movement, because of the weakness of the soil stability during the excavation and thus the tendency of the soil mass to move relative to the properly founded jet-grouting columns.

3-4-1-2-1 Classical Theory

Marston equations [24] were originally derived to define boundary stresses in soil partially supported between vertical walls with a constant separation distance B, and they predict a constant wall pressure below a certain depth. Behind a single wall, the horizontal distance equivalent to B/2 runs from the wall to stable soil, encountered behind a plane nominally rising at (45 + φ/2) from the base of the wall. Along this plane, the principal stresses are oriented vertically and horizontally, so the separation distance from the wall defines a half-arch. Thus, distance B changes with depth, becoming zero at the bottom of the wall. The distribution of horizontal pressure with depth may be obtained by the following process:

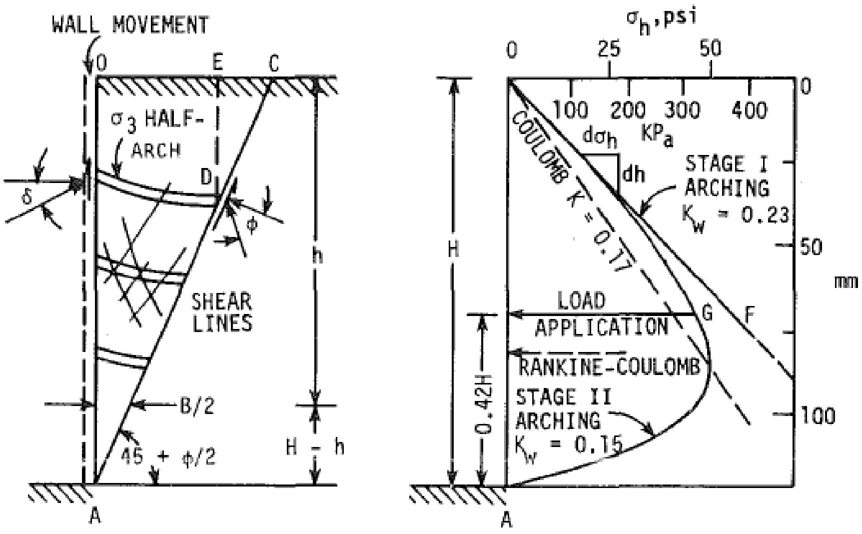

Figure 32- Differential element in classical representation of soil arching

In a vertical-walled trench, B is constant and the equation above can be divided by dh and integrated to give the commonly used Marston equation for loads on ditch conduit:

$$V = \gamma B^2 \frac{1-\exp(-2K_w\mu\frac{h}{B})}{2K_w\mu} \tag{3.72}$$

In which V = total accumulated vertical load at depth h; γ = unit weight of the soil; B = width of the trench; $K_w = \sigma_h / \sigma_{av}$; and μ = tanφ. Knowing that V/B is equal to $\sigma_{av,}$ $K_w \times \sigma_{av} = \sigma_h$:

$$\sigma_h = \frac{\gamma B}{2\mu}\left[1-\exp(-2K_w\mu\frac{h}{B})\right] \tag{3.73}$$

Then differentiating this equation

$$\frac{d\sigma_h}{dh} = K_w\gamma\exp(-2K_w\mu\frac{h}{B}) \tag{3.74}$$

Near the top of the wall, where h is small and B is large, the exponential term becomes 1 and the slope is K_w x γ, giving maximum wall pressures much larger than those predicted from Rankine and Coulomb theories, as indicated by the K_w line in (Figure 32):

$$\frac{B}{2} = (H-h)\tan(45-\frac{\phi}{2}) \tag{3.75}$$

Substitution of the equation (3.75) into (3.73) gives the equation for horizontal soil pressure at any level behind a rough wall:

$$\sigma_h = \frac{\gamma}{\mu}(H-h)\tan(45-\frac{\phi}{2})\left[1-\exp\left(-\frac{K_w\mu}{\tan(45-\frac{\phi}{2})}\frac{h}{H-h}\right)\right] \tag{3.76}$$

in which σ_h=horizontal pressure at level h; γ=unit weight of the soil; μ=soil-to-wall coefficient of friction, equal to tanδ; H=total height of the wall; h=elevation from the top; and Φ=soil internal friction angle. K_w is the ratio of σ_h at the wall to mean vertical stress σ_{av}.

3-4-1-2-2 Modified Theory

The surface of contact between the jet-grouted structure and the soil mass is no longer a plane but a curved surface (series of columns). The following coefficient Λ is introduced to account for the geometry of the problem.

In this model, each column is assumed to have a diameter of 1 meter (this is a usual order of magnitude). The friction force developed on the surface of the column is:

$$\mathrm{dV} + 2 \times \mathrm{K} \times \mu \times \Lambda \times \frac{\mathrm{V}}{\mathrm{B}} \times \mathrm{dh} = \gamma \times \mathrm{B} \times \mathrm{dh} \qquad (3.77)$$

Then, following the same steps than from the classical theory:

$$\sigma\mathrm{h} = \frac{\gamma \times \mathrm{B}}{2\mu}(1 - \exp(-2 \times \mathrm{Kw} \times \mu \times \Lambda \times \frac{\mathrm{h}}{\mathrm{B}})) \qquad (3.78)$$

The model predicts a reduction of the horizontal pressure, and thus the vertical pressure, in the soil behind the jet-grouting columns.

In fact, the interface between the soil mass and a jet-grouted column is expected to be rougher than between the soil mass and a standard concrete diaphragm wall, which is expected to generate more friction. The formula presented over-estimates the horizontal pressure remaining behind the walls – which is conservative for design purposes.

3-4-1-3 Arching Between the Two Rows of Jet-Grouted Columns

The arching theory states that for an element of soil which moves relative to a non-moving element, in our case the jet-grouting columns, the force is applied on the element below the one considered will be reduced from a normal state by the amount of friction between the soil mass and the columns (see Figure 33).

Terzaghi provides a state of the art on the theories of soil arching in [20, 21], and give a general empirical idea of the geometry of the sliding surfaces and zones of influence

Handy reviews some arching models in [24]. In this study, the following free body diagram is considered (Figure 33):

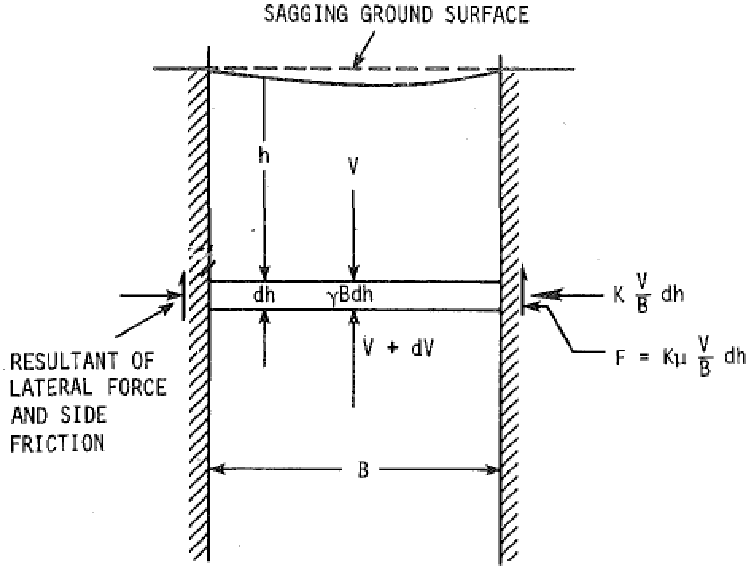

Figure 33- Free body diagram used by Handy for his arching theory

The objective of the modeling of arching effects is to find the orientation of the principal stresses developed in the soil mass. The arching slice-element of (Figure 33) is bounded by surfaces representing principal planes of zero shearing stress. The slice element is considered to be uniform in thickness and density which lead to a uniform weight throughout the arch. The result is that the shape of the arch is a catenary described by (2.47).

Differentiating this equation give the slope of the catenary which is described below.

Published studies are used to relate the following parameters of the arching:

- Major principal stress σ_1
- Distance between the two walls
- Vertical displacement d
- Unit weight of the soil
- Internal friction angle
- The earth pressure coefficient K

[25] uses the following formula to relate the load supported by reinforcement (P) to the surface load transmitted by the ground (q):

$$P = \frac{qB^{2}\sqrt{1+\frac{16d^2}{B^2}}}{8d} \tag{3.79}$$

The problem of this theory is that the major principal stress is not depending of the depth at which the arching is considered. In reality, there is a direct connection between the major principal stress and the depth: $\sigma_v = \gamma' \times z$ where z is the depth and $\gamma' = y - \gamma_w$.

There is a non-linear relationship, depending on depth, between the major principal stress and the horizontal stress applying on the jet-grouting columns as a function of the depth [24]. Horizontal stress represents the friction developed between the grouted structure and the soil mass when arching takes place.

CHAPTER IV

RESULTS

4-1 Calibration of the Model Predicting the Injection Radius

4-1-1 Presentation of the Computational Method

A computational method has been developed to determine the radius of the jet-grouted column. This has been done considering the engineering parameters of the system (injection pressure, thickness of the “pancake” (the disc of the given thickness due to a unique injection) kinematic viscosity, unit weight of the cement and speed of injection). The purpose of the part of the computational method is not to know exactly the space distribution of the solid particles embedded in the cement matrix, but to evaluate:

- the minimum zone within the soil has been improved (based on targeted soilcrete performance data)
- the radius beyond which the grout has not penetrated the soil mass

The computational algorithm first calculates the energy given to the grout during the injection, the work of the force required to expel water and solid particles out of the injected zone, and the energy dissipated by friction. Then parameter N is calibrated so as to get radius estimates as close as possible to the reference data.

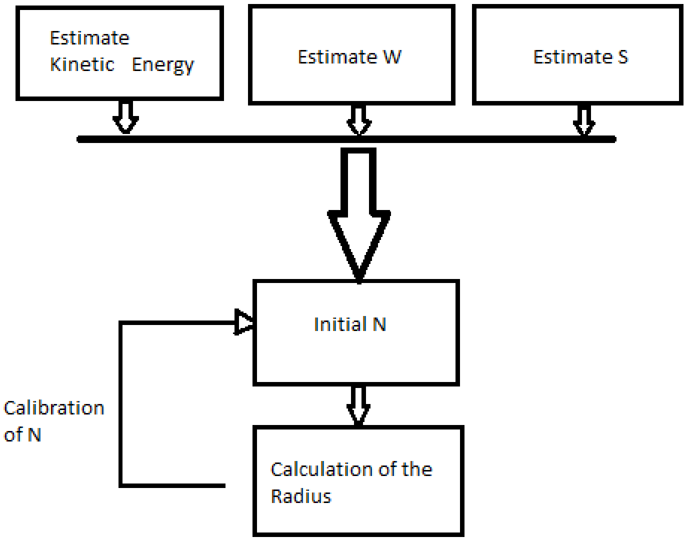

Figure 34- Diagram representing the process of calibration of the N.

4-1-2 Calibration of the Model Based on Energy Balance

As illustrated in Figure 34, using reference data on injection radius and velocity [4, 14, 28, 32, 47], equation (3.31) has been used to determine N. The results show a linear relationship between N and $\mathrm{R_{injection}}$ (Figure 35). The equation of the regression line is:

$$\mathrm{N} = 0.1315\mathrm{R_{injection}} - 0.0102 \qquad (4.1)$$

in which $\mathrm{R_{injection}}$ is expressed in meters. Equations 8 and 9 constitute the calibrated model proposed to predict the injection radius. The predicted values of $\mathrm{R_{injection}}$ are slightly lower than the reference data used for calibration, which meets the modeling objectives. More data is needed to validate the model.

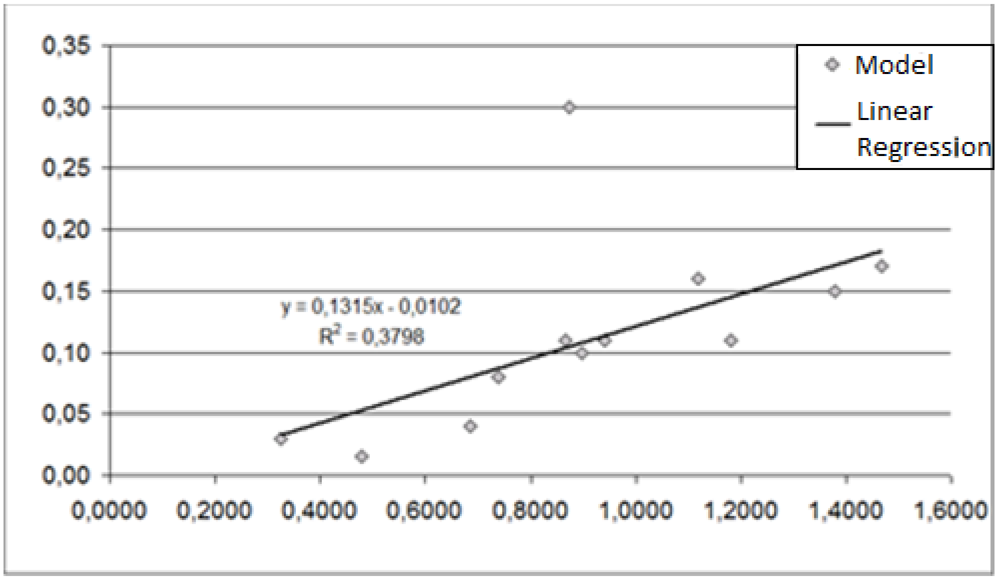

Figure 35– Number of round made by the nozzle versus radius of injection [m]

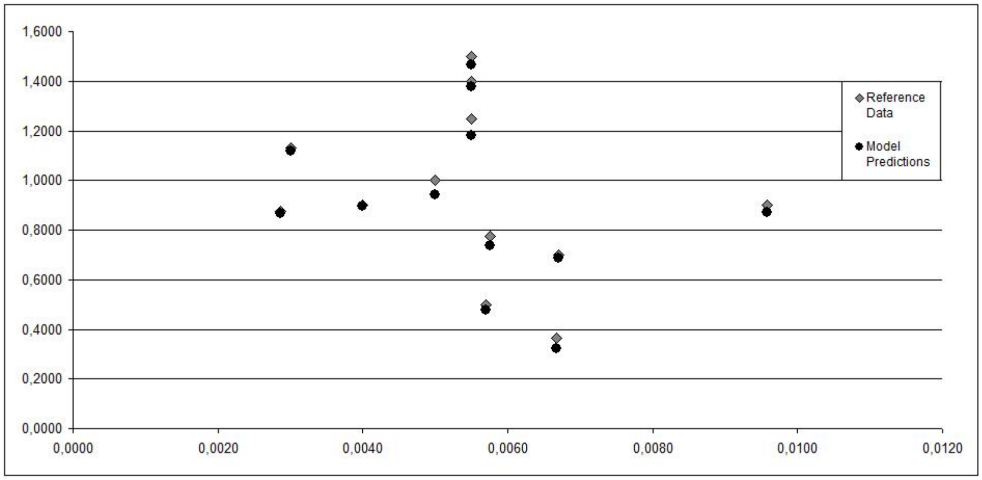

Figure 36- Radius of injection [m] versus the velocity of the cement in the ground for the reference data and the third energetic model predictions [m/s]

As expected, the theoretical results are below the measured ones for all the different values of the velocity of the grout in the soil (see Figure 36). Nonetheless, it appears that the accuracy of the results depends on the velocity of the grout in the soil and the number of revolutions of the nozzle.

The predictions of the third energetic model are compared to the predictions of the theoretical model developed by [28]. Both model predictions are compared to reference in situ measurements published in [6]. (Figure 37) shows that the predictions of the third energetic model are closer to the in situ measurements than Modoni's model [28]. Moreover, the third energetic model provides a lower bound to estimate the injection radius, which makes the predictions conservative. Last but not least, it has to be noted that Modoni's model is not formulated with classical engineering parameters. On the contrary, the proposed modeling framework is based on data that is accessible to the engineering community.

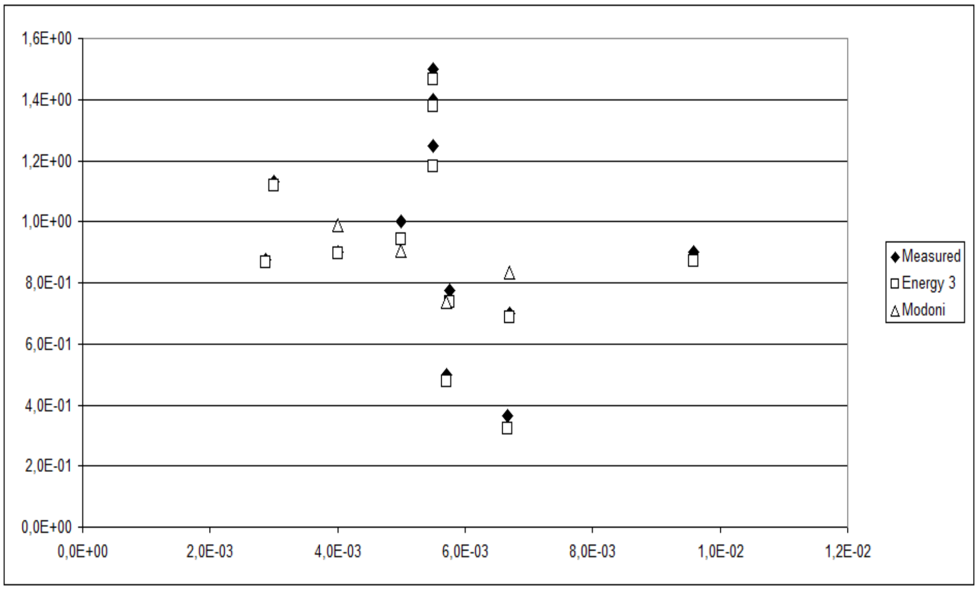

Figure 37- Comparison of two models predicting the injection radius: Modoni's model [28] and the third energetic model proposed in this paper

The knowledge of the upper and lower bounds for each pre-defined pancakes allows the definition of the upper bound shape and a lower bound shape. The lower bound shape will be used to determine the minimum radius of the jet-grouted column in order to design the bearable load. The upper bound shape of the columns will be used for the permeability and group effect problems.

4-2 Arching Proposed Computational Schemes

4-2-1 Iterative Computation of Surface Settlements and Subsurface Stresses

In order to estimate the effect of the residual stress on the shell of the tunnel, the authors have used the model developed in [25]. This model connects the different parameters listed below:

- Load on the arching surface
- Vertical displacement
- Residual stress
- Distance between the two lines of jet-grouted columns

Once the load on the arching surface is known and using the first hypothesis, the authors can express an equation of the fourth degree that connects the vertical displacement to the following parameters:

- Material parameters (friction angle, unit weight)
- Geometry parameters (distance between the columns, depth of the tunnel and radius)

The calculations are given below:

$$u = \frac{1-\nu^2}{E} \times \left[\frac{a\times(1+K)}{D} \times P + \frac{2a(1-K)}{D} \times P\right] \tag{4.2}$$

$$P = \frac{q_{max}\times D^2}{8u} \times \sqrt{\left(1 + \frac{16u^2}{a^2}\right)} \tag{4.3}$$

$\frac{1-\nu^2}{E} \times D \times (3-K) \times a \times q_{max}$ is called M which leads to the fourth degree equations mentioned above:

$$64u^4 - 16\frac{M^2}{a^2}u^2 - M^2 = 0 \tag{4.4}$$

Theoretically this equation of the fourth degree allows four solutions nonetheless, because physically the vertical displacement is following the gravity direction, two of the solutions can be eliminated. Moreover, if the condition $16\frac{\mathrm{M}^2}{\mathrm{a}^2} > \sqrt{\Delta} = \sqrt{196\frac{\mathrm{M}^4}{\mathrm{a}^4} + 256\mathrm{M}^2}$ is not fulfilled, two of the solutions are imaginary which is not acceptable which leads the authors to this conclusion:

- If $16\frac{\mathrm{M}^2}{\mathrm{a}^2} > \sqrt{196\frac{\mathrm{M}^4}{\mathrm{a}^4} + 256\mathrm{M}^2}$ the two solutions are $\sqrt{\frac{-\mathrm{b}-\sqrt{\Delta}}{2\mathrm{a}}}$ and $\sqrt{\frac{-\mathrm{b}+\sqrt{\Delta}}{2\mathrm{a}}}$
- Else then the only solution is $\sqrt{\frac{-\mathrm{b}+\sqrt{\Delta}}{2\mathrm{a}}}$

In order to confirm that result, the authors have written a MATLAB program. The physical phenomenon appears to have evolved from the steady state in response to the excavation of the tunnel. Stress is redistributed due to arching effect. In order to simulate that complex process, the authors have developed an iterative code.

The code is based on equations (4.2) and (4.3). Indeed, the value of the displacement necessary for the use of equation (4.3) is given by (4.2). Beginning with an initial value of the pressure on top of the tunnel, the computations stop when this pressure reaches a steady state. In order to compensate the problem of (4.3), the value of q_{max} is taken equal to:

$$\mathrm{q}_{\mathrm{max}} = \rho \times (\mathrm{z} - \mathrm{a}) \times \frac{(\mathrm{B}-(\mathrm{z}-\mathrm{a})\times\sin\phi)}{\mathrm{B}} \qquad (4.5)$$

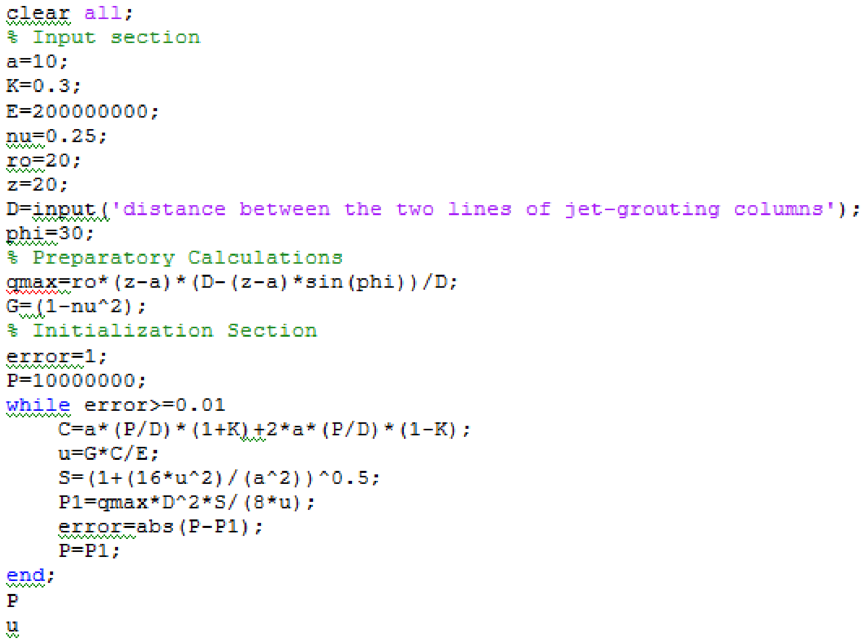

```
clear all;
% Input section
a=10;
K=0.3;
E=200000000;
nu=0.25;
ro=20;
z=20;
D=input('distance between the two lines of jet-grouting columns');
phi=30;
% Preparatory Calculations
qmax=ro*(z-a)*(D-(z-a)*sin(phi))/D;
G=(1-nu^2);
% Initialization Section
error=1;
P=10000000;
while error>=0.01
    C=a*(P/D)*(1+K)+2*a*(P/D)*(1-K);
    u=G*C/E;
    S=(1+(16*u^2)/(a^2))^0.5;
    P1=qmax*D^2*S/(8*u);
    error=abs(P-P1);
    P=P1;
end;
P
u
```

Figure 38- Code used for the computations

It appears that this code (see Figure 38) is not depending on the initial value of the residual stress and always gives the same values of the final vertical displacement than the mathematical analysis which confirm the last.

Table 2- Presentation of the results for the same initial conditions and for different initial P

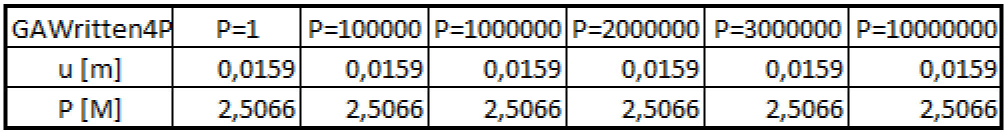

GAWritten4P	P=1	P=100000	P=1000000	P=2000000	P=3000000	P=10000000
u [m]	0,0159	0,0159	0,0159	0,0159	0,0159	0,0159
P [M]	2,5066	2,5066	2,5066	2,5066	2,5066	2,5066

Where P in top of the columns is the initial pressure given for the iterative process and (P, u) is the final state described by a vertical pressure and a vertical displacement (see Table 2).

The results are presented below (Figure 39):

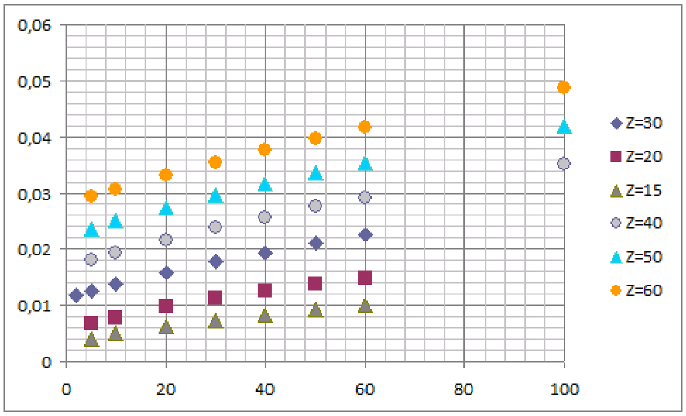

Figure 39- Vertical displacement [m] versus distance between two columns for different depth Z [m]

Firstly, it appears that the vertical displacements increase when the depth of the axis of the tunnel increases. That is normal considering that an increase of the depth equals an increase of the load on the shell of the tunnel and as a consequence, an increase of the deformation of the shell and of the vertical displacement on top of the shell.

Secondly; it appears that the vertical displacement increases when the distance between the two lines of columns increases. It is explained by the fact that the equation of the fourth degree in u is a function of B^2.

The experiments have shown that there is a limit of influence of the arching effect. The current theories founded in the literature are not taking into account this limit of influence (see Figure 40).

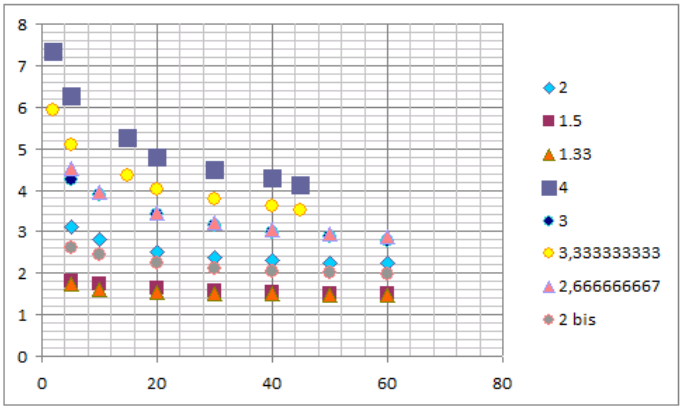

Figure 40- Ratio of u for two depths of the tunnel vs. distance between the two lines [m]

4-2-2 Analytical Model Based on Handy's Theoretical Work

The method develops below is using a combination of the engineering inputs and Handy's method in order to determine the pressure applied on top of the shell by the surrounding soil mass.

Assuming that arching will reorient stresses in a way that major principal planes form a catenary, compute principal stresses in the arch just above the tunnel shell. The scheme describing the different elements used in the computations is given in (Figure 41):

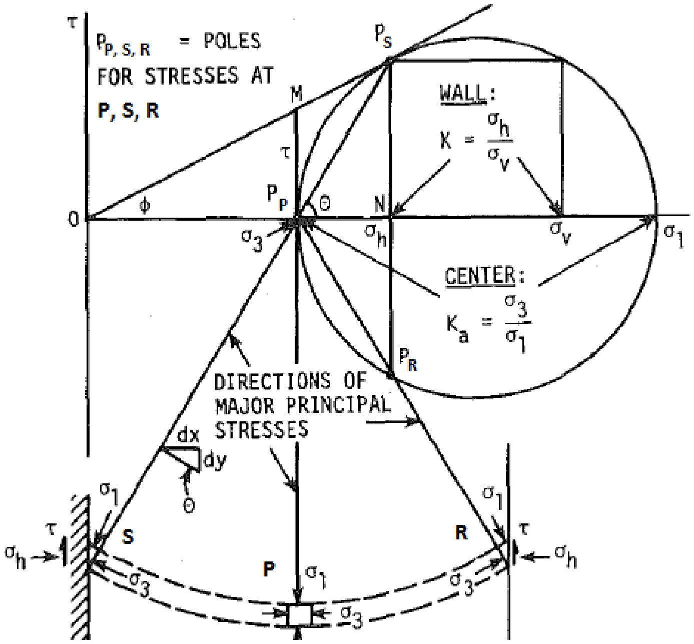

Figure 41- Scheme representing the model of the soil mass

The z-axis goes upward. Let’s call Z the depth at which is located the top of the shell of the tunnel. Using the catenary shape of the arch described by [24], the authors define Z’, the depth at which the catenary is reaching the jet-grouted columns, point S.

$$Z' = Z + a \times \cosh \frac{\frac{H}{2}}{a} \tag{4.6}$$

In which *a* is a coefficient depending on the internal friction angle, *H* is the distance between the two rows of jet-grouted columns.

The authors are now defining the vertical stress at the point, S, where the catenary is reaching the jet-grouting columns.

$$\sigma_V = \gamma \times Z' \tag{4.7}$$

Where γ is the unit weight of the soil and σ_V is the vertical stress.

Using Handy’s results, the Kw at this position is obtained and the authors defined the horizontal stress at point S.

$$\sigma_h = Kw \times \sigma_v \tag{4.8}$$

Finally, considering the shear stress equaled on every face, the authors get:

$$\tau = c + \sigma v \times \tan\phi \tag{4.9}$$

Where ϕ is the internal friction angle and c the cohesion of the soil.

Then using Mohr-Coulomb theory, the authors obtained the major principal stress at point S. Or according to the definition of the arching surface as a surface of equaled principal stresses, the major principal stress on top of the shell, point P, is known.

Moreover, the top of the shell, point P, is also the bottom of the catenary and as a result, the vertical stress is equal to the major principal stress at this point.

For a same material defined $[\gamma = 20\frac{\mathrm{kN}}{\mathrm{m}^3}, c = 0 \text{ and } \phi = 20 \text{ degrees}]$, the reference data for a soil without jet-grouting columns and model predictions are plotted for different depths and distance between the rows of jet-grouting columns.

A computational tool has been first developed in order to test the influence of the parameter H while being in a fixed geometry of problem (the depth Z of the axis of the tunnel and the radius R of the tunnel are not changing). The results are shown in (Figure 42):

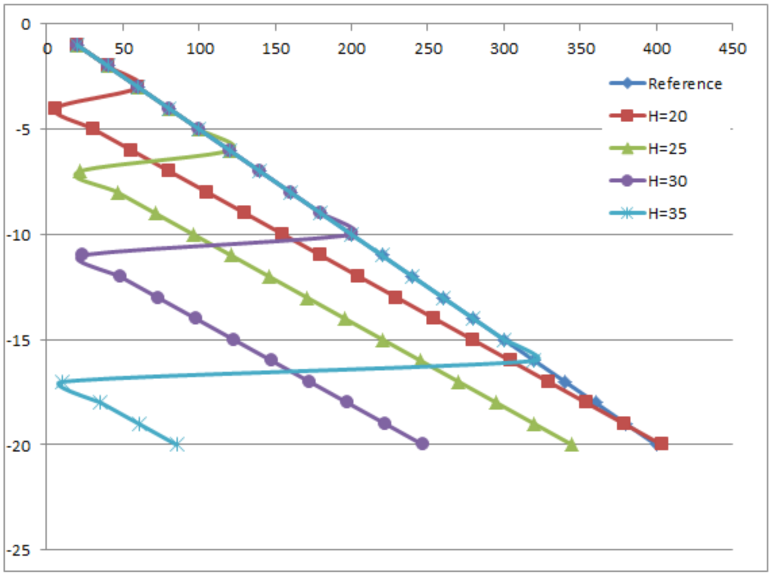

Figure 42- Influence of parameter characterizing the distance between the two walls: Major Principal Stress at the top of the shell [kN/m2] vs. Depth [m]

The fact that the curves are non-continuous is due to a simple consequence of Handy's theory. Indeed, Handy's work is based on the assumption that the arching surface is a fully developed, in the soil mass, catenary. As a consequence, the first fully developed catenary will only appears at a certain depth, depending on the distance between the two rows of piles.

This first catenary is defining two zones in the soil mass in between the two rows of piles. The soil mass below the catenary behaves in accordance with Handy's theory of arching. The soil mass above the first catenary behaves like a normal soil mass, without arching.

4-2-3 Numerical Study

PLAXIS Finite Element code has been used to test the model presented above in 2D configurations. The objective is to answer the following questions:

- What is the zone of influence of arching?

- How to determine the maximum influence of the arching?
- Can the different phenomena studied be linearly superimposed for obtaining the complete model?

The plane strain modelling requirements are:

- The geometry must be representative of the problem studied
- The dimensions of the soil mass must be large enough in order to assume that the load applied has no effect on the soil located at the boundaries.

Accordingly:

- The soil mass considered is 30 meters deep and 50 meters wide
- The jet-grouted walls are one meter thick.
- The tunnel is considered to have a radius of 5 meters.

The geometry of the problem study in the FEM analysis is presented in (Figure 43).

The boundary conditions are the following (Figure 43):

- Bottom: no horizontal or vertical displacements are allowed
- Vertical Far-field: only vertical sliding is allowed

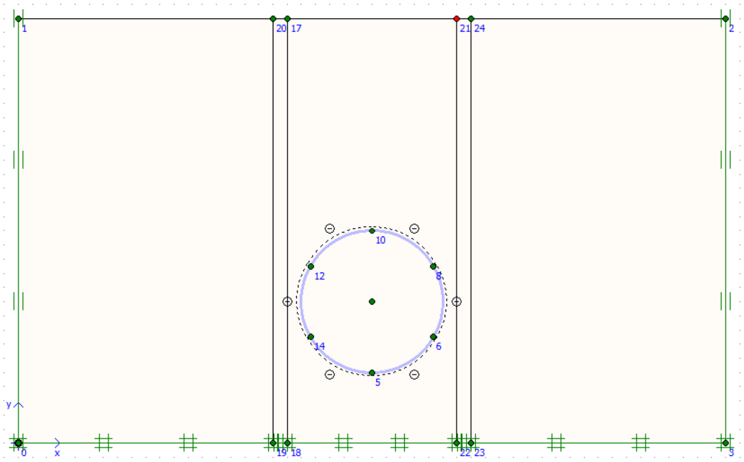

Figure 43- Presentation of the boundary conditions of the problem

The properties of the materials used for the simulations are presented in (Table 3- Values of the parameters describing the materials used in the problem).

Table 3- Values of the parameters describing the materials used in the problem

Properties	Sand	Grout
Model	MC	MC
Type	Drained	Drained
γ_{unsat} [kN/m^3]	16.5	24
γ_{sat} [kN/m^3]	20	24
k_x [m/day]	1	1
k_y [m/day]	1	1
E	80000	3000000
ν	0.3	0.3
c	1	1
ϕ	31	31
ψ	1	1

Properties	Shell
Type	Elastic
EA [kN/m]	14000000
EI [kNm]	143000
d [m]	0.35
w [kN/m/m]	8.4
ν	0.15

4-2-3-1 Influence of Parameter Characterizing the Distance between the Two Walls

The following figures (Figure 44) illustrate the influence of the spacing between the two jet-grouted walls.

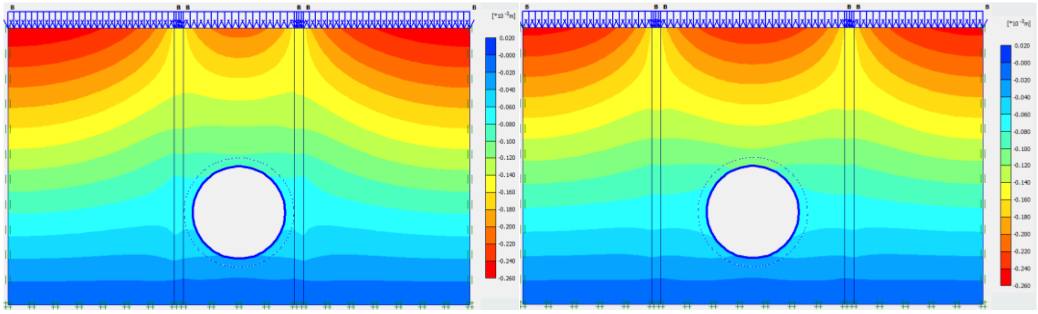

Figure 44- Graphical outputs for H=13 and H=21m (scale unit [mm])

The results for the entire set of test are given in the (Figure 45) which plots the vertical displacements versus the parameter H:

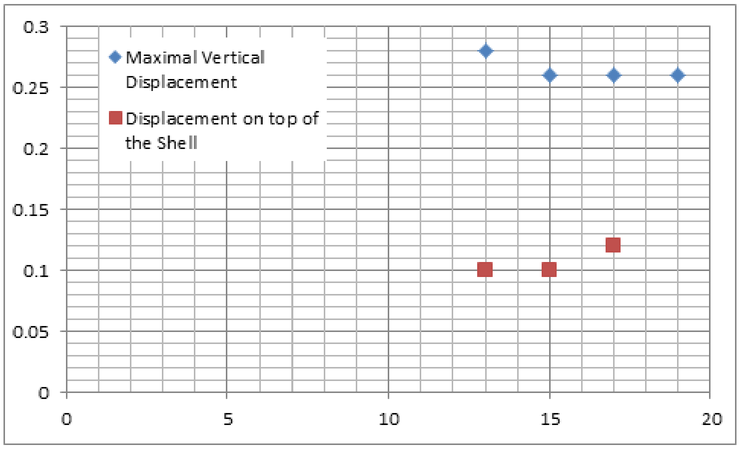

Figure 45- Vertical displacements [mm] versus distance between the two jet-grouting walls on top of the shell compared to the maximal displacement [m]

In addition, these results are compared to the ones get obtained using [24] (see Figure 46):

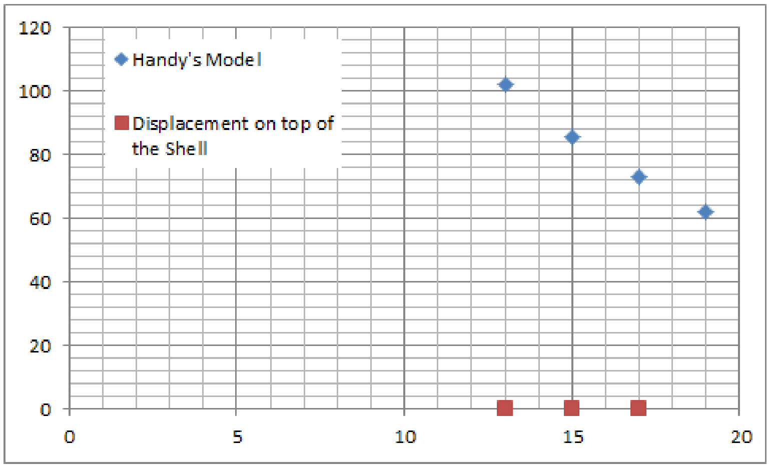

Figure 46- Vertical displacements [mm] versus distance between the two jet-grouting walls [m]

It appears that the more distant are the two rows of piles the more important are the stresses in the soil mass in particular on top of the shell. This result is in contradiction to the one obtained in the theoretical section using the theory developed by Handy. Indeed

Handy states that, for each depth, there is an optimum in the distance between the two rows of piles.

The difference between the analytical values and the numerical values is due to the fact that the analytical values are the results of two different theories partially coupled for this study. Although easy to partially couple by the complementarity of nature between the inputs and outputs of one other, it does not allow the same accuracy in the results. The two main parts that remain uncertain for the coupling and would explain the difference in the results are the two following one.

First, the fact that the presence of shell made of stiff concrete, even while in a shape that allow more easily the deformations, prevent the apparition of a fully developed catenary (see 4-4-3-4).

Second, the theory developed by MATLAB supposed an infinite continuous soil around the cavity of the tunnel, which is obviously never the case in tunneling and in the case studied is even worst by the presence of the two walls of jet-grouting whose influence on the deformations was at first neglected.

In order to verify this result, the authors have developed a model similar to the first one but for the load. The geometry is presented in (Figure 47):

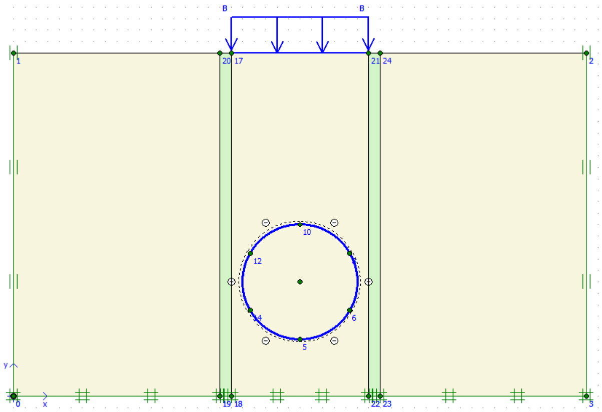

Figure 47- Presentation of the alternative model

The model is submitted to the same series of tests than the previous model. The curves obtained by plotting the vertical displacement versus the value of the parameter H as long as some particular results are shown in the following figure (Figure 48):

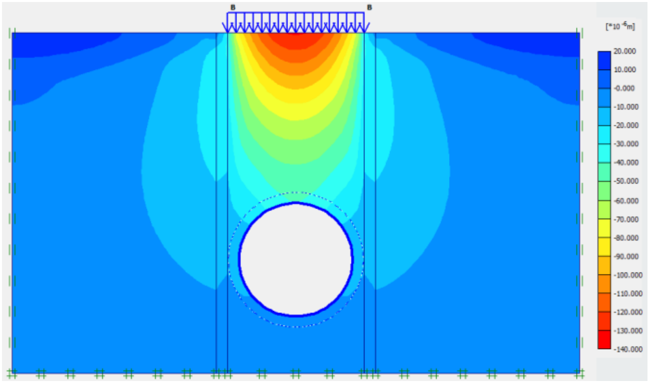

Figure 48- Graphical output for H=13 m

The results for the entire set of test are given in the following figure which represents the plotting of the vertical displacements versus the parameter H:

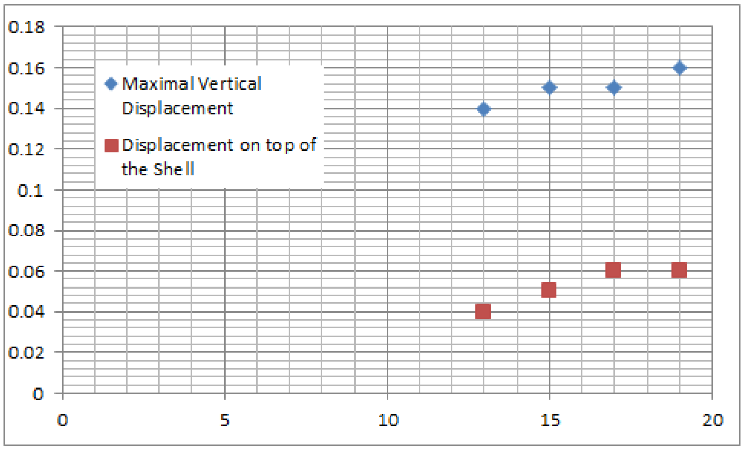

Figure 49-Vertical displacements [µm] versus distance between the two jet-grouting walls for a load applied only on the soil mass between the walls [m]

Once again, the same phenomenon can be observed (Figure 49). Moreover, under this kind of loading the influence of the rows of piles is not as important as in the other model. This is due to the fact that the solicitation of the piles is not as important as before because of the location of the load and its transmission to the surrounding soil.

4-2-3-2 Influence of the Elastic Modulus

The study of the influence of the elastic modulus of the soilcrete is relevant for several reasons. The most important ones are given below:

- A higher elastic modulus will allow the walls to take a bigger stress with less deformation and thus will change the path of stresses in the soil mass.
- A higher elastic modulus will decrease the horizontal deformations of the wall due to the loading on top of the soil mass. This will have for consequences to change the path of strain in the soil mass.

The tests of the model compared to the elastic modulus are realized using the geometry described below with H and B fixed with the respective values H=13 and

B=10. The parameters describing the properties of the sand and of the shell are given in the following chart (Table 4- Properties of the sand and of the shell):

Table 4- Properties of the sand and of the shell

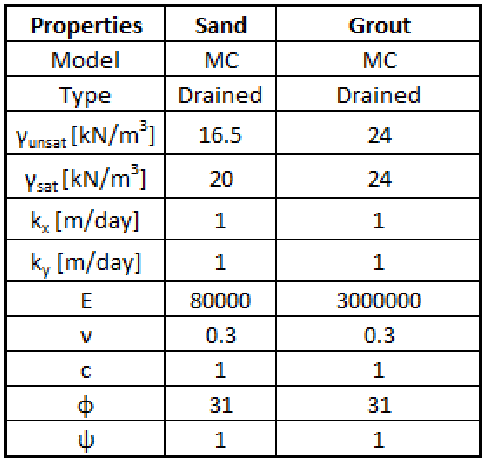

Properties	Sand	Grout
Model	MC	MC
Type	Drained	Drained
γ_{unsat} [kN/m^3]	16.5	24
γ_{sat} [kN/m^3]	20	24
k_x [m/day]	1	1
k_y [m/day]	1	1
E	80000	3000000
ν	0.3	0.3
c	1	1
ϕ	31	31
ψ	1	1

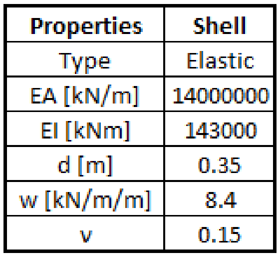

Properties	Shell
Type	Elastic
EA [kN/m]	14000000
EI [kNm]	143000
d [m]	0.35
w [kN/m/m]	8.4
ν	0.15

The results for $\mathrm{E} = 3\mathrm{GN/m}^2$ and $\mathrm{E} = 15\ \mathrm{GN/m}^2$ are given in (Figure 50):

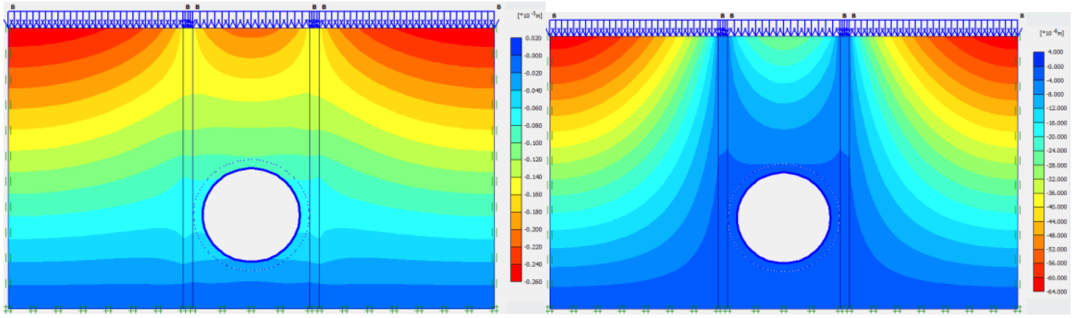

Figure 50- Graphical outputs for E=3000000 and E=15000000kN/m2

The results for the entire set of test are given in the following figure which represents the plotting of the vertical displacements versus the elastic modulus (Figure 51)

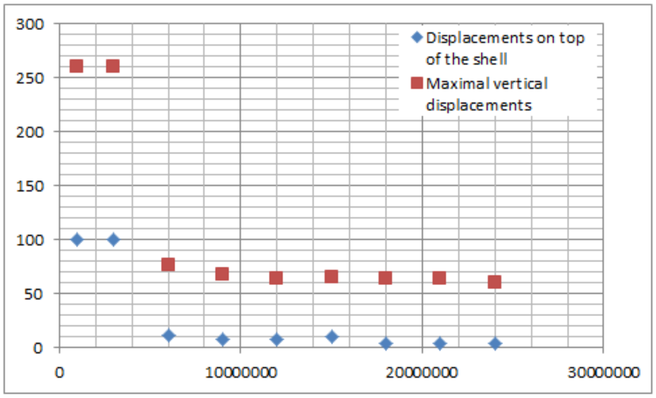

Figure 51- Vertical displacements [µm] versus the elastic modulus [kN/m]

It appears that the higher the elastic modulus of the soilcrete is the less important the vertical displacements observed in the soil mass are. It confirms that the influence of the elastic modulus of the soilcrete in the arching process. It also confirms the driving hypotheses that make the author study the influence of the elastic modulus.

4-2-3-3 Influence of the Shell

The last parameter the authors have studied is the influence of the shell. This is due to the fact that the arching phenomenon requires a small vertical displacement to take place. This need for a vertical displacement is expressed in numerous papers found in the literature but is not considered by [24].

It appears that PLAXIS is not displaying any influence of either parameters EA or EI. This is due to the fact that according to the set (EA, EI) PLAXIS is determining the width of the wall. This width is determined in order to conserve the same global properties and thus the same vertical displacements at the surface.

4-2-3-4 Comparison with Handy's Results

Along the processing of the different cases, it appears that the part located below the first catenary, developed in 4-4-2, is more affected by the presence of the tunnel than the part above the first catenary.

In addition it appears that in the case of the tunnel even the shape of the first catenary is modified. The modification is not influenced by the same parameters that are defining the original shape of the catenary (D, Φ).

The hypothesis which is explored on the following part is the one of the superposition of two fields. The first field, is the Handy's one and is governed by the parameters (D, Φ) while the second field, named modifications field would be governed by the parameter E and would explain the field of arching surfaces observed while superposed on the first field.

CHAPTER V

CONCLUSION

5-1 Findings and Limitations

5-1-1 Grout Penetration Distance

Several methods have been developed, either based on hydraulic theories or energy balance equations. Hydraulic methods are based on pressure drops. An upper bound for the penetration distance is determined by using regular pressure drops. A lower bound is determined by accounting for both regular and singular pressure drops.

In energetic methods, the kinetic energy of the injected grout is assumed to be compensated by the work of forces. Several hypotheses on the expression of these forces have been tested. The best model retained accounts for the force necessary to expel pore pressure from the soil and for shear forces due to the friction between the grout and the soil particles.

The results have been compared to reference data found in the literature. An upper and a lower bound have been computed for the radius of injection. The models proposed in this thesis compare reasonably well with the theoretical predictions of Modoni's model, which is the most performing technique found in the literature [28].

The energetic approach presented in this thesis allows the computation of a lower bound for the radius of injection, which is expected to provide safe design predictions.

5-1-2 Soilcrete Elastic Properties.

The radius of injection calculated in step 1 is used as a characteristic length to define a Representative Elementary Volume (REV), within which soilcrete elastic properties have been homogenized. This thesis has investigated three different homogenization techniques.

A hollow sphere model has been proposed. Because the mechanical properties of the grout are higher than the one of the soil, the grout is considered as the solid phase while the mechanical properties of the soil are not used. As a result, grout properties are used to model the solid matrix, whereas the volume fraction of the soil grains is used to quantify hollow spheres' porosity. The parameter f, characterizing the fraction of the grout, has been calibrated in the study to match the reference data.

The average and Eshelby’s methods are using the mechanical properties of both the soil and the grout. The main hypothesis is the close-packing of the homogeneous grain of soil.

In average, Eshelby’s method provides more accurate results than the average method, but there are more cases where theoretical values of the elastic moduli mismatch experimental reference data.

The high pressure high velocity fluid is breaking down the soil structure, and, because it is a turbulent flow, the grains of soil are mixed and displaced according to their size and shape. Unfortunately, there is not enough data in the literature on the spatial distribution of the inclusions to get accurate results from homogenization techniques.

Future research work will improve the geometric model used to describe soilcrete fabric.

5-1-3 Performance Analysis of Jet-Grouted Columns

A parametric study has been done with Theta-Stock Finite Element program to determine the influence of different geometrical and mechanical properties of isolated jet-grouted columns. The same Finite Element code has then been used in order to model an embankment supported by jet-grouted columns. Reverse arching has been observed between the columns. This form of passive arching actually helps transferring the load imposed by the embankment to the foundations instead of the soil mass.

A numerical model has been proposed to study surface settlements above a tunnel. Arching is studied between two rows of injected columns lying on each side of the tunnel.

Handy's work is used to determine the pressure on top of the shell of the tunnel. Then the current theories of geomechanics applied to tunneling are used to compute the pressure on top of the shell into a vertical displacement of the shell. This vertical displacement is then assumed to be transferred to the surface without any disturbance. In order to test this model, computations have been realized using MATLAB computational code. Settlements computed in the presence of columns are less than in reference case studies where only the tunnel is modeled. A parametric study on grout elastic modulus, column spacing and tunnel depth has been performed with the Finite Element code PLAXIS to illustrate the effect of ground improvement by jet-grouting.

Analytical and numerical studies do not provide the same predictions for surface settlements. A possible explanation is that the analytical solution proposed in this research work uncouples the computation of stress around the tunnel from the prediction of arching between the columns.

In addition, the catenary shape described [24] cannot be observed in the numerical simulation.

5-2 Prospective Research

1. It is envisaged to use Particulate Mechanical models and Discrete Element Methods in order to determine the spatial distribution of the soil grains in the cement matrix after injection, depending on the initial Grain Size Distribution of the soil and on the injection parameters. It is most likely that grain volumetric fraction will be much less close to the nozzle and then decrease while increasing the distance to the injected column. As a result, the REV size will depend on the distance to the nozzle. Homogenization could be performed on REV of various sizes to have an idea of the variation of soilcrete properties with the distance to the nozzle. A second homogenization would then be necessary in order to give the mechanical properties of the jet-grouting column as a single material.
2. The theory of arching (based on Handy's work) and the tunnel theory need to be fully coupled in order to get better predictions on the surface settlements in the case study presented in Step 3. Moreover, the soil mass surrounding the tunnel cannot be considered as a homogeneous and infinite medium, because of the presence of soilcrete columns on both sides of the tunnel.
3. The numerical studies presented in this thesis would require more experimental data for model calibration and validation.

REFERENCES

[1] Croce P, Flora A. Analysis of single-fluid jet grouting. Géotechnique 2000; 50: 739-748.

[2] Dabbagh AA, Gonzales AS, Pena AS. Soil erosion by a continuous water jet. Soils and Foundations 2002: 1-13.

[3] Pichler C, Lackner R, Spira Y, Mang HA. Viscoplastic material models for soil: new insight into the soil-support interaction in NATM tunnel excavations. Archives of Mechanics 2005: 209-240.

[4] Jaritngam S, Design concept of the soil improvement for road construction on soft clay. In: Proceedings of Eastern Asia Society for Transportation Studies. 2003, p.313-22.

[5] Keller Company. The soilcrete-jet grouting process. Website: http://www.kellerge.com.au, [accessed on 03/06/2012].

[6] Chiari A, Croce P, Some limits to the use of jet-grouting. In: Piling and Deep Foundations, Proceedings of the Fourth International Conference on Piling and Deep Foundations, Stresa, Italy. 1991, p.201-204.

[7] Fang YS, Kuo LY, Wang DR, Properties of soilcrete stabilized with jet grouting. In: Proceedings of the Fourteenth International Offshore and Polar Engineering Conference, Toulon, France. 2004. p.696-702.

[8] Heinz WF, Mining grouting: a rational approach. In: Proceedings of the Third International Grouting and Ground Treatment Conference, New Orleans, Louisiana. 2003, p.1115-1129.

[9] Ou CY, Teng FC, Wang IW. Analysis and design of partial ground improvement in deep excavations. Computers and Geotechnics 2007; 35: 576-584.

[10] Dormieux L, Kondo D, ULM FJ. Microporomechanics. Chichester, England: John Wiley & Sons; 2006.

[11] Gatmiri B, Arson C. Theta-Stock, a powerful tool for thermohydromechanical behaviour and damage modelling of unsaturated porous media. Computers and Geotechnics 2008; 35(6): 890-915.

[12] Hong WP, Lee JH, Lee KW, Analysis of vertical loads acting on embankment. In: Proceedings of the Fifteenth International Offshore and Polar Engineering Conference, Seoul, Korea. 2005, p.641-6.

[13] Hayward-Baker. Website: http://www.haywardbaker.com, [accessed on 03/06/2012].

[14] Kauschinger JL, Perry EB, Hankour R, Jet grouting: state-of-the-practice. In: Proceedings of the Grouting, Soil Improvement, and Geosynthetics Conference. 1992, p.169-81.

[15] Gazaway HN, Jasperse BH, Jet grouting in contaminated soils. In: Proceedings of the Grouting, Soil Improvement, and Geosynthetics Conference. 1992, p.206-214.

[16] Welsh JP, State of the art of grouting in North America. In: Proceedings of the Second International Conference on Ground Improvement Geosystems, Tokyo. Vol. 2; 1997, p.825-831.

[17] White DM, Koelling M, Ashcom DW, Kuma J. Design and construction of a jet-grouted barrier wall. Geo-Engineering for Underground Facilities 1999: 1027-38.

[18] Nemat-Nasser S, Hori M. Micromechanics: overall properties of heterogeneous materials. North-Holland: Elsevier; 1993.

[19] Imanishi H, Yamauchi Y, Ground behaviour during soil improvement by jet grouting. In: Proceedings of the Second International Conference on Ground Improvement Geosystems, Tokyo. Vol 1; 1996, p.133-36.

[20] Terzaghi K. Theoretical soil mechanics. New York: John Wiley and Sons; 1945.

[21] Terzaghi K, Stress distribution in dry and saturated sand above a yielding trap-door. In: Proceedings of the First International Conference on Soil Mechanics and Foundation Engineering, Cambridge, Massachusetts. 1936, p.307-311.

[22] Hong WP, Lee JH, Lee KW. Load transfer by soil arching in pile-supported embankments. Soils and Foundations 2007; 47(5): 833-43.

[23] Deb K. A mathematical model to study the soil arching effect in stone column-supported embankment resting on soft foundation soil. Applied Mathematical Modelling 2010. Personal correspondence.

[24] Handy RL. The arch in soil arching. Journal of Geotechnical Engineering 1985; 111(3): 302-18.

[25] Rehnman SE, Eriksson UB, Jendeby L. Embankment on soft soil, interaction between embankment, reinforcement and piles, long term measurement at Urvalla, Sweden 1999. Personal correspondence.

[26] Janna WS. Introduction to fluid mechanics. Boston: PWS Publishing Company; 1993.

[27] Idel'cik IE. Mémento des pertes de charges. Paris: Eyrolles; 1986.

[28] Modoni G, Croce P, Mongiovi L. Theoretical modelling of jet grouting. Geotechnique 2006; 56(5): 335-47.

[29] Covil CS, Skinner AE, Jet-grouting- a review of some of the operating parameters that form the basis of the jet grouting process. In: Proceedings of Grouting in the Ground Conference Organized by the Institution of Civil Engineers, London. 1994, p.605-29.

[30] Gruner LB. Jet grouting in cohesive soils. Geo-Engineering for Underground Facilities 1999: 1016-26.

[31] Gyorgy P, Hajnal I, Zsigmondi A, Foundation reinforcing of surrounding buildings around construction sites in urban areas by using jet grouting technology. In: Proceedings of the Ninth Danube-European Conference on Soil Mechanics and Foundation Engineering, Budapest. 1990, p.449-454.

[32] Katzenbach R, Iagolnitzer Y, Moormann C, New experimental results and sites experiences on grouting techniques. In: Proceedings of the European Conference on Soil Mechanics and Foundation Engineering, Amsterdam. 1999, p.1419-1431.

[33] Lunardi P. Ground improvement by means of jet-grouting. 1997: 65-85. Personal correspondence.

[34] Pellegrino G, Adams DN, The use of jet grouting to improve soft clays for open face tunnelling. In: Proceedings of the International Symposium on Geotechnical Aspects of Underground Construction in Soft Ground. 1996, p.423-28.

[35] Pichler C, Lackner R, Spira Y, Mang HA. Thermochemomechinal assessment of ground improvement by jet grouting in tunneling. Journal of Engineering Mechanics 2003: 951-962.

[36] M.Shibazaki. State of the art grouting in Japan. Grouting and Deep Mixing (Yonekura, Terashi & Shibazaki) 1997: 851-867.

[37] Welsh JP, Burke GK, Jet grouting – uses for soil improvement. In: Proceedings of the Geotechnical Engineering Congress. 1991, p.334-345.

[38] Chen RP, Tang LJ, Ling DS, Chen YM. Face stability analysis of shallow shield tunnels in dry sandy ground using the discrete element method. Computer and Geotechnics 2011: 187-195.

[39] Sherif MA, Ishibashi I, Lee CD. Earth pressures against rigid retaining walls. Journal of the Geotechnical Engineering Divison 1982; 108: 679-696.

[40] Croce P, Modoni G, Russo G. Jet-grouting performance in tunneling. 2004: 1-11. Personnal correspondence.

[41] Pichler C, Lackner R, Martak L, Mang HA. Optimization of jet-grouted support in NATM tunnelling. International Journal for Numerical and Analytical Methods in Geomechanics 2004: 781-796.

[42] Sun X, Haizhen W, Use of jet-grouting technique in treating large deformation of tunnel. In: Proceedings of the Fourteenth Southeast Asian Geotechnical Conference, Hong Kong. 2001, p.449-452.

[43] Yang JG, Xie YL, Wang YZ, Wei M, Pre-supporting with horizontal piles of jet-grouting in weak loess tunnel. In: Proceedings of the International Conference on Information Management, Innovation Management and Industrial Engineering. 2009, p.141-144.

[44] Zacas MK, Vandolas VO, Rahaniotis NA, Tzima K. Ensuring behavioural requirements of tunnelling through natural and man-made ground by employing the observational method. Geotechnical Measurements and Modelling 2003: 117-123.

[45] Bilotta E, Russo G. Use of a line of piles to prevent damages induced by tunnel excavation. Journal of Geotechnical and Geoenvironmental Engineering 2011: 254-260.

[46] Mahtab MA, Grasso P. Geomechanics principles in the design of tunnels and caverns in rocks. Amsterdam: Elsevier; 1992.

[47] Chen CN, Huang WY, Tseng CT. Stress redistribution and ground arch development during tunnelling. Tunnelling and Underground Space Technology 2011: 228-235.

Supplemental Sources

Allan ML, Kukacka LE. Grout-treated soil for low-permeability barriers around waste landfills. ACI Materials Journal 1994: 355-61.

Becker AA. An introductory guide to finite element analysis. New York: The American Society of Mechanical Engineers Press; 2004.

Chen RP, Chen YM, Han J, Xua ZZ. Theoritical solution for pile-supported embankments on soft soils under one-dimensional compression. Canadian Geotechnical Journal 2008; 45: 611-23.

Essler RD. Applications of jet grouting in civil engineering. Engineering Geology of Construction, Geological Society Engineering Geology Special Publication 1995; 10: 85-93.

Fang YS, Liao JJ, Lin TK. Mechanical properties of jet grouted soilcrete. Quarterly Journal of Engineering Geology 1994; 27: 257-65.

Hatt WK, Mills RE. Physical and mechanical properties of Portland cements and concretes. Engineering Experiment Station 1928; 34. Personal correspondence.

Hewlett WJ, Randolph MF. Analysis of piled embankments. Ground Engineering 1988; 21(3): 12-18.

Hin EC, Lee H, Das BM, Performance of embankment on soft clay supported by geogrid and concrete piles. In: Proceedings of the Twelfth Asian Regional Conference on Soil Mechanics & Geotechnical Engineering. 2003. Personal correspondence.

Hsi JP, Yu JBY, Jet grout application for excavation in soft marine clay. In: Proceedings of the International Conference on Soil Mechanics and Geotechnical Engineering. 2005, p.1485-88.

Jonkers HM. Self-healing concrete: a biological approach. Self-Healing Materials: an Alternative Approach to 20 Centuries of Materials Science 2007: 195-204.

Karol RH. Chemical grouting and soil stabilization. New York: Marcel Dekker Inc; 2003.

Kwong J, Sandefur K, Hahiro R, Case histories on design and construction of jet grouted ground for trenchless projects. In: Proceedings of the International Symposium on Ground Improvement Technologies and Case Histories. 2009, p.1-9.

Larock BE, Jeppson RW, Watters GZ. Hydraulics of pipeline systems. New York: CRC Press LLC; 2000.

Li VC, Yang EH. Self-healing in concrete materials. Self-Healing Materials: an Alternative Approach to 20 Centuries of Materials Science 2007: 161-193.

Low BK, Tang SK, Choa V. Arching in piled embankments. Journal of Geotechnical Engineering 1994; 120(11): 1917-37.

Matsumoto Y, Nishioka T. Theoretical tunnel mechanics. Tokyo: University of Tokyo Press; 1991.

Nikbakhtan B, Osanloo M. Effect of grout pressure and grout flow on soil physical and mechanical properties in jet grouting operations. International Journal of Rock Mechanics & Mining Sciences 2009: 498-505.

Pelizza S, Peila D. Soil and rock reinforcements in tunnelling. Tunnelling and Underground Space Technology 1993; 8: 357-372.

Popovics S. Strength and related properties of concrete a quantitative approach. New York: John Wiley and Sons; 1998.

Stemco. Website: http://www.stemco.com/, [accessed on 03/05/2011].

Stewart ME, Navin MP, Filz GM, Analysis of a column-supported test embankment at the I-95/Route 1 interchange. In: Proceedings of GeoTrans 2004. Personal correspondence.

Suer P, Hallberg N, Carlsson C, Benz D, Holm G. Biogrouting compared to jet grouting: environmental (LCA) and economical assessment. Journal of Environmental Science and Health. Part A, Toxic/Hazardous Substances & Environmental Engineering 2009; 44(4): 346-353.

Tonon F. ADECO full-faced tunnel excavation of two 260 m^2 tubes in clays with sub-horizontal jet-grouting under minimal urban cover. Tunnelling and Underground Space Technology 2011; 26: 253-266.

Wachman GS, Biolzi L, Labuz JF. Structural behavior of a pile-supported embankment. Journal of Geotechnical and Geoenvironmental Engineering 2010. Personal correspondence.

Wong IH, Poh TY. Effects of jet grouting on adjacent ground and structures. Journal of Geotechnical and Geoenvironmental Engineering 2000: 247-256.

Xanthakos PP, Abramson LW, Bruce DA. Ground control and improvement. New York: John Wiley & Sons; 1994.

Zhuang Y, Ellis EA, Yu HS, The effect of subsoil support in plane strain finite element analysis of arching in a pile embankment. In: Proceedings of the First International Conference on Transportation Geotechnics, Nottingham. 2008, p.25-27.

VITA

Benjamin Laurent Juge received his Bachelor of Science in Civil Engineering from the Ecole Speciale des Travaux Publics in 2010. He entered the Geotechnical Engineering program at Texas A&M University in September 2011 and received his Master of Science in May 2012. His research interests include ground improvement method and numerical analysis. He has also worked as an intern at the French Public Work Research Laboratory.

Mr. Juge may be reached at Zachry Department of Civil Engineering, Texas A&M University 3136 TAMU, College Station, Texas 77843-3136 USA.

His email is juge.benjamin@gmail.com.